EXPERIMENTAL STUDY OF XUROGRAPHIC MICROCHANNEL SINGLE-PASS SINGLE-PHASE COUNTERFLOW HEAT EXCHANGER

by

Sultan M. Alshareef

A thesis submitted to the faculty of
The University of Utah
in partial fulfillment of the requirements for the degree of

Master of Science

Department of Mechanical Engineering

The University of Utah

December 2012

The University of Utah Graduate School

STATEMENT OF THESIS APPROVAL

The thesis of **Sultan M. Alshareef**

has been approved by the following supervisory committee members:

Timothy A. Ameel	, Chair	**08/10/2012** Date Approved
Kuan Chen	, Member	**08/10/2012** Date Approved
Eric Pardyjak	, Member	**08/10/2012** Date Approved

and by **Timothy A. Ameel** , Chair of the Department of **Mechanical Engineering**

and by Charles A. Wight, Dean of The Graduate School.

ABSTRACT

Xurography is a relatively inexpensive rapid prototyping microfabrication method used to manufacture microfluidic devices. An experimental study of water flow in rectangular xurographic microchannel counterflow heat exchangers with different channels widths is reported. Four different microchannel heat exchangers having channel widths ranging from 350 μm to 1000 μm and aspect ratios ranging from 0.1 to 0.29 were fabricated using double-sided adhesive Kapton® polyimide tape and two square copper substrates. A mechanical clamping system provided additional mechanical force to prevent leakage and to enable higher flow rates. The maximum Reynolds number Re, based on the hydraulic diameter, was approximately 4500. Reported data include heat rate, heat flux, overall heat transfer coefficient, overall volumetric heat transfer coefficient, heat exchanger effectiveness, net transfer units, and two exergy efficiencies. These data are reported for each heat exchanger with up to three capacity rate ratios C_r. The maximum heat rate, achieved with the largest size channels with $C_r \sim 1$, approaches 77 W, corresponding to a heat flux of approximately 120 W/cm^2. The maximum overall heat transfer coefficient is 49.5 kW/m^2/K for the 500 μm channel width heat exchanger, which corresponds to an overall volumetric heat transfer coefficient of 488 MW/m^3/K. Strong agreement is found between the experimental heat exchanger effectiveness and

net transfer units relationship and an analytical expression for the conventional concentric tube counterflow heat exchanger. The maximum experimental effectiveness of about 0.623 was found for the 1000 μm channel width heat exchanger with $C_r \sim 0.5$. An exergy efficiency analysis suggests that laminar channel flows produce the maximum exergy efficiency for the heat exchanger. The study confirms that xurography can be used to create effective thermal devices, so long as maximum operating temperatures do not exceed the temperature limits of the adhesive.

To my grandfather, Jaber, my parents, Mubarak and Norah, my brother Tareq, and my lovely wife Charity and beloved sons Jibril and Noah

TABLE OF CONTENTS

LIST OF FIGURES

LIST OF TABLES

NOMENCLATURE

α_i	Channel aspect ratio
A_{fin}	Substrate heat transfer surface area
A_i	Channel cross sectional area
$A_{i,ht}$	Channel heat transfer surface area
C_r	Capacity rate ratio
C_i	Fluid heat capacity rate
C_{max}	Maximum heat capacity rate
C_{min}	Minimum heat capacity rate
$C_{p,i}$	Fluid isobaric specific heat capacity
$D_{h,i}$	Channel hydraulic diameter
δ_w	Separation wall thickness between channels
δx	Uncertainty in measured variable
δR	Total uncertainty in output
$\frac{\partial R}{\partial x}$	Sensitivity coefficient
ΔT_1	Temperature difference between the hot inlet fluid and the cold outlet fluid
ΔT_2	Temperature difference between the cold inlet fluid and the hot outlet fluid
ΔT_{lm}	Log mean temperature difference

ΔT_i	Fluid temperature change in channel
ΔP_i	Pressure drop in channel
ε	Heat exchanger effectiveness
ε_o	Perturbation for uncertainty analysis
ε_{th}	Theoretical heat exchanger effectiveness
ε_{ex}	Experimental heat exchanger effectiveness
η_{ch}	Fluids-based exergy efficiency
η_{oi}	System-based exergy efficiency
f_i	Channel friction factor
H	Channel height
H_{fin}	Fin height
h_i	Heat transfer coefficient
$h_{c,i}$	Enthalpy of inlet cold fluid
$h_{c,o}$	Enthalpy of outlet cold fluid
$h_{h,i}$	Enthalpy of inlet hot fluid
$h_{h,o}$	Enthalpy of outlet hot fluid
h_{ref}	Enthalpy at reference state
i	Subscript for c = cold and h = hot
j	Subscript for k = Kapton® tape, g = glass, and cu = copper
k_i	Fluid thermal conductivity
k_k	Kapton® tape thermal conductivity
k_g	Glass thermal conductivity

k_{cu}	Copper thermal conductivity
K_n	Knudsen number
λ_{mfp}	Mean free path
L	Characteristic length of the system
L_i	Channel length
$LMTD$	Log mean temperature difference
$\dot{m}_i$	Fluid mass flow rate
μ_i	Fluid dynamic viscosity
$NTU_{th,1}$	Theoretical net transfer units based on the 1D thermal circuit analogy using Eq. (3.9), (3.17), and (3.19)
$NTU_{th,2}$	Modified theoretical net transfer units based on Eq. (4.10)
NTU_{ex}	Experimental net transfer units
$Nu_{Dh,i}$	Nusselt number based on channel hydraulic diameter
P	Channel wetted perimeter
$P_{i,in}$	Fluid inlet pressure
$P_{i,out}$	Fluid outlet pressure
P_{ref}	Reference pressure
$\bar{P}_i$	Average pressure in channel
Pr_i	Fluid Prandtl number
q_i	Heat rate
$\bar{q}$	Average heat rate
q_{max}	Maximum heat rate in the system
$q_i^{''}$	Heat flux

$Re_{Dh,i}$	Reynolds number based on channel hydraulic diameter
R_{tot}	Total thermal resistance
R	Output quantity for uncertainty analysis
$S_{c,i}$	Entropy of inlet cold fluid
$S_{c,o}$	Entropy of outlet cold fluid
$S_{h,i}$	Entropy of inlet hot fluid
$S_{h,o}$	Entropy of outlet hot fluid
S_{ref}	Entropy at reference state
ρ_i	Fluid density
$T_{i,in}$	Fluid inlet temperature
$T_{i,out}$	Fluid outlet temperature
$\bar{T}_i$	Average fluid temperature
T_{ref}	Reference temperature
U	Overall heat transfer coefficient
U_j	Overall heat transfer coefficient for j = k, g, and cu
$U_{th,1}$	Theoretical overall heat transfer coefficient based on the 1D thermal circuit analogy using Eq. (3.9), (3.17), and (3.19)
$U_{th,2}$	Theoretical overall heat transfer coefficient based on the analytical *NTU* expression for the concentric tube counterflow heat exchanger using Eq. (3.9), (3.19), (3.22), and (4.10)
U_{ex}	Experimental overall heat transfer coefficient
U_{vol}	Experimental overall volumetric heat transfer coefficient
V_i	Fluid mean velocity
Vol_{fluid}	Fluid volume in the channel

W_i	Channel width
x_i	Measured variable
$\chi_{c,i}$	Exergy of inlet cold fluid
$\chi_{c,o}$	Exergy of outlet cold fluid
$\chi_{h,i}$	Exergy of inlet hot fluid
$\chi_{h,o}$	Exergy of outlet hot fluid

ACKNOWLEDGEMENTS

The current research project has many contributor individuals that I would like to thank and show appreciation for. First I would like to thank my Adviser Dr. Tim Ameel for giving me the chance to work under his supervision in this project. Dr. Ameel continuous support and faith on me and the project was one of the main motivations behind this research. His patience and assistance through the entire research journey was a key element to complete this research. Also, I would like to thank Dr. Gale for allowing the use of his lab equipments and the xurographic plotter. In addition, I want to send special thanks to my colleague Faisal Fathiel on his tremendous assistance during the entire period of this research. His valuable knowledge was a crucial part of execution and completing the current study. Thanks and appreciation also extends to Lam Nguyen, Dan Torgerson, Brian Spann, and Rahul Kolekar for their suggestions and advices that guided this research through several stages. Also, I would like to thank Mike Johnson for his assistance to use the cutting plotter and other equipments in Dr. Gale's lab. In addition, special thanks go to Jeff Kessler and Tony Roehrig, the staff from the mechanical engineering department, for their technical support during the experiment test stage. Finally, I would like to thank Dr. Kuan Chen and Dr. Eric Pardyjak for their involvement as committee members for this research study.

CHAPTER 1

INTRODUCTION

1.1 Motivation

1.1.1 Miniaturization and Microscale Engineering

Microscale engineering has become a significant field in the last few decades. The idea to miniaturize engineering devices has attracted many researchers since microfabrication technologies first started over two decades ago. Applying and validating macroscale theories, such as the Navier-Stokes equations and convection correlations, at the microscale level was, and remains, one of the biggest questions researchers are pursuing. At the macroscale, these theories are valid only for specific cases with strict assumptions and boundary conditions; at the microscale, these assumptions and specific cases might not be easily achievable or possible.

One of these macroscale assumptions is the continuum hypothesis, where the working fluid in any system is considered as a whole "continuum". The parameter that determines whether this assumption is valid for fluid flow is the Knudsen number K_n This dimensionless parameter relates the working fluid mean free path λ_{mfp} to the system characteristic length L.

$$K_n = \frac{\lambda_{mfp}}{L} \tag{1.1}$$

For $K_n \leq 0.01$, the working fluid is considered as a continuum. This parameter becomes more important when gas is the working fluid since the concept of the mean free path does not apply for liquids. However, mean spacing between liquid molecules can be used to determine the Knudsen number. For instance, the intermolecular spacing for water is about 0.3 nm, which places water clearly in the continuum flow region for most applications. On the other hand, the mean free path for gases might be affected by many factors such as the system size (characteristic length) and the operating temperatures and pressures. Conditions such as low pressure, high temperature, or small system size can increase the Knudsen number such that the fluid is not in the continuum regime. This scenario is one of the challenges that may be a result of the miniaturization process. Microscale devices also tend to have a very high surface area to volume ratio, which makes them very attractive for convective heat transfer, or other processes that occur at surfaces. As an example, the surface area to volume ratio in automobile radiators is about 1000 and in human lungs it is over 10,000. In this study, the surface area to volume ratio exceeds 20,000. Partially because of this high ratio, microchannel heat sinks, microchannel heat exchangers, and microreactors have been manufactured and developed in the last few decades. Another benefit from scaling down or miniaturization is the relative low cost of bulk manufacturing, which makes batch development of products attractive to business. As explained in the previous paragraph, there are some challenges, but also some promising aspects that result from miniaturization, which makes research at the microscale level an interesting and exciting area of study.

1.1.2 Micro-Electro-Mechanical Systems (MEMS) and Microfluidics

Microfluidics is an area that deals with the behavior of fluids that are constrained in systems with very small geometries, typically on the sub-millimeter scale. In life sciences (analytical sciences), such as biotechnology, analytical chemistry, medical technology, environmental monitoring, and food analysis, microfluidics has been used extensively. Other areas such as pharmacy, cosmetics, optics, electronics, and the print industry have also benefited from microfluidics. Microfluidics provides many advantages, such as reducing analysis times from hours to minutes or even seconds, reducing sample volumes by orders of magnitude, reducing required space and footprint, and providing easy handling and portability. Early microfluidics devices were first manufactured in the 1970s. Examples include the fully integrated miniaturized gas chromatograph and the implantable piezo micropump; however, these early attempts were not easily sustainable due to the dearth of inexpensive and available microfabrication techniques [1]. This obstacle, and the slow progress on the development of microfluidic manufacturing technologies, have slowed the progress of microfluidic applications. With more recent advances in microfabrication technologies, many new microfluidic devices have been manufactured.

Some key examples of modern microfluidic devices are the silicon-chip-based gas chromatograph at Stanford University and the ink-jet printer at IBM [2]. DNA analysis is another of the major uses of microfluidic devices. Polymerase chain reaction (PCR), integrated PCR, separation-based detection, and integrated DNA hybridization are a few examples of microfluidic devices used in DNA analysis. In these analyses, small volumes of DNA samples are pumped into microchannel devices that have different temperature

zones to facilitate the desired biological processes. Since the demand on these microfluidic devices has increased with time, the need to add other components and functions to these devices has grown. These integrated microfluidic devices incorporate many of the necessary components and functionality of a typical room-sized laboratory on a small chip [2].

1.1.3 Microchannel Heat Exchangers

Microchannel heat exchangers, including those operated with a single fluid (heat sink) or two fluids have been studied, manufactured, and developed by many researchers. These devices have been used to cool electronics that dissipate significant amounts of heat. In addition, microchannel heat exchangers have been used in chemical process engineering and the food processing industry.

Tuckerman and Pease [3] were the first to manufacture high-performance heat sinks for electronic component cooling. In their research, water-cooled silicon microchannels served as a heat sink to absorb a heat flux of up to 790 W/cm^2 with a maximum substrate temperature rise of 71 °C above the inlet water temperature. Even though this heat sink had only one fluid pass, which is different from the current two-fluid heat exchanger study, this was one of the first attempts to introduce a fluid as a cooling agent for electronic devices at the microscale. The work of Tuckerman and Pease has been extended since through extensive studies on microchannel heat sinks [4].

As mentioned earlier, microchannel heat exchangers are capable of transferring a significant amount of heat because of their high surface area to volume ratio. Also, convection heat transfer is inversely proportional to the hydraulic diameter D_h. As a

result, reducing the channel size significantly increases the heat transfer coefficient [20]. However, this increase in the heat transfer coefficient comes at the expense of an increase in pressure drop across the microchannels. It can be shown that pressure drop is proportional to D_h^{-4}. Since the fluid has to flow in a very small channel, higher pressures are required during the process. This may be the most expensive cost of using microdevices; hence, the designer has to weigh the cost associated with pumping requirements.

Microchannel heat sinks typically have deep channels [4], where the aspect ratio (channel depth to width) is more than 1, while microchannel heat exchangers tend to have shallow channels, where the aspect ratio is less than 1 [4]. This characteristic difference is due to the limitations of the early microfabrication technologies [4]. These constraints also limited the material choices for microdevices, in general. However, more recent advances in microfabrication technologies have made material selection for microdevices less of an issue. Microchannel heat exchangers have been constructed from several materials, such as silicon, nickel, copper, ceramic, and polymers. When microchannel plates are the primary building block of a heat exchanger, the final assembly of the device depends on the bonding technique. This bonding process depends on the materials, adhesives, and the microfabrication method. For example, in one method, plates of microchannel heat exchangers are bonded to form the final device using a high temperature fusing process with thin layers of tin solder [4]. These previous paragraphs are intended to provide a foundation to explain the motivation behind the current study. The microchannel heat exchangers in the current study have been fabricated using a novel method called xurography, which uses a double-sided polyimide Kapton® tape to

define the microchannels. This application of xurography is the first time the method has been applied to create microchannel heat exchangers. Xurography provides many advantages. First, xurography, as will be explained later in Chapter 4, is uniquely suited for rapid prototyping. Devices such as microchannel heat exchangers can be completely designed, fabricated and put into use in as little as 3 to 4 hours. Second, xurography does not require expensive equipment or materials. Finally, as mentioned above, using a double-sided adhesive Kapton® tape in the construction of the microchannels has not been studied before. Since the Kapton® tape has very low thermal conductivity; the thermal performance of the heat exchanger could be expected to be poor. However, since the size of the microchannels and the distance between them is relativity small, the temperature gradient in the wall separating the channels can actually be quite large, leading to much better than expected performance.

1.2 Xurography Technology

The xurography fabrication method is a rapid prototyping technology that has been recently developed to manufacture microchannel systems. Traditionally, this method is commonly used in the sign industry for cutting graphics in adhesive vinyl films [5]. As mentioned earlier, some microfabrication technologies are quite expensive and time consuming. Even though some of these high-tech fabrication methods can be very precise in creating microchannels, several applications in biomedicine and other areas of science do not require this high precision. A comparison between glass etching and xurography prototyping of microfluidic channels for DNA melting analysis has been conducted [6]. The study concluded that xurographic microfluidic channels compare well

with those etched in glass. Xurography, coming from the Greek words *Xuron* and *graphe* meaning *razor* and *writing*, respectively, uses a commercial cutting plotter to cut the outlines of designs (letters) using adhesive films to produce retail signs [5]. Xurographic plotters with an addressable resolution of 10 μm are available commercially. As mentioned earlier, many applications do not require high-resolution features. For example, micropumps, valves, and sensors have characteristic dimensions that range from 100 μm to 50 mm [5]. In microfluidics, xurography can be used to cut several different materials such as polymer films and adhesive tapes. Knife blades with different cutting angles are applied to cut the desired microchannel geometry. In the sign industry, the most common cutting angles for the knife blades are 30°, 45°, and 60°, with the angle measured from the surface of the material to the blade's cutting edge [5].

In the current study, the xurography technique is used to create microchannel heat exchangers with the use of double-sided adhesive polyimide Kapton® tape. This type of tape is a commercial adhesive that is used primarily as an insulation system in engineering applications such as automobile engines. The manufacturing process for the microchannel heat exchanger starts with the selection of the substrate material. Most fluid dynamic studies conducted in microchannel systems created by xurography have used glass as the substrate material [6]. Glass has the advantage of being biocompatible, electrically resistive, and transparent; however, it is brittle, not easily drilled, and prone to cracking. In the end, material selection depends on the nature of the microfluidic application, environment that surrounds the device, and the desired operation conditions. For this study, glass was used in the initial designs; however, the heat transfer results indicated that glass was a poor choice for the intended objective of the device. This poor

thermal performance of the glass as a substrate material was due to the low thermal conductivity of both the glass and Kapton® tape. This issue will be covered in detail in Chapter 4. Following initial testing with glass, copper was selected as the substrate material.

Regardless of the substrate material, a microchannel system has to have inlet and outlet ports for each fluid. Once the locations of these ports are known, holes have to be drilled through the substrate to allow the fluid to pass in and out of the microchannels. Nanoports, small fittings that are connected to external tubes, are then aligned with the drilled holes and clamped and cured to the substrate through a specific curing procedure. With the microchannel pattern cut in the Kapton® tape, the holes drilled in the substrate, and the nanoports attached to the substrates, the Kapton® tape is then sandwiched between the two substrates and cured. The specific curing procedure will be presented in Chapter 4. The xurography method, compared with other advanced microfabrication technologies, has the advantage of being very inexpensive and very quick. The average time to create a microchannel heat exchanger for this project was about 3 hours (from initial design to testing). On the other hand, the method produces features with less accuracy and precision that the more expensive technologies. Xurographic microchannels are prone to wavy wall channels, adhesive droplets in the channel, overcut and/or undercut corners, and poorly defined features due to inadvertent removal of adhesive during the peeling process [21]. The complete xurography process is completely described by Nguyen [21].

1.3 Summary

Research on microfluidics and MEMS devices has been growing rapidly over the last few decades. Microfabrication technologies have also been expanded in that same time frame such that there are now many different high-precision methods available to designers. The xurography microfabrication technology has been shown to be very effective in creating microchannels that do not require high precision geometries. In addition, xurography is considered relatively inexpensive compared to other technologies. Xurography is also capable of producing products in a shorter time than other technologies.

Microchannel heat exchangers fabricated by xurography with Kapton® tape have not yet been studied. The thermal performance of this type of microchannel heat exchanger is unknown, which makes this research more interesting. The research questions of interest in this study are:

1) Can a compact single-pass two-channel heat exchanger be fabricated by xurography?
2) How does the thermal performance of the microchannel heat exchanger compare to theory?
3) What are the temperature limits for the fluids? It is understood that the cured adhesive in the Kapton® tape has upper limits on its operating temperature.
4) What are the upper limits on flow rate and pressure drop for a xurographic microchannel heat exchanger?
5) Is glass an acceptable substrate material for microfluidic systems that require interfluid heat transfer?

6) What are the best conditions to operate the heat exchanger from a cost (pressure drop)/benefit (heat transfer) analysis?

In Chapter 2, an extensive literature review, concentrating on the experimental works on microchannel heat exchangers (parallel, counter-, and cross-flow) by other researchers is presented. Furthermore, the various manufacturing technologies used in these studies will be discussed. Models used to predict performance and design are presented in detail in Chapter 3. Commercial software packages, specifically EES and Matlab, have been used to facilitate the modeling. Chapter 4 includes a detailed description of the xurography microfabrication method. The processes of cutting, material removal, drilling, curing, and final assembly are explained. Also, in Chapter 4, the experiment apparatus and test procedure are described. The data acquisition system and data reduction program are included. Experiment results and observations are presented in Chapter 5. Furthermore, a comparison between the current study results with similar studies will be presented. Conclusions and the researcher's recommendations for future work are presented in Chapter 6.

CHAPTER 2

LITERATURE REVIEW

2.1 Single-Phase Heat Transfer in Mini- and Microchannel Devices

The science of heat transfer has played a vital role in a significant number of scientific research and engineering applications. Hence, tremendous effort has been placed on understanding how heat transfer processes are governed. Thermal and heat transfer analysts over the last century have studied heat transfer processes extensively in conventional size systems. Governing equations have been formulated and solved for many different applications for different boundary conditions. As a result, numerous theoretical solutions and correlations have been proposed for both laminar and turbulent flow regimes. These correlations have been used in the thermal design and analysis of most conventional-size applications. These theoretical solutions and correlations are well documented such that macroscale heat transfer mechanisms are well understood. However, with recent advancements in microfabrication technology and the increased demand for small devices that can cool high heat flux electronic components, heat transfer at the microscale level has became equally as important as that at the macroscale. This urgent need to explore the heat transfer phenomenon at the microscale has been growing the development of microfabrication technologies. However, the corresponding

understanding of the basic mechanisms of momentum, heat, and mass transfer at the microscale has not been adequately clear to researchers and designers. This understanding is crucial when designing micro-devices and in predicting overall thermal system performance.

Microchannel devices, such as heat sinks and heat exchangers, have very high surface area to volume ratios, which allows them to dissipate heat fluxes at very high rates. Cooling of mirrors used in high-power laser systems [1] and controlling fluid transport and its precise thermal behavior in biomedical and genetic engineering [1] are two examples of heat flux removal in MEMS equipment. In convection, fully developed heat transfer coefficients are inversely proportional to microchannel diameter, which proves advantageous for thermal performance when downsizing. However, the pressure drop in these small channels is usually the cost for that high thermal efficiency. Microchannels are used with devices incorporating single-phase liquid flow. Micro-pumps, microvalves, and microsensors have been micromachined and used in the early applications of microchannels [1]. Biological and life sciences have taken advantage of microchannels for analyzing biological materials, such as proteins, DNA, cells, embryos, and chemical reagents [1]. Microchannel devices have been classified by their characteristic length, mainly the channel diameter, by some researchers. Kandlikar and Grande [1] have proposed the following classification based on hydraulic diameter D_h:

Conventional Channels		D_h	> 3 mm
Minichannels	3 mm ≥	D_h	≥ 200 μm

Microchannels	200 μm ≥	D_h	≥ 10	μm
Transitional Channels	10 μm ≥	D_h	≥ 0.1	μm
Transitional Microchannels	10 μm ≥	D_h	≥ 1	μm
Transitional Nanochannels	1 μm ≥	D_h	≥ 0.1	μm
Molecular Nanochannels	0.1 μm ≥	D_h		

For noncircular channels, D_h is defined as:

$$D_h = \frac{4A}{P} \tag{2.1}$$

where A is the channel cross sectional area and P is the channel wetted perimeter.

Mehendale et al. [2] suggested a different classification for microchannel devices as follows:

Conventional Heat Exchangers		D_h	> 6	mm
Compact Heat Exchangers	6 mm ≥	D_h	≥ 1	mm
Meso Heat Exchangers	1 mm ≥	D_h	≥ 100	μm
Micro Heat Exchangers	100 μm ≥	D_h	≥ 1	μm

Regardless of these classifications, the proposed sizes for microchannel devices are, in general, significantly less than conventional size systems. At this small scale, the crucial question that has interested researchers and designers over the years is: Is it

possible to use conventional theories and correlations to design microchannel systems? The answer to this question was not clear for some time; however, today the vast majority of researchers believe that traditional theories and correlations hold true at the microscale when the fluid is considered a continuum.

In conventional theories, the continuum hypothesis is the major underlying assumption that is applied when performing the physical analyses. As previously discussed, this assumption may be the demarcation point where none of the conventional theories and correlations can be used at the microscale. In general, for the continuum assumption, the no-slip and no-temperature-jump boundary conditions at the fluid-solid interface apply. The Knudsen number K_n, a dimensionless parameter equivalent to the ratio of the fluid mean free path to the system characteristic length, is useful in defining the various fluid regimes. Figure 2.1 shows the range of K_n associated with the various flow regimes. Gad-el-Hak [3] summarized the flow regimes based on K_n as follows:

Euler equations (neglect molecular diffusion)		$K_n \rightarrow 0$	$(Re \rightarrow \infty)$
Navier-Stokes equations with no-slip boundary conditions		K_n	$\leq 10^{-3}$
Navier-Stokes equations with slip boundary conditions	$10^{-3} \leq$	K_n	$\leq 10^{-1}$
Transition regime	$10^{-1} \leq$	K_n	≤ 10
Free-molecule flow		K_n	> 10

In his paper, Gad-el-Hak [3] demonstrated that all flow regimes depicted in Figure 2.1 may occur in the same long microchannel. These transitions can result from a variety of operations and boundary conditions within the channel. Thus, microchannel

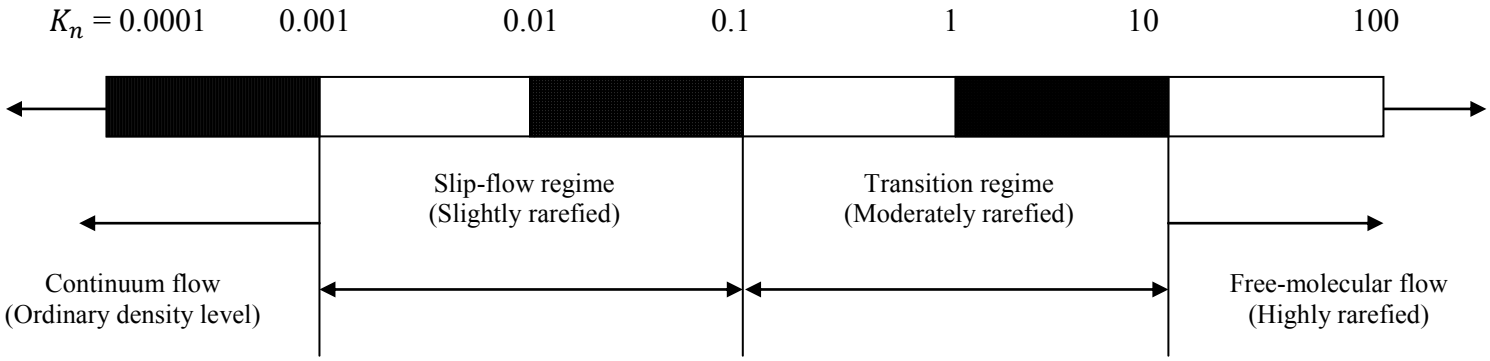

Figure 2.1 Knudsen number regimes

devices can often be designed using the continuum assumption; however, deviations from the designed operating and boundary conditions might transition the flow out of the continuum flow region, hence affecting the system thermal and hydraulic performance. The importance of the continuum assumption becomes crucial when the working fluid in the system is gaseous. As Gad-el-Hak [3] explained, the distance between gas molecules is much larger than in liquids. As an example, a cube 1 μm on a side filled with air at standard temperature and pressure contains approximately 25 million molecules. On the other hand, a cube of the same size filled with water at the same conditions contains around 34 billion molecules. This example indicates that the continuum hypothesis is typically more applicable for liquids than gases. Outside the continuum flow regime, other conditions apply such as the slip flow velocity boundary condition and the temperature jump thermal boundary condition at the fluid-solid interface [2].

Surface phenomena (or surface effects) must also be considered in the microfluidic world [3]. Gad-el-Hak [3] shows the ramifications of the high surface area to volume ratio for microchannel devices. Surface effects such as the electric double layer (EDL) can increase the friction factor and hence retard the fluid flow. Mala et al. [5] and Yang et al. [6] have shown the interaction between the free ions in polar liquids and the electrostatic charges on the channel wall. This interaction tends to increase the friction factor compared to flows free from similar effects. Kandlikar [4] suggested that as long as a liquid is the working fluid in mini- and microchannels and wall surface effects are absent, such as electrokinetic or electroosomotic forces, the flow is considered to follow the continuum theory and no significant deviation from classical theories are expected. Gad-el-Hak [3] argued that channels larger than 1 μm with liquids as working fluid can

be treated as a continuous media and classical theories can be applied. Researchers over the last three decades have manufactured and tested microchannel devices such as heat sinks. The pioneering work of Tuckerman and Pease [7] in the early 1980s laid the foundation for microchannel cooling systems. They fabricated heat sinks with rectangular microchannels using a 1 x 1 cm^2 wafer of silicon. The channels were 302 μm deep and 50 μm wide and the wall separating the channels was 50 μm thick. The working fluid in their test channels was water and they reported the ability to dissipate 790 W/cm^2 with the substrate maximum temperature raise of 71 °C above the water inlet temperature. The pressure drop was 213.7 kPa (31 psi). Since then, the microchannel heat sink field has grown significantly. Kandlikar [4] suggested that the next challenges for heat flux demand by microchannel heat sinks would be between 600 and 1000 W/cm^2. Despite, and perhaps as a result of, the revolutionary work of Tuckerman and Pease [7], researchers afterward conducted many tests on different microchannel heat sink systems that produced major discrepancies compared to conventional correlations. Sobhan and Garimella [8] compiled a comparative analysis of several studies on fluid flow and heat transfer in microchannels. They tabulated the results for each study along with the conclusions and observations of these studies. Major discrepancies between the proposed results and conventional correlations were found. While some studies suggested that conventional Nusselt numbers were predicted by the experimental results, other studies showed that the experimental Nusselt numbers were either higher or lower than conventional ones [8]. Several reasons were proposed for the discrepancies. Since there was no clear evidence that the continuum assumption was violated for most of the tested microchannels (D_h > 50 μm in most cases), the reasons for these discrepancies were

related to other factors such as: entrance and exit effects, surface roughness, nonuniformity of channel dimensions, nature of the thermal and flow boundary conditions, and uncertainties and errors in instrumentation, measurements, and measurement locations [8]. Since the channels lengths in most microchannel systems are relatively small, the assumption of thermally developed flow is questionable. Furthermore, the ambiguity of defining the proper boundary conditions can lead to major errors in experimental results. The two primary thermal boundary conditions that most practical applications might experience are the constant heat flux and constant surface temperature boundary conditions. These boundary conditions normally can be identified at the macroscale level; however, at the microscale it is relatively hard to clearly identify the imposed thermal boundary condition. Some microchannel systems might experience both boundary conditions at different locations along the channel length. The previously mentioned sources of error are thought to be the primary reasons for the discrepancies between experimental data and predictions from conventional correlations. Other sources, such as nonconstant fluid properties, electric double layer effects (EDL), and two- and three-dimensional transport effects may also lead to the reported discrepancies [9].

In the previous paragraphs, a background on heat transfer in microchannels was presented. The fundamental differences between conventional channels and mini- and microchannels based on the continuum assumption were explained. Some applications where microchannel systems can be used were illustrated. Discrepancies between experimental and conventional correlations were discussed and reasons for these discrepancies were addressed. In the next section, a brief background of the numerical studies that have been conducted on microchannel heat sinks and microchannel heat

exchangers will be presented. Results from reported numerical analyses will be presented and compared with existing experimental studies. Thermal and hydraulic assumptions used in these numerical analyses will also be discussed.

2.2 Numerical Studies of Heat Transfer in Rectangular Microchannel Heat Exchangers

Advances in computer technology and software in the last few decades has allowed these tools to become very useful in the design of many engineered systems. One of the most advanced computer tools for thermo-fluid design and analysis is computational fluid dynamics (CFD). CFD is a numerical approach to predict the flow behavior under specified conditions. Several commercial CFD software applications, such as FLUENT™ and Comsol™, are frequently used by researchers and designers. These software applications have the ability to solve the discretized governing equations, such as the Navier-Stokes equation and the energy equation, provided all boundary conditions and the initial condition are known. Hence, these computer tools can provide reasonable and accurate predictions of system performance. In heat transfer numerical analysis involving convection, the interaction of the fluid and solid in the heat transfer process must be considered concurrently. As an example, in heat exchanger numerical analysis both heat transfer in the solid and in the fluid should be taken in account. In this conjugate heat transfer analysis, both the proper fluid flow governing equation and the energy equation must be solved simultaneously. This task can be quite complex and time consuming and requires extensive computing resources. There are many times though that simplification of the boundary conditions, especially in the solid region, reduces the

solution to just the governing equations in the fluid flow domain. As an example, one of the most common thermal boundary conditions is that of constant heat flux (H1) which is practical and reasonable for many engineering applications. This boundary condition assumes that the surfaces of the conduit walls have the same heat flux imposed everywhere along the length of the channel. Technically, this thermal boundary condition (H1) is applicable in many applications such as: electric resistance heating, radiant heating, nuclear heating, and in counterflow heat exchangers having the same fluid capacity rates ($C_r \sim 1$), where C_r is the flow capacity rate ratio. When the H1 thermal boundary condition is assumed, the numerical analysis is simplified such that the flow and temperature fields need only be determined in the fluid.

Several researchers interested in heat transfer in microchannels have conducted numerical studies to predict the thermal behavior in channels with a constant heat flux boundary condition. Where some have proposed new correlations, others have proposed modifications to conventional correlations. Some of these numerical results have been compared to experimental studies and good agreement between the numerical and experimental results has been observed. Lee et al. [10] conducted a numerical study to investigate the heat transfer in rectangular microchannels. In his study, the microchannel width ranged from 194 μm to 534 μm with the channel depth being five times the width. The numerical model employed was for 3D conjugate heat transfer, accounting for conduction and convection heat transfer. The full comprehensive conjugate heat transfer analysis can be simplified to determine the flow and temperature fields inside the microchannel by assuming specific thermal boundary conditions on the microchannel walls. This assumption eliminates the need to solve for temperature in the solid region,

which makes the analysis more economical. This approach has been used extensively. Thermal boundary conditions that have been applied to conventional geometries include: constant surface temperature on the channel walls (T), constant heat flux (H1) (axially uniform heat flux with circumferentially constant temperature), and uniform wall heat flux (H2). The numerical results of Lee et al. [10] were found to be in good agreement with their equivalent experimental results. They performed several numerical studies using the three thermal boundary conditions and full 3D conjugate heat transfer. They also built microchannel heat sinks for their experimental studies that represented the proposed sizes mentioned earlier. The data extracted from the experiment were compared with the numerical studies and good agreement was found. The best agreement was found using the full 3D conjugate heat transfer model with the H1 thermal boundary condition. The numerical 3D conjugate heat transfer results almost matched the results from the simplified nonconjugate H1 analysis, indicating that the simplification of the numerical analysis using the H1 thermal boundary condition is often justified. This good agreement is a result of the combination of constant heat flux and constant surface temperature around the perimeter at a particular axial location that the H1 thermal boundary condition assumes.

Lee and Garimella [11] performed a numerical analysis to investigate laminar convective heat transfer in rectangular microchannels. In their approach, Lee and Garimella [11] assumed that the flow is hydraulically fully developing and thermally developing using the constant heat flux thermal boundary condition (H1) based on the suggestion shown by Lee et al. [10]. Additional assumptions were made to perform the numerical analysis. These assumptions were: (1) steady state, (2) incompressible fluid,

(3) laminar flow, (4) constant fluid properties, (5) negligible axial conduction and viscous dissipation, and (6) negligible radiative and natural convective heat transfer from the microchannel heat sink. The microchannels had a constant width of 200 μm and the depth ranged from 200 μm to 2000 μm in 200 μm increments, creating channels with aspect ratios ranging from 1 to 10. Since the constant heat flux thermal boundary condition was used (H1), the region of study was the inside the channel, which constituted only the flow region. Using this boundary condition on all four walls produces symmetry, and hence, only one fourth of the channel was considered. This simplification makes the simulation much faster and economical. Based on the Lee and Garimella [11] numerical simulation, a correlation was proposed for the local Nusselt number as a function of axial distance from the channel entrance and channel aspect ratio. The proposed Nusselt number correlations suggested by Lee and Garimella [11] show good agreement with the conventional correlations as well as with the experimental results from the microchannel heat sinks. The numerical simulation conducted by Lee and Garimella [11] assumed the (H1) thermal boundary condition on the four sides of the microchannel. They also proposed a different correlation for the cases where the boundary condition is imposed on only three walls of the microchannel. The agreement between the proposed correlations and conventional theory suggests that the proposed correlations based on the classical, continuum approach may be employed to predict heat transfer coefficients in microchannel systems. Note that these correlations are for laminar flow only. Further numerical investigations are needed for the turbulent flow regime with comparison to experimental studies.

Qu and Mudawar [12] conducted experimental and numerical analyses for heat transfer in a single-phase microchannel heat sink. In their numerical analysis, the 3D heat transfer characteristics were studied by solving the conjugate heat transfer problem. In their study, two heat fluxes, q'' = 100 W/cm^2 and q'' = 200 W/cm^2, were used in both the experiment and numerical simulations. The Reynolds number ranged from 139 to 1672 for q'' = 100 W/cm^2 and 385 to 1289 for q'' = 200 W/cm^2, respectively. The heat sink channels were 231 μm wide and 713 μm deep, fabricated from oxygen free copper and fitted with a polycarbonate plastic cover plate. Deionized water was the working fluid. The numerical simulations were performed under several assumptions: (1) steady fluid flow and heat transfer, (2) incompressible fluid, (3) laminar flow, (4) negligible radiation heat transfer, (5) constant solid and fluid properties except water viscosity, and (6) negligible natural convection for air trapped in the deep slots of the heat sink. The comparison between the measured temperature distribution and the predicted results from the numerical simulation showed good agreement, suggesting that the conventional Navier-Stokes and energy equations can adequately predict the heat transfer characteristics in microchannel systems.

In summary, heat transfer in microchannel heat sinks can be predicted by using a conventional heat transfer analysis assuming that the boundary conditions are reasonable approximations for the actual conditions. Note again though that the numerical simulations presented here were limited to the laminar flow region. Also, to create a reasonable comparison between the numerical predictions and experimental results, the experiment must be conducted with good instrumentation to minimize errors.

2.3 Experimental Studies of Two Single-Phase-Fluid Microchannel Heat Exchangers

Experimental studies on two-single-phase-fluid microchannel heat exchangers have been conducted by several researchers. While numerical simulations can provide a reasonable approximation of the thermal performance for microchannel heat exchangers, experiments provide the actual performance of such devices assuming the measurements of the experiments are accurate. The design of conventional and microchannel heat exchangers, in general, requires an estimate of the heat transfer coefficient. In conventional size heat exchangers, the measurement of the channel wall temperature is usually not a problem. However, in microchannel devices, it is difficult to insert temperature sensors near the microchannel walls due to the small size of the device and the size of the sensors. Placement of sensors can increase the possibility of leaks from the system and may create an alternative conduction path that affects the study. Due to this measurement complexity and inability to estimate the heat transfer coefficient, conventional correlations and numerical simulations have been used to predict the thermal performance of microchannel heat exchangers. While some authors suggest that conventional correlations and numerical simulations might be satisfactory based on comparison of the available experimental data, this suggestion is only valid for the laminar flow regime. In addition, the thermally fully developed assumption has been shown to be invalid in some microchannel studies. The thermally fully developed assumption in the turbulent region flow in conventional heat exchangers is not of a great importance as the thermal entry length is relatively small compared to the total length of most systems. However, in short channels, such as microchannel systems, the thermal

entry length can comprise 50% or more of the total channel length. These differences from the macroscale correlations can lead, in some cases, to significant differences between actual and design performance.

Kang and Friedrich [13] manufactured a counterflow microchannel heat exchanger by diamond machining. The microchannels were fabricated from thin metal foils using diamond cutting tools. These metal foils were then bonded together using a fusion bonding process. The channels were trapezoidal in shape with a hydraulic diameter of 101 μm. The total number of channels on each foil side was 1440. The working fluid was water. The Reynolds number in their experiment ranged from 72 to 492. The experimental results for the microchannel heat exchanger show a volumetric heat transfer coefficient ranging from 33.3 to 44.3 $MW/m^3/K$. This high value of heat transfer coefficient is primarily related to the high surface area to volume ratio, which was reported to be about 6875 m^2/m^3. Alm et al. [14] constructed a microchannel heat exchanger from ceramic material. The microchannel heat exchanger was used in both counterflow and crossflow by switching the inlet fluid manifold. The channels were 12.5 mm long, 250 μm wide, and the depth ranged from 320 to 420 μm depending on the heat exchanger type. The microchannel heat exchangers were fabricated by combining streolithography and low-pressure injection molding. The working fluid in the experiment was demineralized water. The mass flow rate was kept nearly equal for both sides (cold and hot) and it ranged from 80 to 120 kg/h in 10 kg/h increments. Three sets of test data were reported for the insulated counterflow, noninsulated counterflow, and the insulated crossflow heat exchangers. The experimental results for the insulated counterflow showed an effectiveness of 0.1 - 0.22 and an overall heat transfer coefficient,

calculated using the log mean temperature difference method LMTD, ranged from 8.7 to 19.5 kW/m^2/K. The noninsulated counterflow heat exchanger operated with 0.07 - 0.19 effectiveness and an overall heat transfer coefficient, using the LMTD method as in the previous test, ranged from 7 to 15 kW/m^2/K. Finally, the insulated crossflow heat exchanger showed an effectiveness of 0.1 - 0.22 and an overall heat transfer coefficient, using the LMTD method again, ranged from 7 to 22.2 kW/m^2/K.

Bier et al. [15] fabricated microchannel heat exchangers made of aluminum alloys, copper, stainless steel and titanium by surface shaping of metal foils by microtool precision cutting. These foils were then joined primarily by diffusion bonding. The rectangular channels had a cross section of 100 μm x 78 μm and a hydraulic diameter of 87.6 μm. The total number of channels for each passage was 4000. The maximum flow rate was 12.5 l/min, which was in the laminar flow regime with a mean Reynolds number of 1700 for the hot fluid and a mean Reynolds number of 800 for the cold fluid. The microchannel heat exchanger was crossflow in configuration. The overall heat transfer coefficient was 22.8 kW/m^2/K and the volumetric heat transfer coefficient was 324 MW/m^3/K. The mean logarithmic differential temperature was observed to be 59.3 K. Jiang et al. [16] conducted an experimental study of a microchannel heat exchanger made from 0.7 mm thick pure copper plates sectioned on a wire-cutting machine. The channels were 0.2 mm wide, 0.6 mm deep, and had an active length of 15 mm. The width of the solid wall (fin) between the channels was 0.2 mm. Multiple channels were fabricated on the plates and multiple plates were joined using a thin layer of soldering tin. There were 38 channels per plate and a total of 30 sheets were joined together to construct the final microchannel heat exchanger. The configuration of the microchannel was crossflow. The

area density, another name for the surface area to volume ratio, for the microchannel system was 2895 m^2/m^3. Water was used as the working fluid. The thermal performance of the heat exchanger was characterized by a maximum overall volumetric heat transfer coefficient of 38.4 $MW/m^3/K$ and a maximum overall heat transfer coefficient of 13.3 $W/m^2/K$. Thermal effectiveness between 0.1 and 0.5 was reported with corresponding net transfer units NTU ranging from 0.1 to 1.2, respectively. These results correspond to an equal flow capacity rate in both sides $C_r \sim 1$.

Cross and Ramshaw [17] constructed two crossflow microchannel heat exchangers made from a stack of 21 copper leaves with thickness of 0.5 mm. These copper leaves were etched to a depth of 0.3 mm to create the first test section while the second plate arrangement consisted of a pair of corrugated titanium plates 0.55 mm thick with the corrugation pitch and gross thickness 3 mm and 1.23 mm, respectively. Both heat exchangers had an overall volumetric heat transfer coefficient of 7.3 $MW/m^3/K$ with a Reynolds number of 1300 for the corrugated type and a much larger Reynolds number for the etched type. Hernando et al. [18] tested two single-phase liquid-to-liquid counterflow microchannel heat exchangers made from stainless steel. Deionized water was chosen as the working fluid for the experiment. Two prototypes were built: one had 100 microchannels with square cross section of 100 μm on a side and the other had 50 square microchannels of 200 μm on a side. The distance between channels in each prototype was fixed and equal to the channel side. The maximum heat rate was about 40 W for the 100 μm microchannel heat exchanger while it was about 35 W for the 200 μm microchannel heat exchanger with both types operating with a maximum Reynolds number of 1600. The overall heat transfer coefficient for both types has been calculated

using the LMTD method. For the 100 μm microchannel heat exchanger, this coefficient ranged from 3000 to nearly 5500 W/m^2/K. Correspondingly, the 200 μm microchannel heat exchanger heat transfer coefficient ranged between 2000 and 5000 W/m^2/K. Hernando et al. [18] reported that for small Reynolds number (Re < 400), the heat transfer coefficient increased rapidly with Reynolds number and then remained nearly constant afterward. The experimental thermal effectiveness and NTU for both exchangers were calculated and plotted with the analytical effectiveness and NTU given by Incorpera et al. [19] for the counterflow heat exchanger. Strong agreement between the two was observed. Hernando et al. [18] calculated the local Nusselt number as a function of Reynolds number using the correlation introduced by Lee and Garimella [11] for equivalent capacity rates for both fluids (C_r ~ 1). Their experimental thermal resistance ranged from 1.1 to 0.6 K/W, corresponding to Reynolds numbers of 25 to 900 for the 100 μm type. For the 200 μm microchannel heat exchanger, the thermal resistance ranged from 1.4 to 0.6 K/W, corresponding to Reynolds numbers of 25 to 1200.

In summary, several experimental studies on microchannel single-phase two-fluid heat exchangers have been reported in the literature. A few of the more important studies are discussed here. These studies provide a better understanding of the expected thermal performance for such devices. High overall heat transfer coefficient and overall volumetric heat transfer coefficient were reported. These positive characteristics may be attributed to the small device size, small microchannel hydraulic diameter, and the high surface area to volume ratio for the microchannels. Experimentalists have discussed the difficulty in measuring the wall surface temperatures of microchannels. Some researchers reported that conventional correlations, and other proposed correlations generated from

numerical simulations, used to predict the thermal performance of microchannel heat exchangers should be applied with caution. Thermal entry effects in microchannel systems can play a significant role in the analysis; hence, this effect should not be neglected nor omitted. Experimental thermal effectiveness and NTU were in a good agreement with the conventional theories for the experiments reported herein.

2.4 Summary

Heat transfer at the microscale level has been an interesting area of research and development for many scientists, researchers, and businesses since the 1980s. Extensive theoretical analyses have been conducted by many researchers and a state of the art review for the fluid mechanics of microdevices has been presented by Gad-el-Hak [3]. The fundamental question on whether conventional theories and correlations are valid at the microscale has essentially been answered. The conventional correlations and the continuum assumptions were shown to be valid for systems as small as 1 μm in characteristic length when operating with liquids. When analytically modeling smaller systems, or when $0.01 < K_n < 0.1$, new boundary conditions, different than those assumed in the continuum region, must be included. These boundary conditions account for the slip velocity and temperature jump at the solid-fluid interface. Numerical simulations of microchannel heat sinks and heat exchangers have shown that the conventional Navier-Stokes and energy equations can satisfactorily predict microchannel thermal performance when $K_n < 0.01$. For the most accurate modeling, thermal boundary conditions should be chosen carefully. Experimental studies on microchannel heat exchangers showed very high overall heat transfer coefficients and overall volumetric heat transfer coefficients.

These high values can be ascribed to the small size of the channels and to their high surface area to volume ratio. While experimental results were compared with numerical and theoretical predictions and reasonably good agreement was observed, careful measurements of experiment variables is crucial to justify this agreement. In addition, creating boundary conditions in the experiments that mimic those in the numerical analyses and the theoretical correlations should be emphasized. Microchannel heat exchangers have vast potential to be used in applications where high heat transfer is required with minimal weight and volumes, such as in aerospace technology.

CHAPTER 3

MODEL DESIGN

3.1 Preanalysis Using EES

In the early stage of the current study, a preliminary design analysis was conducted to predict the performance of the microchannel heat exchanger and to determine the characteristic features of the system such as substrate material, channel length, channel width, operating temperatures and pressures. Preliminary assumptions for the flow were made to simplify the first-level model used to predict the performance of the test device. These assumptions are:

(1) Steady flow.

(2) Incompressible flow.

(3) Flow is hydrodynamically fully developed.

(4) Flow is thermally fully developed.

(5) Negligible axial conduction.

(6) Negligible viscous dissipation.

(7) No phase change.

(8) Heat loss to the surroundings through radiation and natural convection is negligible.

These assumptions allow the use of conventional correlations for rectangular ducts to determine the friction factor, and hence the pressure drop, and the Nusselt number, and hence the heat transfer coefficient for different flow conditions. The validity of these assumptions will be addressed after analyzing the experimental results for this study in Chapter 5. Nusselt number Nu is a dimensionless parameter that thermal analysts use to present the heat transfer coefficient for various thermal conditions. Nu is the ratio of convection to conduction heat transfer in the system. As discussed in previous chapters, the relationship between the heat transfer coefficient and the channel hydraulic diameter is inversely proportional. In general, the smaller the channel size the larger the heat transfer coefficient and the larger the heat transfer coefficient the more heat dissipation that can be achieved. Determining the heat transfer coefficient and the corresponding pressure drop is important to thermal designers since these parameters will determine the pumping needs for a specific application to achieve a desired thermal performance.

Friction factor, f correlations, for three different regions based on flow Reynolds number, Re and the channel aspect ratio, α are used to determine the total pressure loss in the microchannels. For laminar duct flow, the product of friction factor f and Reynolds number Re is constant. For rectangular ducts this constant is dependent on the duct aspect ratio, α. Three flow regimes are considered in this analysis: laminar flow with Reynolds number $Re_{Dh} < 2300$, turbulent flow with $2300 < Re_{Dh} < 20000$ and fully turbulent flow with $Re_{Dh} > 20000$. For the laminar flow case, the data presented from [20] are used to create a cubic polynomial fit for fRe. For the other two flow conditions, equations (3.2, 3.3) in Table 3.1 are used from [20] to predict the friction factor. These correlations are

programmed as conditional statements in the code and are executed based on the Reynolds number value. The thermal behavior is predicted using two Nusselt number correlations for two different flow regimes. For duct flow in the laminar regime, Nu is a function of the channel aspect ratio. A cubic polynomial fit of the $Nu(\alpha)$ data given in Table 8.1 in [20] for the uniform heat flux thermal boundary condition is used to predict the Nusselt number in the laminar region. For the turbulent region, the correlation provided by Gnielinski [20] is used to predict the Nusselt number. These correlations are programmed as conditional statements in the code and are executed based on the calculated Reynolds number. Table 3.1 presents the hydrodynamic and thermal correlations used as conditional statements in the EES code used for the current research. EES, or Engineering Equation Solver, is a commercial software package designed to solve systems of nonlinear equations using the Newton-Raphson method. The package includes built-in properties for a wide variety of substances in solid, liquid, and gaseous states, making it ideal for modeling thermal systems. As indicated by the correlations in Table 3.1, Re and α need to be known to determine the output. The program for the current study was designed to have the characteristic dimensions of the channels, such as channel length, width, depth and the wall thickness between the channels, as inputs. Since the material used to create the channels is double-sided Kapton® tape, which has a specific thickness of approximately 101.6 μm (4 mils), the height of the two channels is the same and fixed. In addition, the mass flow rates for both the cold and hot fluids and the inlet temperatures and the outlet pressures are chosen as input arguments. Since the model consists of a set on nonlinear equations, specific known and unknown variables may be changed for each solution. The only requirement is that the number of equations

Table 3.1 Hydrodynamic and thermal correlations used in EES pre-design code

Model Conditional Statement Hydrodynamic Correlations	Condition Range	Equation No.
$f = \frac{95.705 - 50.41\,\alpha^3 + 132.75\,\alpha^2 - 121.217\,\alpha}{Re_{Dh}}$	$Re_{Dh} < 2300$	(3.1)
$f = 0.316\,Re_{Dh}^{-0.25}$	$2300 < Re_{Dh} < 20000$	(3.2)
$f = 0.184\,Re_{Dh}^{-0.2}$	$Re_{Dh} > 20000$	(3.3)
Thermal Correlations	Condition Range	Equation No.
$Nu_{Dh} = 7.496 - 10.06\,\alpha^3 + 22.726\,\alpha^2 - 17.195\,\alpha$	$Re_{Dh} < 2300$	(3.4)
$Nu_{Dh} = \frac{\left[\left(\frac{f}{8}\right) Pr(Re_{Dh} - 1000)\right]}{\left[1 + 12.7\left(\frac{f}{8}\right)^{1/2}(Pr^{2/3} - 1)\right]}$	$Re_{Dh} > 2300$	(3.5)

is equivalent to the number of unknowns. Table 3.2 presents the EES model input arguments. It was assumed that the outlet pressures for both flows are atmospheric pressure. Fluid properties in each channel are evaluated at the mean channel fluid temperature. To facilitate the solution of the highly coupled set on nonlinear equations, fluid properties are initially estimated based on an approximation of the average channel fluid temperature. After the code is executed and a solution is obtained, these properties are evaluated based on the calculated mean fluid temperatures in an iterative scheme until the solution has converged. Using the mass flow rate values and equation (3.12) allows the fluid mean velocities to be determined. The velocities are then used to determine the Reynolds number for both sides (Eq. (3.13)). After determining the Reynolds numbers, the conditional statements are executed and the friction factor and Nusselt number are calculated (Eq. (3.1) – (3.5)). Finally, equations (3.14) through (3.36) are executed. Figure 3.1 presents the iteration scheme of the EES code. Table 3.3 presents the EES model equations, in addition to the conditional statements, that are used to predict the hydrodynamic and thermal performance of the microchannel heat exchanger. Equations in Table 3.3 represent the typical order in which they are executed. As noted above, using EES allows the equations to be listed in any order, so long as the unknowns are equivalent to the number of equations. Since the input arguments from Table 3.2 are entered as known variables, Equations (3.7) to (3.13) can be processed immediately. As mentioned earlier, it is important to predict the pressure drop expected in the device. This information helps determine possible upper limits on key parameters, such as flow rates and Reynolds numbers, for the two fluids. Knowledge of these upper limits can then be applied during testing to try to limit system pressures so that device integrity is assured.

Table 3.2 EES model input arguments

Model Input		Description	Unit
Channel geometry	W_c	Cold channel width	m
	W_h	Hot channel width	m
	H	Channel height	m
	H_{fin}	Fin height	m
	L_c	Cold channel length	m
	L_h	Hot channel length	m
	δ_w	Separation wall thickness between channels	m
Material Properties	k_k	Kapton® tape thermal conductivity	W/m/K
	k_g	Glass thermal conductivity	W/m/K
	k_{cu}	Copper thermal conductivity	W/m/K
Hydrodynamic and thermal conditions	$\dot{m}_c$	Cold fluid mass flow rate	kg/s
	$\dot{m}_h$	Hot fluid mass flow rate	kg/s
	$P_{c,out}$	Cold fluid outlet flow pressure	kPa
	$P_{h,out}$	Hot fluid outlet flow pressure	kPa
	$T_{c,in}$	Cold fluid inlet temperature	°C
	$T_{h,in}$	Hot fluid inlet temperature	°C

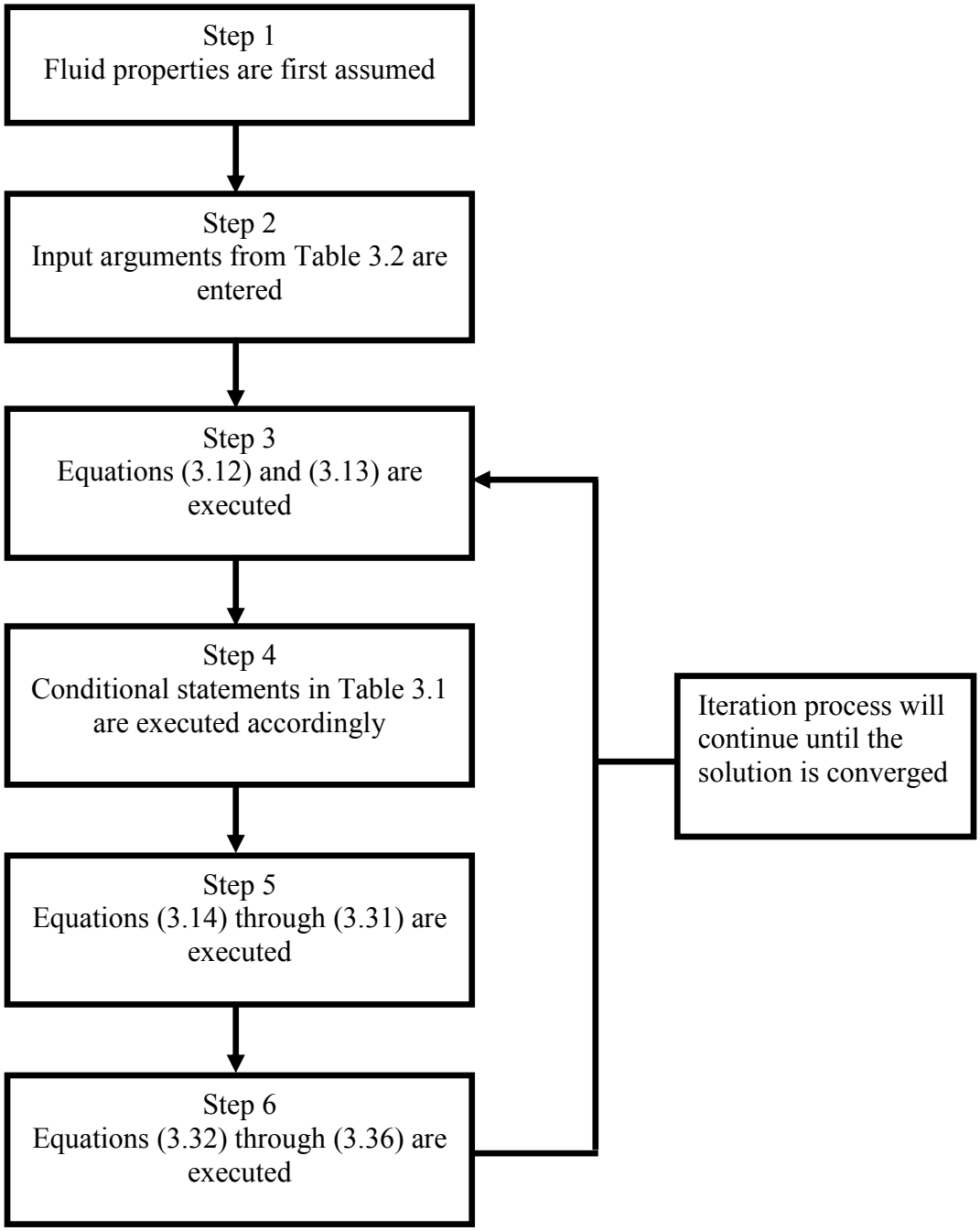

Figure 3.1 Iteration scheme for the EES code

Table 3.3 EES model equations

Model Equation	Unit	Equation No.	Model Equation	Unit	Equation No.
$\alpha_i = \frac{H}{W_i}$		(3.7)	$U_k = \frac{1}{\left(\frac{1}{h_c} + \frac{\delta_w}{k_k} + \frac{1}{h_h}\right)}$	W/m^2/K	(3.15)
$A_i = W_i H$	m^2	(3.8)	$U_g = \frac{1}{\left(\frac{1}{h_c} + \frac{\delta_w W_c}{k_g H_{fin}} + \frac{1}{h_h}\right)}$	W/m^2/K	(3.16)
$A_{i,ht} = 2W_i L_i \times 10^{-4}$	cm^2	(3.9)[1]	$U_{cu} = \frac{1}{\left(\frac{1}{h_c} + \frac{\delta_w W_c}{k_{cu} H_{fin}} + \frac{1}{h_h}\right)}$	W/m^2/K	(3.17)
$A_{fin} = H_{fin} L_i$	m^2	(3.10)	$C_i = \dot{m}_i Cp_i$	W/K	(3.18)
$D_{h,i} = \frac{2(W_i * H)}{(W_i + H)}$	m	(3.11)	$C_{min} = \min(C_c, C_h)$	W/K	(3.19)
$V_i = \frac{\dot{m}_i}{A_i \rho_i}$	m/s	(3.12)	$C_{max} = \max(C_c, C_h)$	W/K	(3.20)
$Re_i = \frac{\rho_i V_i D_{h,i}}{\mu_i}$		(3.13)	$C_r = \frac{C_{min}}{C_{max}}$		(3.21)
$h_i = \frac{Nu_i \, k_i}{D_{h,i}}$	W/m^2/K	(3.14)	$NTU_j = \frac{U_j A_{i,ht}}{C_{min}}$		(3.22)

Table 3.3 Continued

Model Equation	Unit	Equation No.	Model Equation	Unit	Equation No.
$\varepsilon = \frac{1 - e^{(-NTU(1-C_r))}}{1 - C_r e^{(-NTU(1-C_r))}} \; for \; C_r < 1$ $\varepsilon = \frac{NTU}{1 + NTU} \qquad for \; C_r = 1$		(3.23)	$\bar{T}_i = \frac{T_{i,in} + T_{i,out}}{2}$	K	(3.30)
$q_{max} = C_{min}(T_{h,in} - T_{c,in})$	W	(3.24)	$\bar{P}_i = \frac{P_{i,in} + P_{i,out}}{2}$	Pa	(3.31)
$\varepsilon = \frac{q_i}{q_{max}}$		(3.25)	ρ_i = Density(Water, T=$\bar{T}_i$,P=$\bar{P}_i$)	kg/m^3	(3.32)
$q_i'' = \frac{q_i}{A_{i,ht}}$	W/cm^2	(3.26)	μ_i = Viscosity(Water, T=$\bar{T}_i$,P=$\bar{P}_i$)	Pa-s	(3.33)
$q_i = \dot{m}_i C_{p,i} \Delta T_i$	W	(3.27)	k_i = Conductivity(Water, T=$\bar{T}_i$,P=$\bar{P}_i$)	W/m/K	(3.34)
$\Delta P_i = \frac{f_i L_i V_i^2 \rho_i}{2D_{h,i}} \times 10^{-3}$	kPa	(3.28)	$C_{p,i}$ = CP(Water, T=$\bar{T}_i$,P=$\bar{P}_i$)	J/kg/K	(3.35)
$P_{i,1} = \Delta P_i + P_{i,2}$	kPa	(3.29)	Pr_i = Prandtl(Water, T=$\bar{T}_i$,P=$\bar{P}_i$)		(3.36)

1 The heat transfer surface area for the channel is defined as the top and bottom channel surface areas, made of the substrate material only, neglecting the Kapton® tape surface area. More details regarding the channel heat surface area definition are presented in Chapter 4.

* i = c (cold), h (hot) and j = k (Kapton® tape), g (glass), cu (copper).

The traditional Darcy-Weisbach equation for pressure drop is used with the hydraulic diameter for the length scale and the previously determined friction factor. It must be mentioned that this pressure drop does not take into account the entrance and exit pressure losses; thus, the computed pressure drop is due solely to frictional losses in the channel. The Nusselt numbers are then used to calculate the heat transfer coefficients for both fluids. Afterward, these calculated heat transfer coefficients are used to calculate the overall heat transfer coefficient for the heat exchanger. In this study, the overall heat transfer coefficient for the heat exchanger is determined using a thermal resistance analogy. Figure 3.2 is a schematic drawing for the proposed configuration of the heat exchanger. To calculate the overall heat transfer coefficient, a one-dimensional thermal circuit is created, assuming steady state interfluid heat transfer only occurs through the Kapton® tape. Equation (3.37) presents the general mathematical expression for the overall heat transfer coefficient that was used to derive Equations (3.15), (3.16), and (3.17).

$$U = \frac{1}{R_{tot}A} \tag{3.37}$$

where R_{tot} is the total 1D thermal resistance of the heat path and A is the corresponding heat transfer surface area. A more detailed discussion of the overall heat transfer coefficient analysis for the cases in Equations (3.15), (3.16), and (3.17) is presented next. Figure 3.3 illustrates the thermal resistance path for this case. Since this 1D analysis was applied to the Kapton® tape wall, all the area terms in the resistance path are equal and can be eliminated. The mathematical expression for this 1D model is presented in Eq.

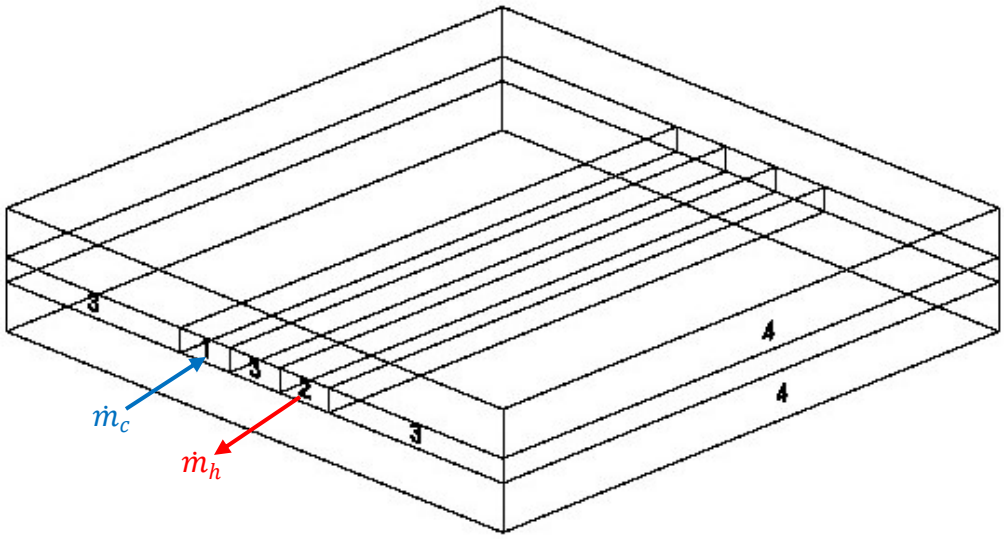

Figure 3.2 Schematic of the microchannel heat exchanger, where (1) is channel 1, (2) is channel 2, (3) is the Kapton® tape and (4) is the substrate

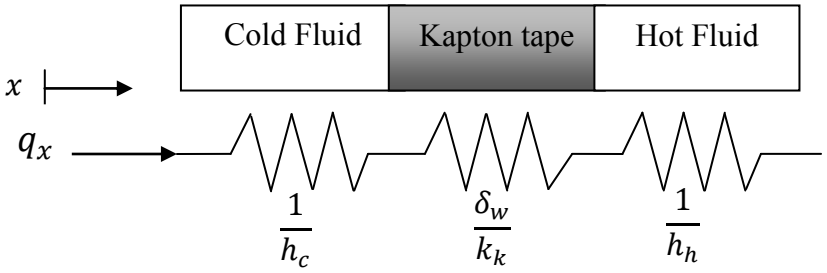

Figure 3.3 Thermal resistance path for 1D heat transfer through Kapton® tape

(3.15) in Table 3.3. Double-sided Kapton® tape has been used in the automotive industry and in other applications as a thermal insulating material. However, since the distance between the cold and hot channels is very small (~ 1 mm), and the temperature gradient through the tape is relatively large, it was sensible to expect that a reasonable amount of heat would be transferred through the tape regardless of its low thermal conductivity (~ 0.12 W/m^2/K). Cold and hot mass flow rates are varied in a set of 100 runs to represent different Re ranging from 200 to 6000. The hot and cold fluid inlet temperatures are set to 100 °C and 0 °C, respectively. The channels are assumed to be 2 cm long, 1 mm wide and 101.6 μm in height. Once the outlet temperatures are calculated, Eq. (3.27), Eq. (3.30), and (3.31) are executed to determine the mean fluid temperature and pressure for each side, which are then used to determine the fluid properties. Data from these trials for the heat exchanger effectiveness for the first case (1D through Kapton® tape only) show very poor thermal performance, with a maximum effectiveness less than 0.01 for C_r = 0.25. This unfortunate thermal performance is due to the low thermal conductivity of the Kapton® tape and the simplified 1D assumption. Figure 3.4 presents the $\varepsilon(NTU)$ performance for the Kapton® tape 1D analysis. This initial 1D analysis is modified by assuming all the heat transfer occurs within the substrate instead of the Kapton® tape material. The analysis is similar to the 1D Kapton® tape case with a minor change to the resistance of the solid region in the thermal resistance circuit shown in Figure 3.3. In addition, the areas in the thermal circuit analysis in Figure 3.3 are no longer the same and, hence, they cannot be eliminated. The cold and hot channels are set to have the same dimensions; thus, their areas are the same. Taking advantage of the symmetry of the system allows half of the system to be analyzed. Figure 3.5 illustrates the new thermal

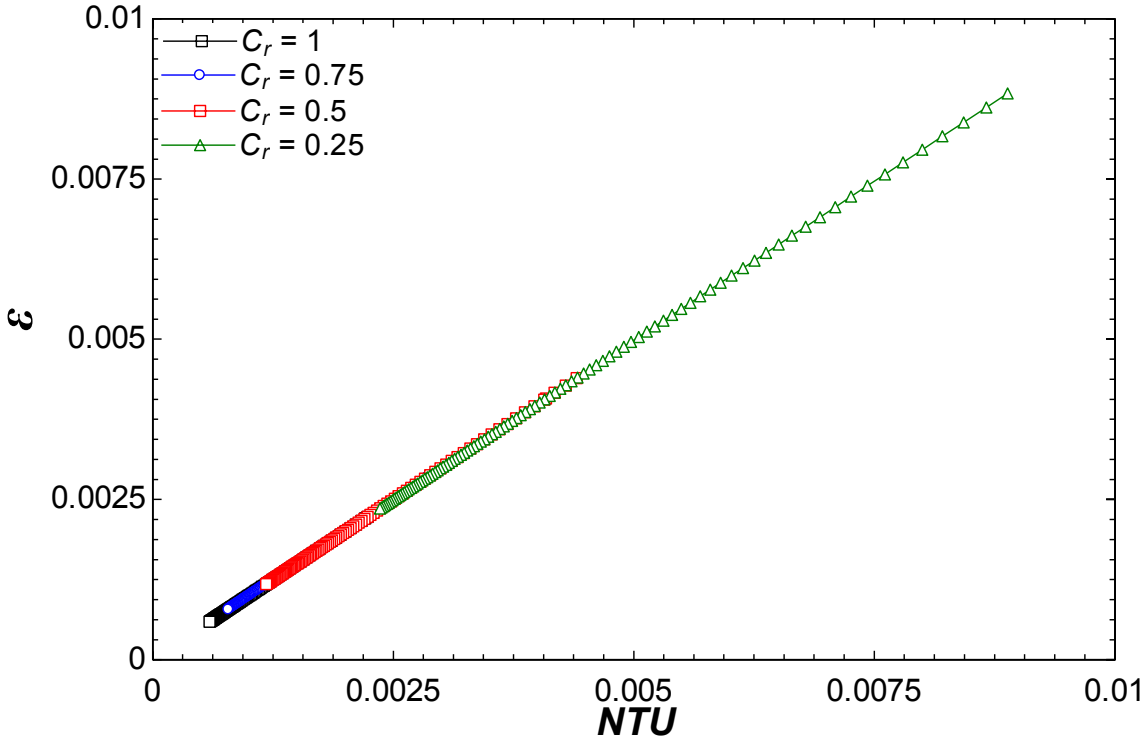

Figure 3.4 Thermal performance of the microchannel heat exchanger based on the 1D Kapton® tape analysis

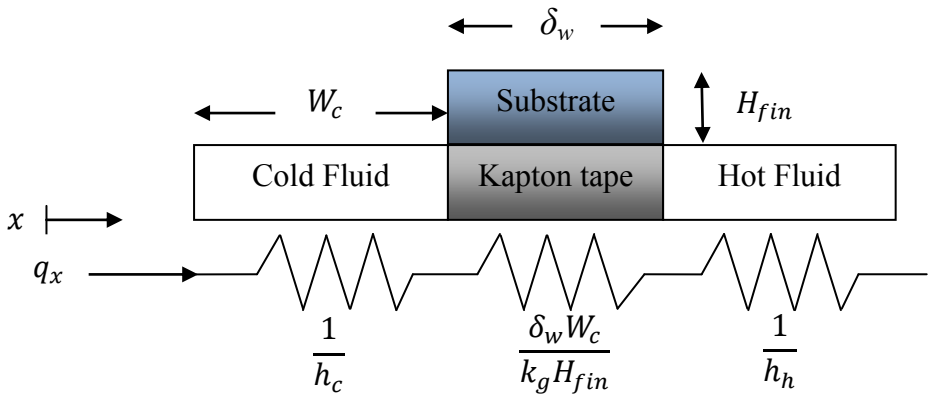

Figure 3.5 Modified thermal circuit analysis

resistance circuit for the modified analysis. Note that heat transfer surface areas for the two channels are equivalent; they are defined in Eq. (3.9) in Table 3.3. The rest of the analysis is conducted as with the previous 1D analysis. The only change is the definition of the overall heat transfer coefficient based on the modified thermal circuit. Glass thermal conductivity is set at 1.4 W/m/K, as suggested from [20] for Pyrex glass. The height of the glass substrate is set to 3 mm and the length of the glass substrate is the same as the channel length. Results from this analysis indicate an improved thermal performance over that of just the Kapton® tape; however, the maximum effectiveness of the heat exchanger is still less than desirable at 0.22 for C_r = 0.25. Given that the inlet temperatures for both fluids are near the extreme values for single-phase flow, this thermal performance is not desirable. Figure 3.6 presents the $\varepsilon(NTU)$ performance for the glass substrate. Finally, the same analysis was conducted using a different substrate material. Copper was chosen as the heat exchanger substrate material for this analysis since it has a very high thermal conductivity (k ~ 400 W/m/K). Using the same dimensions as for the glass substrate case, results for the copper substrate predict a more reasonable range of effectiveness. Figure 3.7 shows the heat exchanger effectiveness along with the corresponding NTU for different capacity rate ratios for the copper heat exchanger. These results suggest that fabricating such a heat exchanger from copper is a feasible option and worth testing. Different channel widths (W_c < 1 mm) lead to different aspect ratios for the channels. Using the same model for the copper substrate with smaller widths also indicates an acceptable range of thermal effectiveness. The three 1D thermal analyses suggest that the maximum thermal effectiveness can be achieved only by using copper as the substrate material. It is also clear that constructing a heat exchanger from

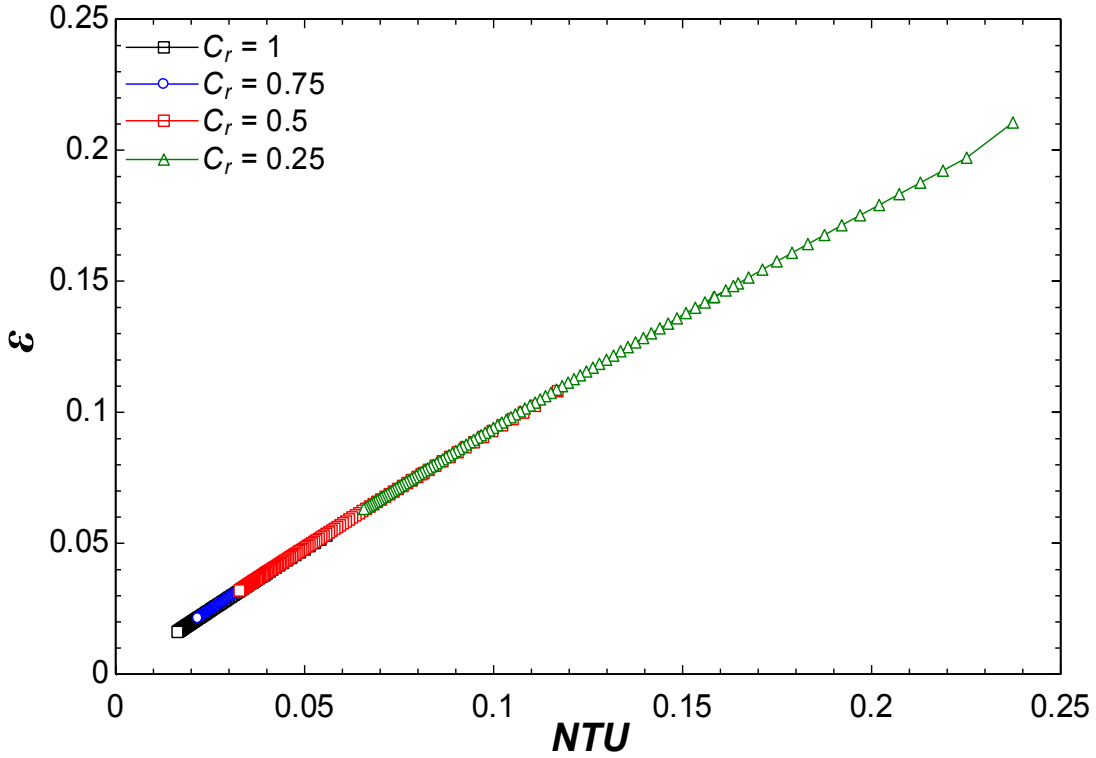

Figure 3.6 Thermal performance of the microchannel heat exchanger based on the 1D glass substrate

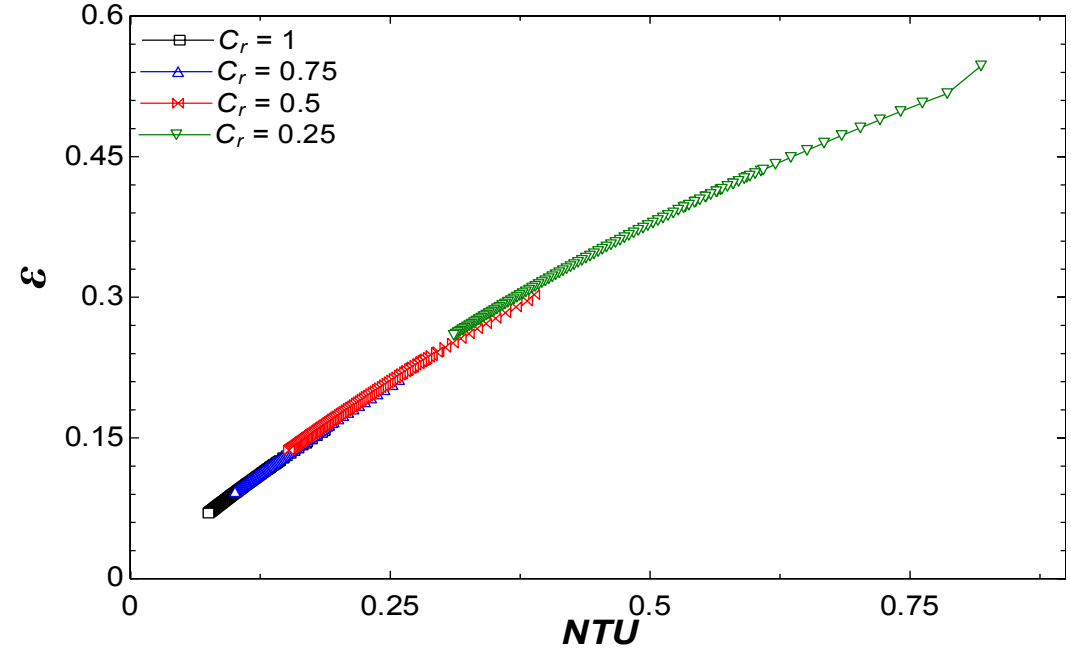

Figure 3.7 Thermal performance of the microchannel heat exchanger based on the 1D copper substrate

Kapton® tape with a glass substrate is not advantageous. Hence, copper was chosen as the substrate material for the microchannel heat exchanger. The associated pressure drop for the desired thermal performance is dependent on flow Reynolds number. Since the heat transfer coefficient is larger in the turbulent flow region, it is desirable that both flows are in this regime. For equivalent mass flow rates in the two channels, the cold fluid Reynolds number Re_c will be less than the hot fluid Reynolds number Re_h. This difference is due to the differences in kinematic viscosity for the two fluids resulting from the differences in the fluid mean temperatures. As $Re_c < Re_h$, the pressure drop in the cold channel will be less than that in the hot channel. Thus, even in parallel flow, and more so in counterflow, a pressure difference occurs in the transverse direction along the channel wall separating the two fluids. For this reason, the channel length has to be carefully calculated to address the pressure drop and force imbalance on the channel separating wall. Longer channels have larger heat transfer areas; however, as in equation 3.27, the pressure drop will be greater. A higher inlet pressure may require more costly equipment to achieve. The driving potential for leaks, both to the surroundings and between fluid channels, increases with pressure, which is a concern for xurographic channel systems. One of the advantages of using glass material instead of the copper is its transparency. Theoretically, internal leaks can be observed through glass while that is not possible for the copper substrate. External leaks will be evident by the formation of droplets around the perimeter of the heat exchanger. While glass may be advantageous for leak detection, it provides poor thermal performance, as shown previously. On the other hand, in early experiments glass was shown to have better adhesion with the Kapton® tape than copper. This makes the choice of the pressure drop in the copper heat

exchanger of a great importance. Using the data generated in the EES code for the copper substrate, the best channel length that will enable a wide range of Reynolds numbers and an acceptable pressure drop is about 2 cm.

In summary, it is concluded that the best option for the substrate material is copper. Channels are designed with different widths (1 mm, 0.75 mm, 0.50 mm, and 0.35 mm) to assess thermal performance as a function of that parameter. It is shown that a reasonable range of effectiveness can be achieved for those channel sizes. In addition, the channels lengths are chosen so a wide range of Reynolds numbers can be achieved with manageable pressure drops.

3.2 Data Reduction Program Using Matlab

A data reduction program was created after the pre-design stage. The data reduction program is coded in Matlab®. The program is used as the primary tool to calculate and analyze the experiment outputs. Program validation was accomplished by comparing output with that generated by the EES code for equivalent conditions. Inputs to the code include all measured quantities, such as inlet and outlet temperatures and pressures, all channel dimensions, mass measurements, and time. From these data, average fluid temperatures in each channel are used with material property correlations to determine the fluid densities, dynamic viscosities, specific heat capacities, and thermal conductivities. Fluid properties are calculated using Matlab functions with absolute temperature, in Kelvin, and absolute pressure, in MPa, as input arguments. These built-in functions are provided from [24]. The data reduction program is explained in more detail

in Chapter 4. It was also used as the foundation for a computational pre-test uncertainty analysis.

3.3 Pretest Uncertainty Analysis

Uncertainty analysis, especially before conducting experiments, is a key step that helps determine the feasibility of the experiment and the acceptability of equipment and procedures. When experiments are conducted, system variables such as temperatures and pressures are measured using instruments such as thermocouples and pressure transducers. Despite the tremendous advancement in the technology of instrumentation, all instruments have some error, which is quantified statistically with measurement uncertainty. The measurement uncertainties propagate through the data reduction procedure to create uncertainties in the reported data. The pretest uncertainty helps identify the sources of high uncertainties such that the instrumentation and procedures used to determine output data may be improved.

Moffat [25] developed a method to determine the uncertainties of desired data from any test during the design stage. This methodology is used here. To determine the uncertainty in any output quantity R that is a function of measured variables $x_1, x_2, \ldots, x_n$, equation (3.37) is applied.

$$\delta R = \left[\left(\frac{\partial R}{\partial x_1}\delta x_1\right)^2 + \left(\frac{\partial R}{\partial x_2}\delta x_2\right)^2 + \cdots + \left(\frac{\partial R}{\partial x_n}\delta x_n\right)^2\right]^{(1/2)} \tag{3.37}$$

δR is the total uncertainty, δx_1 to δx_n are the uncertainties in the physical variable measurements, and the partial derivatives are called the sensitivity coefficients. In this method, the sensitivity coefficients are evaluated from the data reduction program using a central-difference approximation presented in equation (3.38):

$$\frac{\partial R}{\partial x_i} \approx \frac{R[x_1,x_2,\ldots(x_i+\varepsilon_o),\ldots x_n]-R[x_1,x_2,\ldots(x_i-\varepsilon_o),\ldots x_n]}{2\varepsilon_o} \tag{3.38}$$

Inputs such as masses, time, inlet and outlet pressures, inlet and outlet temperatures and heat exchanger dimensions for specific flow conditions are entered. The program then calculates the output parameters, such as Re, q and ε along with their uncertainties by first calculating the values of R_{i+1}, for Re, q, ε, etc., for the positively perturbed values (by ε_o) of the physical measured variables x_i. Second, these results are then returned to the main program and added to the negatively perturbed values R_{i-1}, calculated in the same manner. The sensitivity coefficients are determined next using equation (3.38). Finally, the products of the sensitivity coefficients and the measurement uncertainties δx_i are calculated. Manufacturer's data are applied directly for the measurement uncertainties. These data are provided in Table 3.4. The pretest uncertainty analysis uses the data in Table 3.4 and inputs determined from typical operating conditions as predicted from the EES predesign program. The analysis indicates that the current experiment can be conducted with uncertainties that are acceptable. No modification to the experiment setup, instrumentation, or data acquisition is required. Table 3.5 presents an example of a portion of the pre-test uncertainty analysis for the cold fluid Reynolds number Re_c. As

Table 3.4 Instrument uncertainties

Measurement	Unit	Uncertainty
Temperature	°C	± 0.1*
Setra pressure sensor	psi	± 0.15% of full scale
Mass balance	g	± 0.01
Lab View internal clock	s	± 0.01
Channel length	μm	± 2.0**
Channel width	μm	± 2.0**
Channel height	μm	± 0.5**

*If thermocouples are calibrated otherwise manufacturer uncertainty is ± 1 °C
**The uncertainties of these measurements are consistent with those determined by Nguyen [21].

Table 3.5 Pretest uncertainty analysis example

Pretest uncertainty analysis Output measured = Re_c = 276.22 Uncertainty interval = δRe_c = ± 4.9177 Total Uncertainty = 1.7804 %					
Input argument x	Value	Input argument unit	Measured uncertainty δx	Sensitivity coefficient $\frac{\partial Re_c}{\partial x}$	Relative uncertainty $\left(\frac{\partial Re_c}{\partial x}\delta x\right)^2$
$T_{c,in}$	25	°C	± 0.1* °C	2.1120e+000	4.4605e-002
$T_{h,in}$	100	°C	± 0.1* °C	0	0
$T_{c,out}$	91.85	°C	± 0.1* °C	2.1120e+000	4.4605e-002
$T_{h,out}$	33.25	°C	± 0.1* °C	0	0
$m_{c,1}$	0.1	g	± 0.01 g	-3.4527e+002	1.1921e+001
$m_{h,1}$	0.1	g	± 0.01 g	0	0
$m_{c,2}$	0.9	g	± 0.01 g	3.4527e+002	1.1921e+001
$m_{h,2}$	0.9	g	± 0.01 g	0	0
t_1	1	s	± 0.01 s	2.5111e+001	6.3056e-002
t_2	12	s	± 0.01 s	-2.5111e+001	6.3056e-002
W_c	0.001	m	± 2x10^{-6} m	-2.5074e+005	6.2873e-002
W_h	0.001	m	± 2x10^{-6} m	0	0
H	0.0001016	m	± 0.5x10^{-6} m	-2.5074e+005	6.2873e-002
L_c	0.02	m	± 2x10^{-6} m	0	0
L_h	0.02	m	± 2x10^{-6} m	0	0
δ_w	0.001	m	± 2x10^{-6} m	0	0

*If thermocouples are calibrated otherwise manufacturer uncertainty is ± 1 °C

will be explained in Chapter 4, the mass flow rate was determined by measuring the mass of the accumulated fluid in the container on the mass balance and dividing by the time elapsed. As shown in Table 3.5, some input arguments affect the Reynolds number uncertainty while others have no effect. This is due to the definition of the Reynolds number. The cold fluid mass flow rate and density and the cold channel height and width directly affect the cold fluid mean velocity. Uncertainties in these parameters propagate through the calculation of the cold fluid mean velocity uncertainty. Also, the cold fluid properties, such as density and dynamic viscosity, are determined using the cold fluid average temperature. This introduces additional uncertainties into the output parameters, such as Re_c. Table 3.5 provides the relative uncertainty of the calculated parameter (δRe_c) resulting from each individual input argument. The analysis indicates that the mass measurements have the greatest impact on δRe_c. Given the fact that the relative uncertainty of Re_c is low, the method assumed to determine the mass flow rate (bucket/stopwatch) is deemed acceptable. The uncertainty for the temperature measurements (± 0.1 °C) assumes well-calibrated thermocouples. If the manufacturer's uncertainty (± 1.0 °C) is applied instead, δRe_c will be adversely affected. The methodology described here is also used in the post-test uncertainty analysis. The only changes required are updated values for δx_i that include precision errors. These changes are described in more detail in Chapter 4. Actual experimental outcomes along with their uncertainties are presented in Chapter 5.

CHAPTER 4

FABRICATION METHODS AND TEST PROCEDURES

In this chapter, the test section design, fabrication process using xurography, preparation of the substrates and the final assembly process are presented. In addition, the test apparatus and data acquisition system are introduced. Furthermore, the test loop and test procedures are explained. Finally, the data reduction program used to calculate the final results is presented.

4.1 Test Section Design

Designing the pattern for the channels and manifolds is the first step in fabricating the microchannel heat exchanger. Different software programs can be utilized as design tools for this purpose, such as *Adobe Illustrator*, *SolidWorks*, and *AutoCAD*. The main advantage of using *Adobe Illustrator* is the compatibility and connectivity with the cutting plotter. However, in the current study, *AutoCAD* is the design tool used to draw the channel pattern and the design file is saved in *.dxf* format in order to use it in *Adobe Illustrator* later. In the current study, four different designs are created, representing four different aspect ratios. As mentioned earlier, the microchannel heat exchanger is constructed by cutting the channel pattern into the double sided adhesive Kapton® tape

and then sandwiching and bonding the tape between two square substrates to create the final assembly. Hence, the channel shape is rectangular in cross section with the substrate surfaces providing the top and bottom walls of the channels and the cut tape providing the side walls. Since the thickness of the Kapton® tape is fixed, the channel height is fixed (4 mils ~ 101.6 μm). Due to this constraint, the only way to change aspect ratio is by changing the channel width.

Two straight rectangular channels, for the cold and hot fluids, with a separation wall between them of 1 mm, are selected to represent the heat exchanger. The thickness of the separation wall between the hot and cold channels is selected after considering its effect on interchannel leaks and interfluid heat transfer. Results from the pre-design EES code indicate the thermal performance of the device is not affected appreciably by the wall thickness. In addition, an experimental study for two different microchannel systems having the same channel length, width, and operating conditions with two different wall thicknesses (1 mm and 0.5 mm) has been conducted. The study shows that the heat rate is increased by only 10% for the smaller wall thickness. Since the difference in thermal performance between the two thicknesses was not significant, the current design incorporates a 1 mm separation wall between the cold and hot channels to mitigate the risk of any internal leak between the channels. As discussed in Chapter 3, the length of the channels was selected to be 2 cm in order to reach a fairly high Reynolds number with acceptable pressure drops. The inlet and the outlet ports in the design have to be separated to accommodate the nanoports. Additionally, it is desirable that the fluid temperature sensors are located as close as possible to the inlets and outlets of the straight channels. Thus, there are conflicting design constraints on locating the inlet and outlet

ports. To facilitate temperature measurements at the desired location, a special T-shape connector was purchased from IDEX for mounting on each nanoport. This arrangement allows the thermocouples to be inserted in the T-connection to measure the temperature. The distance between nanoports also has to be sufficient to allow the T-connectors to be tightened into the nanoport threads. All of these constraints were considered when selecting the inlet and outlet locations shown in Figure 4.1. Since the flow configuration tested in the current study is counterflow, there is always a relatively high pressure difference between the fluid channels. This pressure difference exerts a net force on the separation wall which could lead to adhesion failure and internal leakage between the two channels. Also, higher fluid temperatures can adversely affect the bonding process. For this reason, a pressure test has been conducted to determine the pressure limits for the separation wall. Three different wall thicknesses (1 mm, 0.5 mm, and 0.3 mm) were tested. One channel had two ports open to atmospheric pressure; the other channel had a single port for a pressure source. This single port allowed fluid to be introduced into the channel, exerting a force on the separation wall. In this test, a dye was used to detect when an internal leak started. The onset of leakage was determined by gradually increasing the pressure in the single-port channel. The failure pressure for the three test channels is shown in Table 4.1. Note that these pressure failure tests were conducted using glass substrates without any external clamping system, which would add additional bonding force. Since the adherence quality of the tape depends on the substrate material and surface preparation, these results are likely to differ for other substrates; however, it was assumed that these results are reasonable for the copper substrates. The heat exchanger is also susceptible to leakage through the adhesive between the channels and

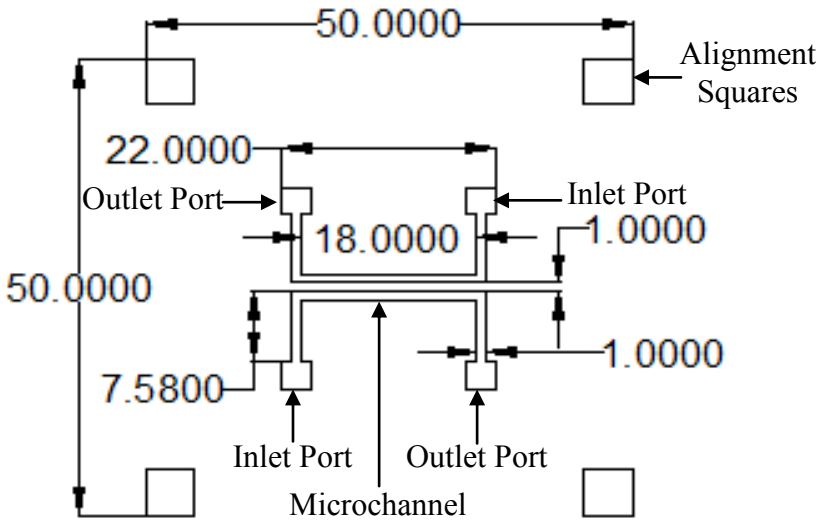

Figure 4.1 Final test section design (not to scale, all dimensions are in mm). Channel width is 1 mm

Table 4.1 Failure pressures for different separation wall thicknesses

Separation wall thickness [μm]	Failure pressure MPa (Psi)
1000	~ 1.69 (245)
500	~ 1.09 (158)
300	~ 0.76 (110)

the ambient pressure outside the device. This problem is controlled with a clamping system that provides mechanical force to the top and bottom of the device. Another likely region to experience leaks is the bond between the nanoports and copper substrate. The adherence between the nanoport and the substrates depends highly on the substrate material and the surface preparation.

4.2 Inlet and Outlet Port Drilling and Surface Preparation

In this section, the procedure for drilling the inlet and outlet ports in the substrates is presented. Also, surface finish and nanoport bonding to the substrates is introduced. The substrates are square in shape with sides of 5 cm (2 in) and thickness of 3 mm (0.12 in). Once the channel pattern is drawn, the drawing is plotted on paper and placed on top of the substrate. Aligning the four squares on the corners of the drawing with the corners of the substrates allows the inlet and outlet ports to be located on the substrate. With these locations known, the drilling process is started. For glass, special diamond coated drill bits are used due to the brittleness of the material. The glass plates are immersed in a water bath during the drilling process to reduce the risk of cracking and to cool the drill bit. In addition, an intermittent drilling sequence is recommended to reduce the risk of cracking and to reduce drill bit wear. Once the ports are drilled, the glass plates are cleaned with distilled water and isopropyl alcohol. When the glass surfaces are clean and dry, the nanoports can be installed. The nanoports (IDEX) are made of PEEK material that uses special adhesive rings to bond with other materials. Nanoport adhesive rings (IDEX) are used to bond the nanoports to substrates such as silicon wafers and glass. These adhesive rings are placed between the nanoport base and the substrate surface. In

the current device, the nanoport adhesive rings are placed over the drilled ports and then the nanoports are aligned with the ports and clamped using binder clips. Afterward, the glass plates along with the clamped nanoports are cured in an oven heated to a temperature between 166 °C and 177 °C for an hour. Finally, the glass plates are cooled in room temperature air. It should be noted that PEEK nanoports can undergo frequent heating cycles, which can make the bottom surface uneven. This surface irregularity may affect the bond quality if a nanoport is reused. It is highly recommended that the curing process for all nanoports be conducted simultaneously. Comprehensive details about the glass drilling process and nanoports adhering procedures can be found in [21, 22, and 23]. When the substrate is made of copper, special surface preparation must be performed. First, the substrate is polished with a spinning disk polishing machine to smoothen the surfaces. Polishing is performed in two steps: step one consists of a polishing process with sand paper of 30 μm grit and step two is polishing with a finer sand paper of 15 μm grit. The surfaces are then cleaned with distilled water and isopropyl alcohol. For strong bonding of the nanoports to the copper substrates, it is desirable to have a rough copper surface. Bond strength of the nanoport adhesive rings to the copper was found to be much less than that for glass. It was also found that the bond strength is enhanced when the nanoport adhesive rings are stored in a refrigerated environment before use. The manufacturer recommends that the nanoports should be stored in a refrigerated space at 1 °C (34 °F). Also, the nanoport adhesive rings have an expiration date. Failure to follow these recommendations results in very poor bond quality. After several attempts to bond nanoports to copper plates, it was found that doubling the nanoports adhesive rings produces a more robust bond. Drilling of the ports in the copper

plates was performed using a conventional drill press and standard drill bits with an oil lubricant.

4.3 Cutting Plotter

The cutting process of the double-sided adhesive Kapton® tape is executed using a computer-controlled cutting plotter. The program that controls the cutting plotter is *Adobe Illustrator*. After saving the design drawing, described in section 4.1 in *.dxf* format, the file is launched in *Adobe Illustrator*. The cutting plotter window is then launched and the settings for the cut are entered. Nguyen [21] has shown that the best settings to cut the Kapton® tape smoothly with minimal damage to the channels is to set the cutting force to 30% of maximum and the cutting speed to 1 cm/s. These settings depend on the sharpness and the quality of the cutting blade. Comprehensive details of cutting the Kapton® tape using the plotter are presented by Nguyen [21], Torgerson [22], and Kolekar [23]. The back of the Kapton® tape has a protective film that is removed after the cutting process. The tape is placed in the cutting plotter with the sticky part facing upward toward the blade and the protective film side facing downward. The tape is aligned with the bottom edge of the plotter before the cutting process starts. Finally, the rollers that control the linear motion of the blade are locked. The cut command is then executed to start cutting the channels in the tape. Once the cutting process is complete, the rollers are unlocked and the tape is removed to a clean table to remove the cut sections of the channels using fine tweezers. The tape removal process must be executed very carefully as the tape can be easily damaged. With the cut sections removed, the tape is now ready to be placed on the substrate.

4.4 Final Assembly and Clamping System

The final assembly of the device involves bonding the Kapton® tape to the two substrates and curing. The bottom surface of the substrate with the nanoports is bonded to the Kapton® tape by first aligning the drilled ports in the substrate with the manifolds in the tape. To ensure good adhesion, a roller is used to remove air bubbles between the tape and the substrate. Next, the exposed protective film on the tape is carefully removed so as to prevent tearing the microchannel features. The minimize damage; protective film removal should be parallel to the channels. Once the protective film is removed, the bottom substrate is joined with the top substrate. This procedure is identical for glass and copper plates. Finally, the device is cured in an oven at a temperature of 60 $^{\circ}$C for 30 to 60 minutes. Since the test article operates at relatively high pressures, a clamping system was designed and installed to provide additional mechanical force for sealing. For the glass device, the clamping system proposed by Nguyen [21] was used. For the copper device, a total of eight 3/8" holes along the outer edges of the device are drilled in both copper plates. These holes are used as the clamping system of the device using bolts. Figure 4.2 shows pictures of the major fabrication steps described previously. Figure 4.3 shows the picture of the final assembly of the microchannel heat exchanger made with copper substrates.

4.5 Test Loop, Test Procedures, and DAQ's System

The working fluid is distilled water. The system is designed as an open flow loop. The water is driven into the test section with a Parker piston-type accumulator (3.785 L, 101.6 mm bore). The accumulator is charged with nitrogen gas from a type K nitrogen

(a)

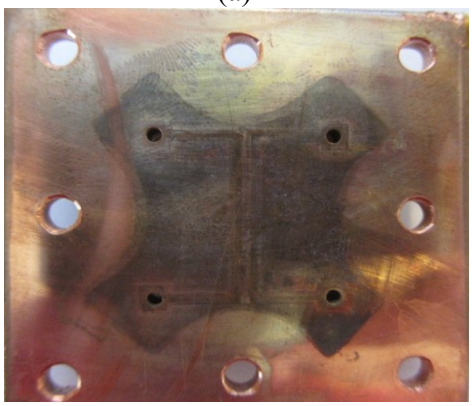

(b)

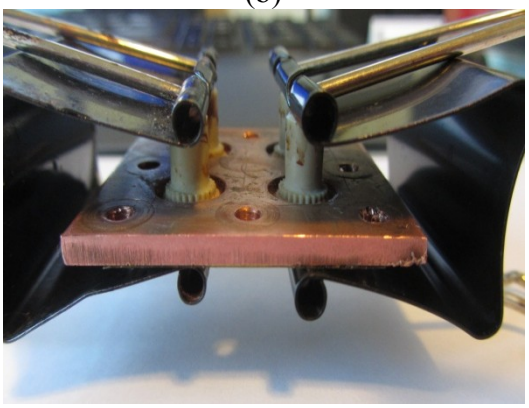

(c)

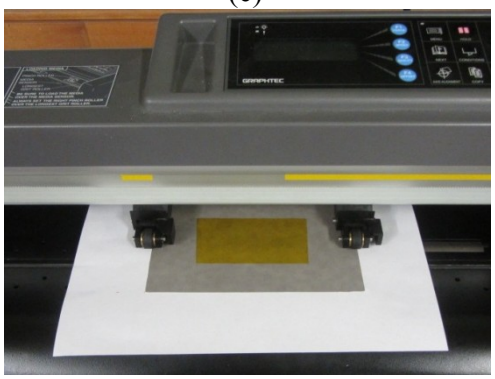

(d)

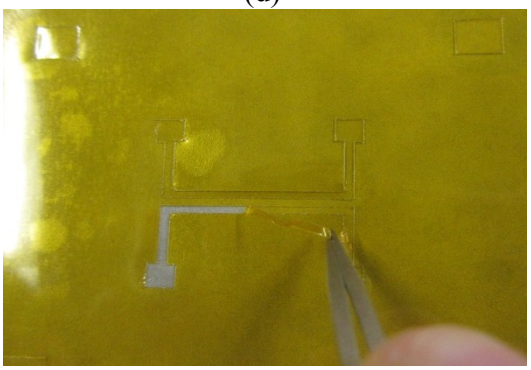

(e)

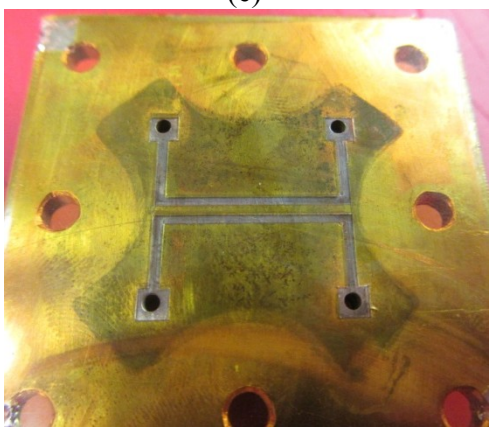

(f)

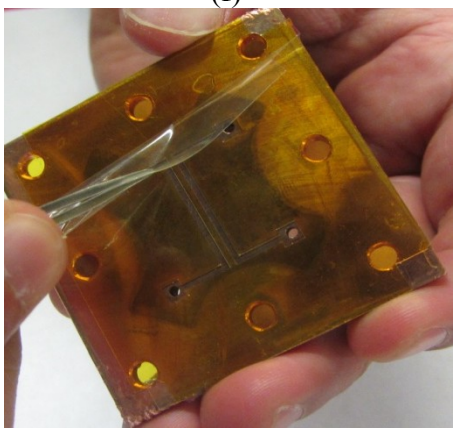

Figure 4.2 Fabrication steps (a) Inlet and outlet holes drilled (b) Nanoport aligned and cured (c) Kapton® tape cut using plotter (d) Removal of cut tape (e) Tape bonded to top substrate (f) Removal of protective film for final assembly to bottom substrate

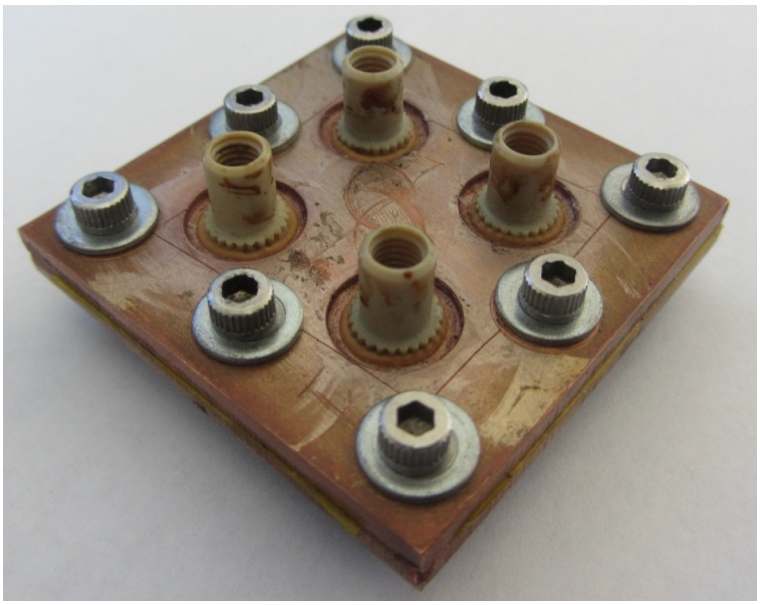

Figure 4.3 Microchannel heat exchanger assembly with the clamping system

tank to a maximum pressure of 13.8 MPa (2000 psi). The accumulator has a stainless steel piston to separate the gas side from the water side and to exert the force created by the pressurized gas. A Tecom pressure regulator located at the pressurized tank outlet is utilized to control the pressure and, hence, the fluid flow rate. The test loop setup is similar to the previous experiments conducted by Nguyen [21], Torgerson [22], and Kolekar [23] with slight modifications to accommodate the second fluid in the test section. The flow loop used by the previous researchers was designed for single channel devices while the current study includes two channels in the test section. The second fluid is accommodated by connecting parallel tubing, carrying the hot fluid, after the filter in the original flow loop. The new tubing passes through a heat exchanger before entering the hot channel side of the test section. The additional tubing and external heat exchanger are the only modifications made to the system previously used for single fluid

experiments; otherwise, the experiment was conducted in the same manner with the same instruments and data acquisition system.

Distilled water is initially drawn into the accumulator using a Gast vacuum pump. Two Swagelok T-valves located on both sides of the accumulator control the accumulator fill and discharge processes. The three-way valve on the gas side of the accumulator is opened toward the vacuum pump and the three-way valve on the water-side of the accumulator is opened toward the water supply. Once the vacuum pump is started, the piston inside the accumulator is pulled to the end of the gas side causing the water in the supply tank to be drawn into the water side of the accumulator. Once the accumulator is filled, both three-way valves are closed. The accumulator is connected to the water supply tank with stainless steel tubing (6.35 mm outer diameter). The three-way valve in the gas side of the accumulator is then opened toward the nitrogen gas tank line allowing the pressurized gas to flow into the accumulator, producing a total net force on the piston to drive the water flow to the test section. A 7 μm filter located at the water side exit of the accumulator removes impurities from the water. The test section is placed between four four-way unions connected to the nanoports on the test section using P-627 adapters and PEEK tubing (1.588 mm OD). The connections between the nitrogen tank, accumulator, filter and four-way unions are made with PEEK and stainless steel tubing (3.173 mm OD). Pressure sensors are connected to the four-ways unions to measure the inlet and outlet pressures. It is assumed that the measured pressures are equal to the pressures in the inlet and outlet manifolds. Static pressure measurements are taken with Setra 522 series sensors having an uncertainty of $\pm$ 0.15% of full scale. The high pressure sensors used for the inlet flows reads a maximum value of 3.45 MPa (500 psi) while the

outlet flows were measured using pressure sensors with maximum reading of 2.09 MPa (300 psi). The pressure sensors are powered with a Kenwood PR36 power supply. The fourth fitting in the four-way union is plugged. Temperatures are measured using T-type shielded thermocouples with an uncertainty of $\pm$ 1 °C. The thermocouples are located in close proximity to the inlet and outlet ports using a T-union made from PEEK (P-728) and male/male PEEK coupler (U-288). It was found that placing the thermocouples close to the test article reduced measurement error caused by heat transfer from connecting tubes to the surroundings.

Two Swagelok needle valves, located downstream of the test section, control the flow rates of the cold and hot fluids. It was found that the cold flow rate was always lower than the hot flow rate. For this reason, the cold flow is controlled to obtain different capacity rate ratios while the hot side needle valve was fully open. Hence, results presented for the current study are for the above-mentioned conditions. Better control could have been achieved by adding a second accumulator and control valve for the hot fluid. Unfortunately, this option was not available. Two plastic beakers placed on two Scientific SL600 mass balances are used to collect the fluids leaving the test section. Mass flow rates are determined using these mass measurements from the balances and elapsed time between measurements provided by an internal clock within LabView. The uncertainties in mass balances and internal clock are $\pm$0.01 g and $\pm$0.01 s, respectively. The maximum mass balance reading is 600 g. Mass accumulation is terminated when the reading approached the maximum value.

The hot water entering the test section is heated by a tube-in-tube heat exchanger from Exergy LLC connected to a programmable electric water circulator. The circulator

has the ability to heat and cool a fluid to specified temperatures based on the fluid type. For the current study, the water temperature in the circulator was set to 90 °C as this was the upper temperature limit recommended for use with water. The water level in the water heater is checked before starting each experiment

A National instruments PX-1010 data acquisition system is used to collect and record all data measured from thermocouples, pressure sensors and mass balances. Since this experiment is designed to gain understanding of the thermal behavior of the heat exchanger, a steady state condition must be reached before data are collected. This condition is satisfied when the temperatures of the two fluids are almost constant, i.e., when the temperature fluctuations are within $\pm$ 0.1 °C. Once this condition is met and the Reynolds numbers for both channels are relatively constant, the measured data are collected and saved in a *.txt* file using the Labview program constructed for this purpose. Table 4.2 presents the variables measured for each test condition. Mass flow rates are increased by increasing the accumulator pressure from the Nitrogen tank. The pressure is raised in 34.5 kPa (5 psi) increments, starting from as low as 34.5 kPa (5 psi), up to the maximum pressure limited by test section damage or leakage. The data collected using the Labview program are taken in intervals of about 150 ms. This data collection frequency created large data sets that can be time averaged to calculate the desired results. The desired relative uncertainties in both mass flow rates, which depend on the amount of mass accumulated during a specified time interval, are chosen to be < 0.1%. For this reason, the lower flow rates require a prolonged time interval when collecting the mass data.

Table 4.2 Summary of measured variables

Definition	Variable	Units	Medium of Measurement
Cold Inlet Temperature	$T_{c,i}$	°C	LabView
Cold Outlet Temperature	$T_{c,o}$	°C	LabView
Hot Inlet Temperature	$T_{h,i}$	°C	LabView
Hot Outlet Temperature	$T_{h,o}$	°C	LabView
Cold Inlet Pressure	$P_{c,i}$	psi	LabView
Cold Outlet Pressure	$P_{c,o}$	psi	LabView
Hot Inlet Pressure	$P_{h,i}$	psi	LabView
Hot Outlet Pressure	$P_{h,o}$	psi	LabView
Cold Mass	m_c	g	LabView
Hot Mass	m_h	g	LabView
Time	t	s	LabView

A flow loop schematic is presented in Figure 4.4. A picture of the entire experimental setup is shown in Figure 4.5. Table 4.3 presents an equipment list including type of instrument, manufacturer, model number and measurement uncertainty.

4.6 Data Reduction Program and Uncertainty Analysis

4.6.1 Data Reduction

The data extracted from the experiment are used to determine the final desired outputs such as heat rate, Reynolds number, and overall heat transfer coefficients using a Matlab code designed for this stage. The data are selected by determining the required time interval between mass measurements such that the relative uncertainty in the mass flow rate is less than 0.1%. Pressure and temperature measurements are averaged for the selected time interval. The working fluid (distilled water) properties are determined from

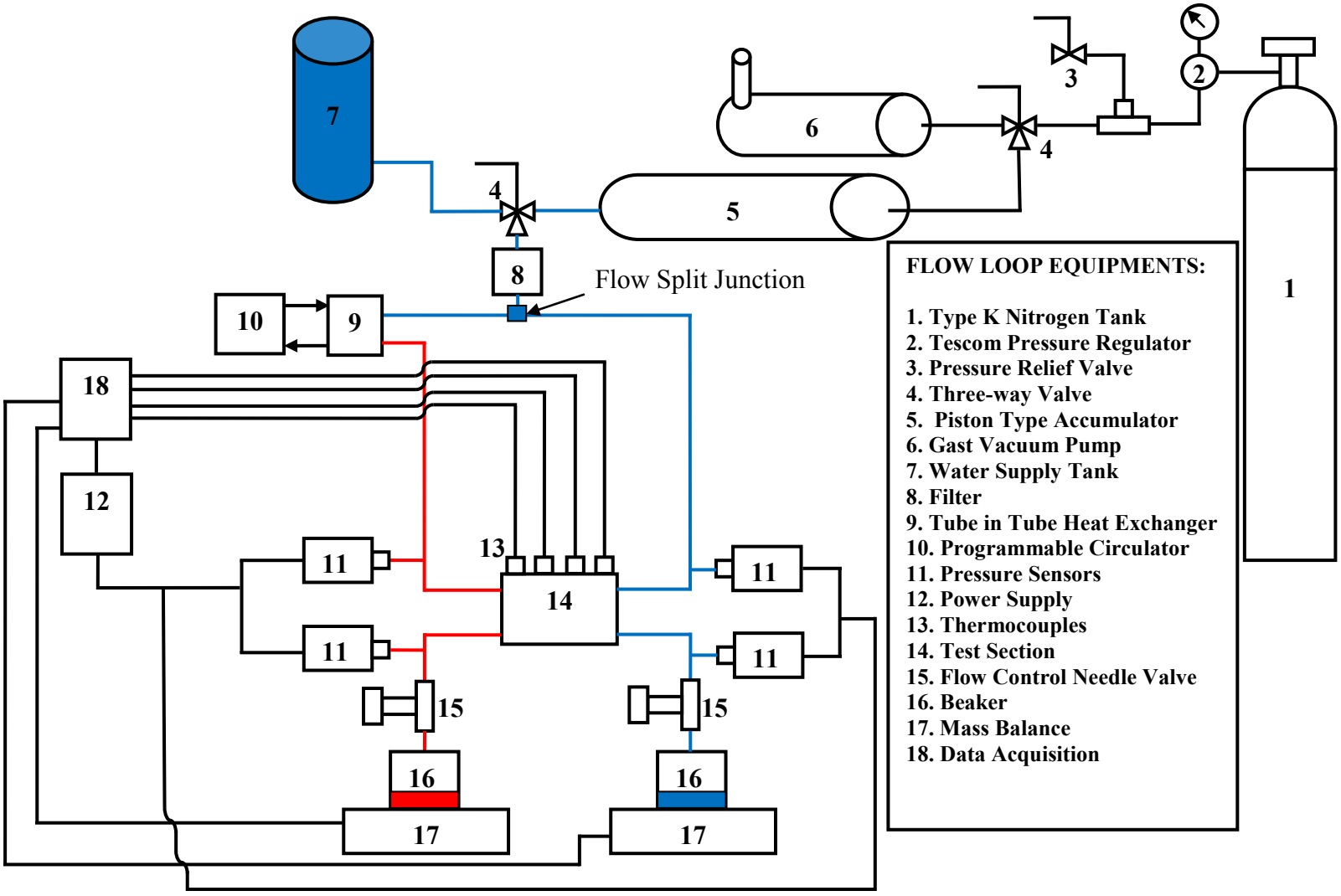

Figure 4.4 Flow loop schematic

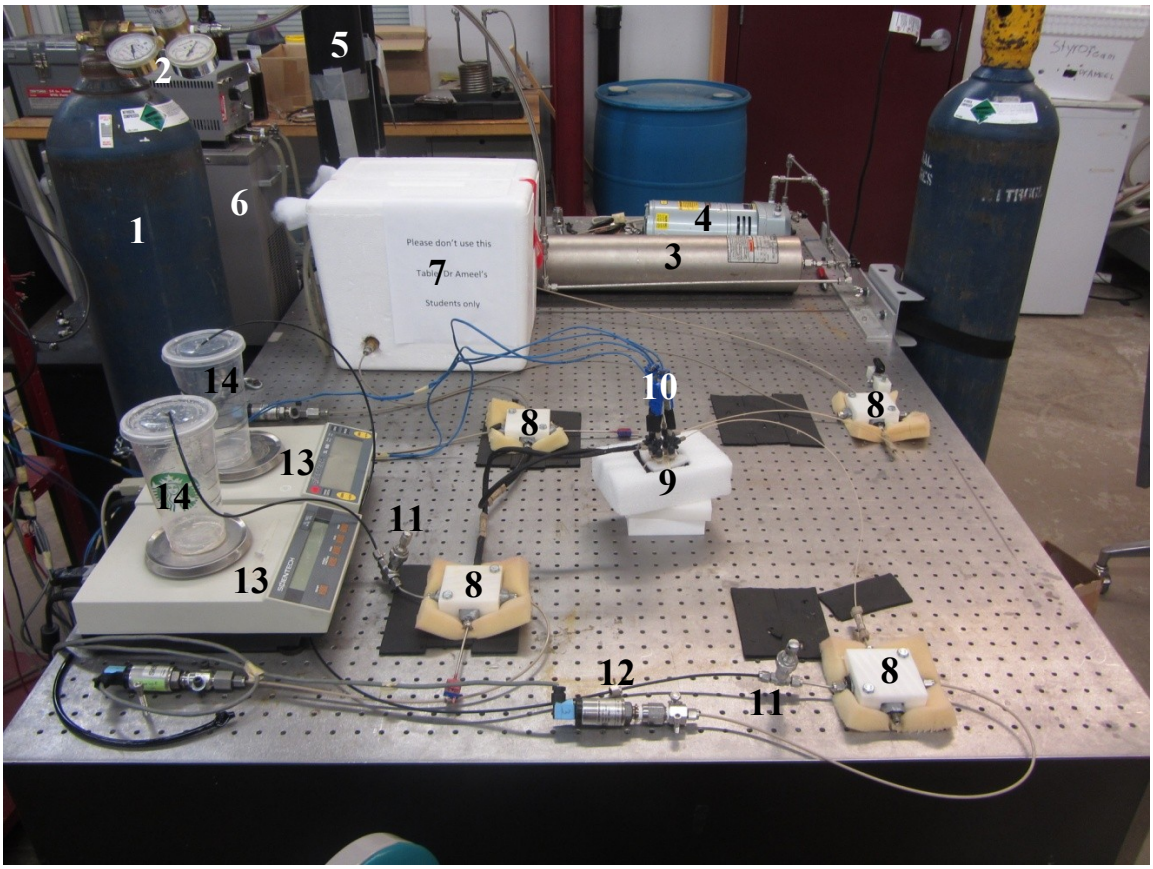

Figure 4.5 Experimental setup: (1) Nitrogen tank, (2) Pressure regulator, (3) Accumulator, (4) Vacuum pump (5) Water tank (6) Programmable recirculator, (7) Insulated tube-in-tube heat exchanger, (8) Four-way union, (9) Test section, (10) Thermocouples (11) Needle valve, (12) Pressure sensor, (13) Mass balance (14) Beaker

Table 4.3 Equipment list

Equipment/Instrument	Manufacturer	Qty	Part/Model Number	Manufacturer Uncertainty
Vacuum Pump	Gast	1	0523-101Q-G5820X	
Accumulator	Parker	1	A4N0231D612H	
Pressure Regulator	Tescom	1	44-1114-24	
Mass Balance	Scientech	2	SL600	± 0.01 g
Power Supply	Kenwood	1	PR36-1.2A	
Thermocouple	Omega	4	TMQSS-062U-2	± 1 °C
Pressure Sensor	Setra	4	522	0.15% of full scale psi
T-Valve	Swagelock	2	SS-43XS4	
Flow Control Valve	Swagelock	2	SS-2MG	
Filter	Swagelock	1	SS-4TF-7	
Pressure Release Valve	Swagelock	1	SS-41TS2	
Four-Way Union	Swagelock	4	SS-4-CS	
Union Fitting	Swagelock	12	SS-200-1-4	
Thermocouple Fitting	Upchurch Scientific	4	P-728	
	Upchurch Scientific	4	U-288	
Pressure Sensor Fitting	Swagelock	4	SS-200-7-4	
Elbow	Swagelock	2	SS-200-9	
	Swagelock	4	SS-400-9	
Nanoport to Flow Loop	Upchurch Scientific	4	F-247	
Fittings	Upchurch Scientific	6	F-300-01	
	Upchurch Scientific	6	F-142N	
	Upchurch Scientific	6	P-627 Adapter	
	Upchurch Scientific	6	P-350	
	Upchurch Scientific	6	LT-210	
PEEK Tubing	Upchurch Scientific	4 m	PK 2062	

Table 4.3 continued

Equipment/Instrument	Manufacturer	Qty	Part/Model Number	Manufacturer Uncertainty
Swagelock Tubing	Swagelock	0.6m	Stainless 6.35 mm	
	Swagelock	0.45m	Stainless 3.18 mm	
Tube in tube heat exchanger	Exergy LLC	1	00413	
Programmable recirculator	PolyScience	1	1167	
Lab View Internal Clock	National Instruments			± 0.01s

Matlab functions provided from [24]. These functions utilize the time-averaged temperatures and pressures of each fluid to determine the water density, dynamic viscosity, thermal conductivity, and specific heat capacity. The input arguments for these Matlab functions are the absolute temperature in Kelvin and absolute pressure in MPa.

The Reynolds number is defined as the ratio of inertial to viscous forces. The Reynolds numbers for both flows were observed to be different even for equivalent mass flow rates since the dynamic viscosity for the hot and cold fluids are highly temperature dependent. Once the measured experimental data, listed in Table 4.2, are obtained and processed using the procedure described in section 4.5 using Matlab, the final experimental outputs are calculated. Table 4.4 presents the equations used to determine the final experimental results. The heat rates and Reynolds numbers are calculated using the equations from Table 3.3. Also, the channel geometric parameters are calculated using the equations from Table 3.3. To assess the cost, in terms of the energy required to

Table 4.4 Equations used to determine the final experimental results

Equation	Unit	Equation no.
$\bar{q} = \frac{q_c + q_h}{2}$	W	(4.1)
$\varepsilon_{ex} = \frac{\bar{q}}{q_{max}}$		(4.2)
$\Delta T_1 = T_{h,i} - T_{c,o}$	°C	(4.3)
$\Delta T_2 = T_{h,o} - T_{c,i}$	°C	(4.4)
$\Delta T_{lm} = \frac{\Delta T_2 - \Delta T_1}{\ln\left(\frac{\Delta T_2}{\Delta T_1}\right)}$	°C	(4.5)
$U_{ex} = \frac{\bar{q}}{\Delta T_{lm} A_{c,ht}}$	kW/m^2/K	(4.6)
$NTU_{ex} = \frac{U_{ex} A_{c,ht}}{C_{min}}$		(4.7)
$Vol_{fluid} = A_i L_i$	m^3	(4.8)
$U_{ex,vol} = \frac{\bar{q}}{\Delta T_{lm} Vol_{fluid}}$	MW/m^3/K	(4.9)
$NTU_{th,2} = \frac{1}{C_r - 1} \ln\left(\frac{\varepsilon - 1}{\varepsilon C_r - 1}\right) \quad for\ C_r < 1$ $NTU_{th,2} = \frac{\varepsilon}{1 - \varepsilon} \quad for\ C_r = 1$		(4.10)

offset the frictional pressure losses, for the desired thermal performance the exergy efficiency for the system is determined. Two different exergy efficiency definitions are proposed. The first definition is the ratio of exergy change for the cold channel to the exergy change in the hot channel (Eq. 4.15). Eq. (4.11) to (4.14) in Table 4.5 present the exergy values for at the two inlet and two outlet flow streams. The second exergy efficiency definition (Eq. 4.16) is the ratio of the inlet exergies for both fluids to the outlet exergies for both fluids. The reference values in the exergy efficiencies analyses are determined at standard temperature and pressure (T = 25 °C, P = 101.325 kPa). The enthalpy and entropy terms in this analysis were determined using the average temperatures and pressures for the inlet and outlet fluids using the previously described built-in functions in Matlab provided from [24].

Table 4.5 Exergy calculation equations

Equation	Units	Equation no.
$\chi_{c,i} = \dot{m}_c\left[\left(h_{c,i} - h_{ref}\right) - T_{ref}\left(S_{c,i} - S_{ref}\right)\right]$	W	(4.11)
$\chi_{c,o} = \dot{m}_c\left[\left(h_{c,o} - h_{ref}\right) - T_{ref}\left(S_{c,o} - S_{ref}\right)\right]$	W	(4.12)
$\chi_{h,i} = \dot{m}_h\left[\left(h_{h,i} - h_{ref}\right) - T_{ref}\left(S_{h,i} - S_{ref}\right)\right]$	W	(4.13)
$\chi_{h,o} = \dot{m}_h\left[\left(h_{h,o} - h_{ref}\right) - T_{ref}\left(S_{h,o} - S_{ref}\right)\right]$	W	(4.14)
$\eta_{ch} = \dfrac{\chi_{c,o} - \chi_{c,i}}{\chi_{h,i} - \chi_{h,o}}$		(4.15)
$\eta_{oi} = \dfrac{\chi_{c,o} + \chi_{h,o}}{\chi_{c,i} + \chi_{h,i}}$		(4.16)

4.6.2 Uncertainty Analysis

The experimental uncertainties associated with the calculated results are determined by the method attributed to Moffat [25] as previously presented in Chapter 3. The measurement uncertainties for each instrument are taken to be that given by the manufacturer. As mentioned previously, the mass flow rate relative uncertainty is desired to be less than 0.1% since it has the greatest effect on the majority of the desired outputs. The propagation of the uncertainty of the mass measured by the scales affects the relative uncertainties in most of the outputs; hence, lower mass relative uncertainties result in lower relative uncertainty of the outputs. The perturbation chosen for the uncertainty analysis was set to 10^{-5} times the result R, as suggested by Moffat [25].

4.7 Microchannel Heat Exchanger Using Glass Substrates

4.7.1 Experimental Results

As concluded in Chapter 3 from the results of the EES code, the only feasible substrate material is one that has high thermal conductivity. Copper is chosen for the substrate material since it is easy to machine, can be easily bonded, and has the necessary high thermal conductivity. However, an initial attempt was made to create a heat exchanger with glass substrates. This trial was based on the invalid assumption that high thermal gradients would be sufficient to offset the low thermal conductivity. This attempt was also used to validate the EES code. The microchannel heat exchanger was constructed using two glass plates in the same pattern shown in Figure 4.1. The glass plate surface preparations, drilling process, Kapton® tape cutting, curing, and final

assembly were conducted as prescribed by Nguyen [21]. The glass heat exchanger was tested in the same manner explained in this chapter. The glass heat exchanger was entirely insulated from the surroundings using multiple layers of Styrofoam material. Results from the experiment for the glass heat exchanger indicated that very small temperature change occurred between the inlet and outlet for each fluid. This outcome indicates very poor thermal performance. The experimental results validated the EES model, which also predicted very poor performance with small temperature changes for the fluids. To ensure the validity of this conclusion, a 2D numerical model using Comsol™ Multiphysics software was created. The next section presents the details of the 2D numerical model.

4.7.2 Numerical Model Using Comsol Multiphysics

The numerical model is intended to confirm the experimental results of the glass microchannel heat exchanger. The software used for this purpose was Comsol™ Multiphysics, which has the capability of solving the governing equations for specific physics and boundary conditions. The actual device is modeled in two-dimensions. Figure 4.6 presents the in-plane view for the model. As a rough approximation to the heat transfer conditions in the two channels, the boundaries of the hot and cold channels are set to constant temperature boundary conditions of 60 °C and 20 °C, respectively. The boundary condition for the glass is set to be adiabatic. The glass and Kapton® tape properties are taken from the material library in Comsol Properties. The model mesh is chosen to be extremely fine, which is the maximum mesh resolution provided by Comsol. The model is solved for the steady state temperature field in the solid materials.

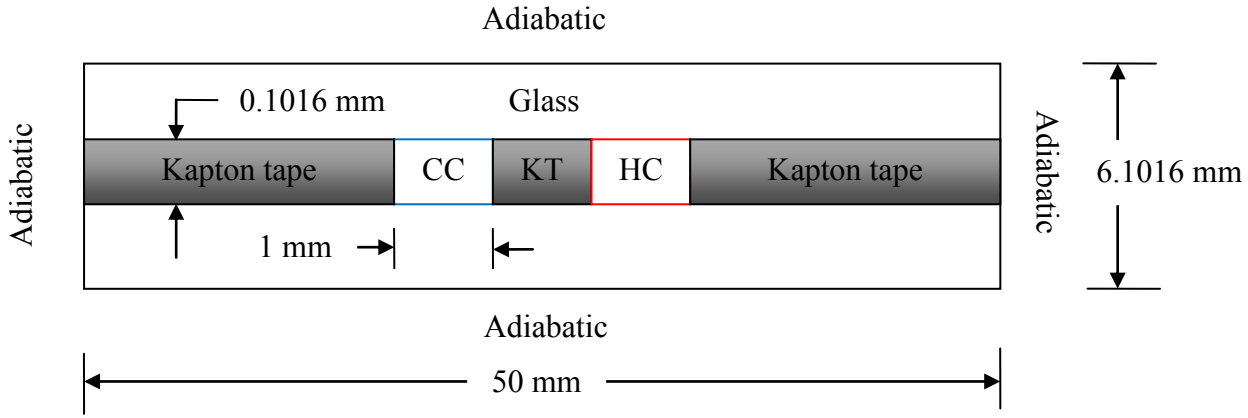

Figure 4.6 Numerical model geometry (not to scale). CC = cold channel and HC = hot channel. The width of the hot and cold channels and the wall thickness between the channels are all 1 mm.

An isothermal plot of the temperature field near the channels for the nominal conditions described above is shown in Figure 4.7. The isotherms indicate that heat is transferred between the fluids nearly equally through the substrate and glass materials. This visual assessment is confirmed by calculating the heat rate through each surface of the two microchannels. Results show that heat transfer between the two fluids through the Kapton® tape is quite low (q ~ 0.31 W) compared to the interfluid heat transfer through the glass substrates, which is approximately ~ 1.19 W (~ 80% of the total). The difference in heat rates is primarily due to the increased microchannel surface area in

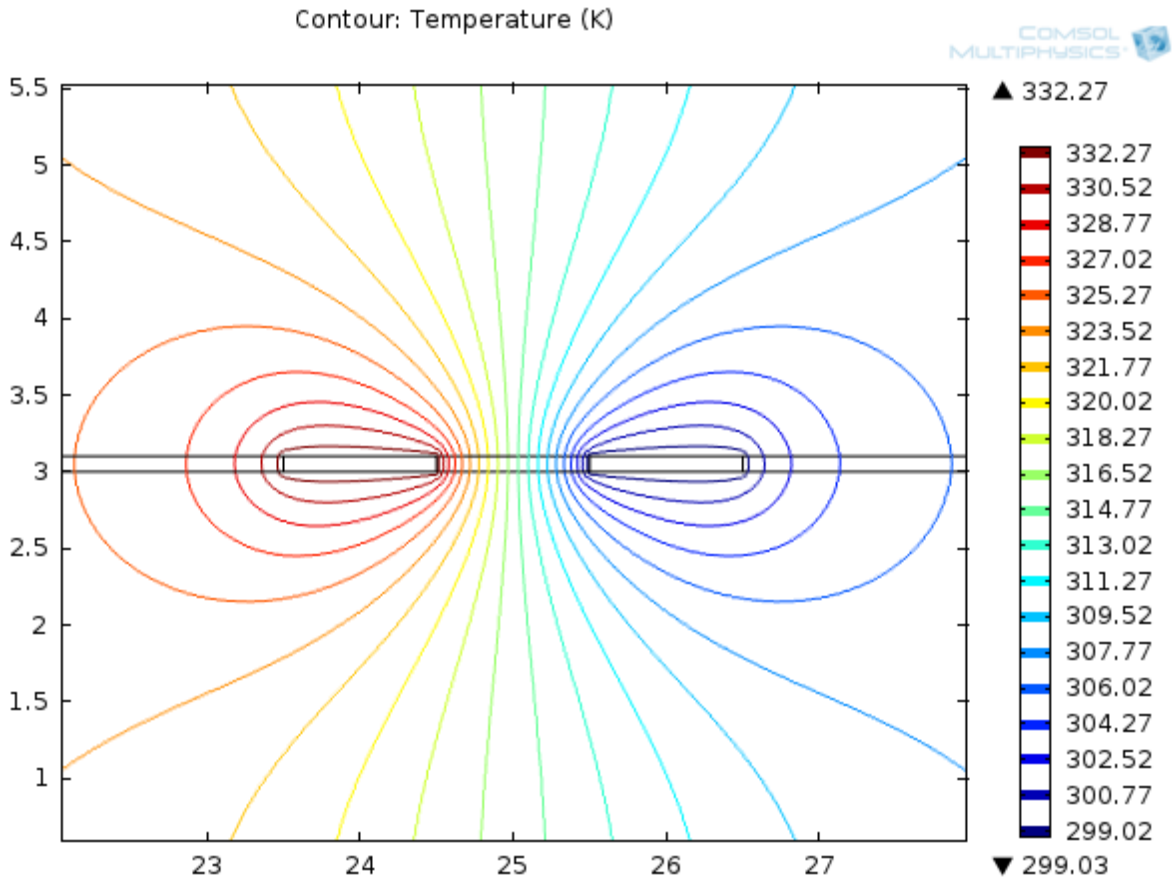

Figure 4.7 Temperature contours for the numerical analysis using nominal conditions

contact with the glass, since the two thermal conductivity values have the same order of magnitude. Note the low heat rates for both materials. An alternative solution for the copper substrates predicts much higher heat rates through the substrate (~ 350 W, 99.86 % of total) than the Kapton® tape (~ 0.46 W, 0.14 % of total). These heat rate data confirm the prediction from the EES model and they also help to explain the experimental results. The numerical model actually overestimates the heat rate, as the boundary conditions approximate a parallel flow configuration while the experiments are performed in a counterflow configuration where the outlet cold temperature is greater than that used in this analysis (20 °C). It is clear that from the numerical analysis that heat is primarily transferred through the substrates, regardless of the material, rather than the Kapton® tape. For this reason, the heat transfer surface area used in the data reduction has been modified to include only the top and bottom surface areas for each channel.

CHAPTER 5

RESULTS AND DISCUSSION

Four microchannel heat exchangers were fabricated, tested and analyzed. These systems have the same characteristic lengths, but differ in channel width. Table 5.1 shows details of the different systems. Data in the table represent nominal values. The uncertainties for these measurements are consistent with those determined by Nguyen [21]. As mentioned previously in Chapter 3, the heights of all channels are the same since height is equivalent to the tape thickness. The first and second systems were tested for three different capacity rate ratios (C_r~ 1, C_r ~ 0.75, and C_r ~ 0.5) while the third system was tested for two different capacity rate ratios (C_r ~ 1 and C_r ~ 0.75). Finally, the fourth system was tested for one capacity rate ratio (C_r ~ 1). The dimensions were previously measured by Nguyen [21] and for this reason, the current study assumed the data obtained by Nguyen [21] is still valid given the fact that the same manufacturing technique is applied and followed. Channel length and width were estimated by the design values in *AutoCAD* and the uncertainties obtained by Nguyen [21] were used in the final calculations. Kapton® tape by Nguyen [21] and those values were also used in this study. In the next few sections, the final results for the experiment are presented. First, the heat balance, heat rates, and heat fluxes for the different systems are presented

Table 5.1 Channel dimensions for the test articles

Variable \ System	System 1	System 2	System 3	System 4
W [mm]	1.00	0.75	0.50	0.35
L [mm]	32.0	32.0	32.0	32.0
H [mm]	0.1016	0.1016	0.1016	0.1016
α	0.1	0.13	0.2	0.29

as a function of Reynolds numbers. Then, the overall heat transfer coefficients are presented and discussed. Next, the $\varepsilon(NTU)$ plots for different capacity rate ratios and different systems are presented. Finally, exergy efficiency data are presented and discussed. It should be noted that the primary independent variables in the figures are Re_c and Re_h for each system. It was found that a significant difference between Re_c and Re_h for each system is always present. This is due to the difference in the cold and hot fluid mean temperatures, which directly affect the dynamic viscosity term in the Reynolds number definition (Eq. (3.13)), with the hot fluid having lower dynamic viscosity than the cold fluid. For this reason, all dependent variable data are presented as functions of Re_c and Re_h.

During the experiments, it was observed that the inlet hot fluid temperature increases with the hot fluid mass flow rate. This dependence is due to the nature of the process used to heat the hot fluid. Recall that the tube carrying the hot fluid after the control valve splits the flow from the accumulator. The hot fluid then transitions through a constant temperature water bath. The higher mass flow rate in the tube produces a

larger heat transfer coefficient, more heat transfer to the hot fluid, and, thus, higher temperature entering the test section. Figure 5.1 presents the inlet hot fluid temperature as a function of the hot fluid mass flow rate for all systems and capacity rate ratios.

5.1 Heat Balance, Heat Rate and Heat Flux Performance

5.1.1 Heat Balance

To verify that the conservation of energy principle is satisfied for the heat exchanger, a comparison between the hot and cold heat rates is made. Figure 5.2 presents the comparison of the heat rate from the hot fluid and the heat rate to the cold fluid for the different capacity rate ratios. A practical obstacle in miniaturized thermal devices is insulation quality. When downsizing a heat exchanger, thermal insulation thickness is typically decreased. In addition, the surface area to volume ratio is greater leading to an increased emphasis on convection heat loss while the heat transfer driving potential is unchanged. These conditions suggest heat losses to the ambient are difficult to prevent. On the other hand, typical heat exchanger models assume perfect insulation between the device and its surroundings. In the current study, the microchannel heat exchanger was insulated on all sides with multilayer Styrofoam material to minimize the heat transfer to the surroundings. As shown in Figure 5.2, the heat balance for all systems was very good. The heat balance for system 1 is excellent, as shown in Figure 5.2 (a). Based on the hot fluid heat rate, the maximum difference between the two heat rates is 16.6%. The heat balance for System 2, represented in Figure 5.2 (b), however, is the worst of the four heat exchangers. Based on the hot fluid heat rate, the maximum imbalance is 17.8%, which occurs for the lowest C_r. The cold flow rate was controlled to change the capacity rate

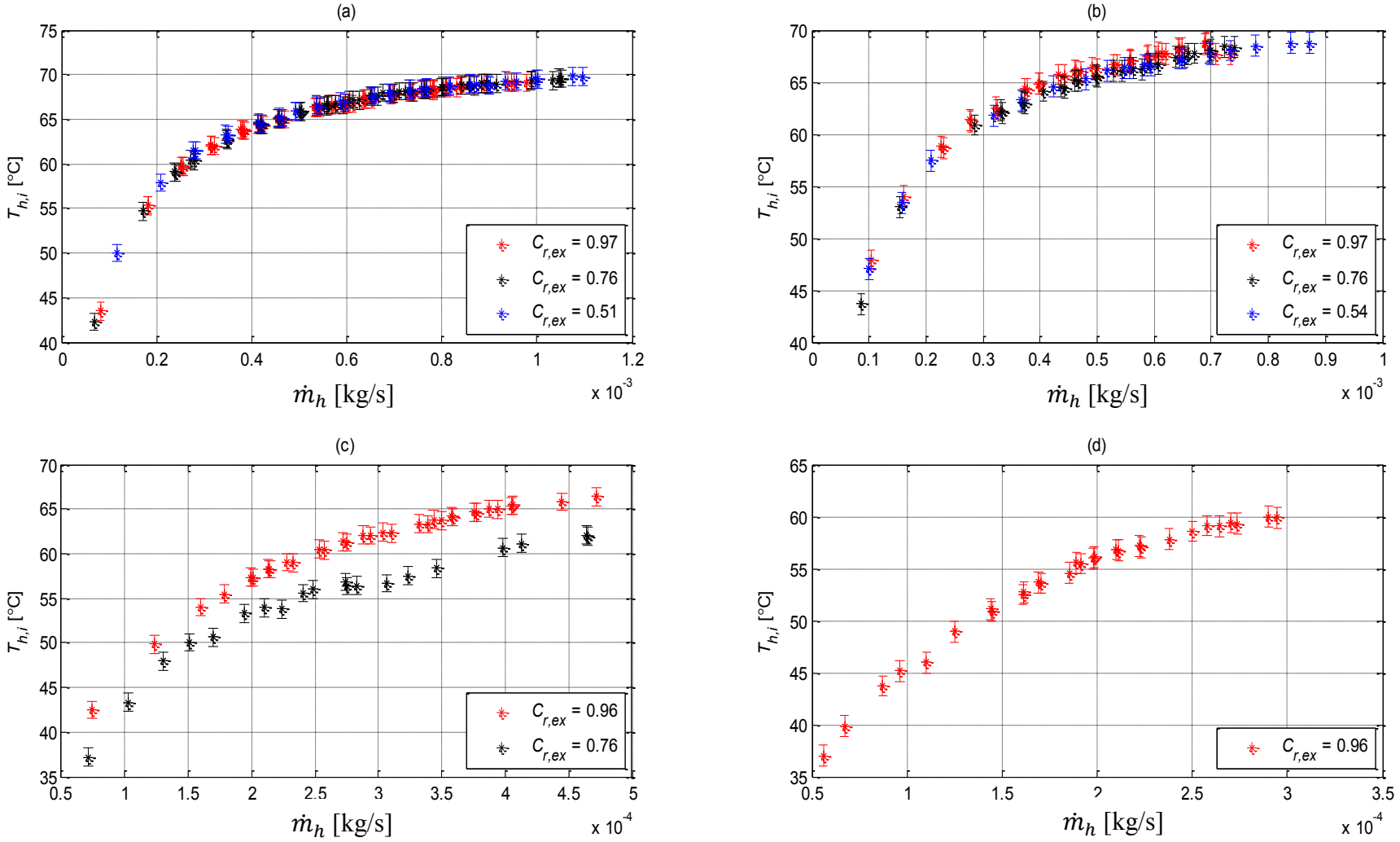

Figure 5.1 Inlet hot fluid temperatures as a function of hot fluid mass flow rate for different capacity rate ratios (a) Channel 1 (1000 μm), (b) Channel 2 (750 μm), (c) Channel 3 (500 μm), (d) Channel 4 (350 μm)

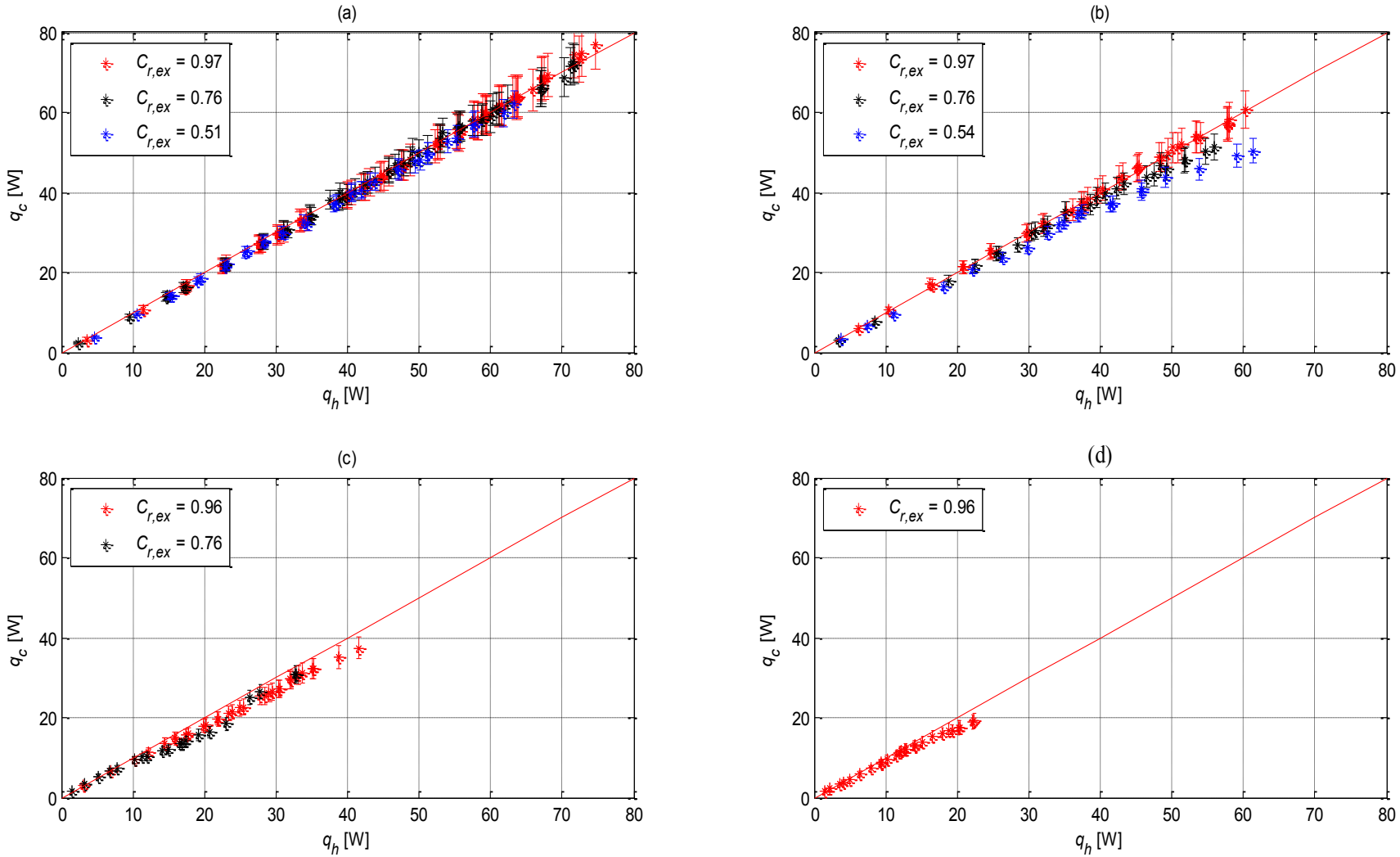

Figure 5.2 Heat balance results for different channel sizes: (a) Channel 1 (1000 µm), (b) Channel 2 (750 µm), (c) Channel 3 (500 µm), (d) Channel 4 (350 µm)

ratio. For a fixed total mass flow rate from the accumulator, a reduced cold fluid mass flow produces a greater hot fluid flow rate. As noted above, the increased hot fluid flow rate leads to an increased hot fluid inlet temperature. The higher hot fluid temperature most likely increases the heat loss to the surroundings from the device. Thus, the heat rate imbalance increases. Systems 3 and 4, which are shown in Figures 5.2 (c) and (d), respectively, have a similar heat rate imbalance for the same reason. Note that the capacity rate ratios are the mean values for each experiment.

5.1.2 Heat Rate

The experimental heat rates for the cold fluid are presented in Figure 5.3 as functions of the Reynolds number for the cold fluid Re_c. As expected, the heat transfer to the cold fluid increases with the cold fluid Reynolds number for all systems due to relationship between the Nusselt number and the Reynolds number. Figure 5.3 (a) presents these data for system 1 as a function of Re_c for the different capacity rate ratios. Heat rates increase with a decrease in capacity rate ratios for the same Re_c. This trend is explained by the conservation of energy principle. When the capacity of the cold flow decreases (due to decrease $\dot{m}_c$), $\dot{m}_h$ increases, $T_{h,i}$ increases (as previously discussed), and the interfluid heat transfer driving potential increases, and, thus, q_c increases. The same explanation is valid for system 2, as shown in Figure 5.3 (b). However, the effect of C_r is less dramatic. This difference is due to the heat rate imbalance in system 2 for smaller C_r, as shown in Figure 5.2 (b). Figure 5.3 (c) shows the heat rate data for system 3. The trend with C_r is the same as for systems 1 and 2; however, the heat rate imbalance in system 3 shown in Figure 5.2 (c) is the reason the effect is reduced. Also, since system

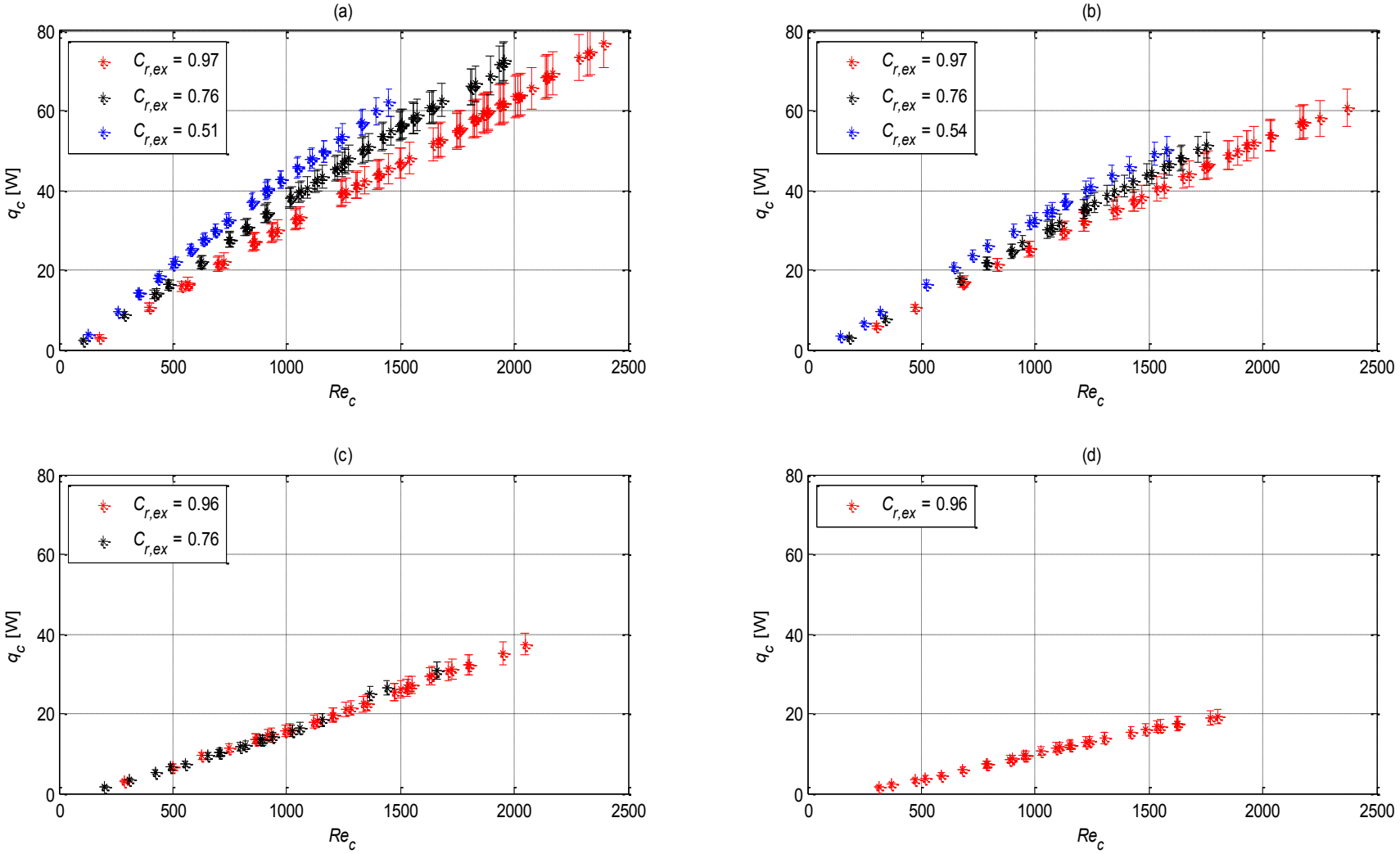

Figure 5.3 Effect of cold fluid Reynolds number on heat rate to the cold channel for different channel sizes: (a) Channel 1 (1000 µm), (b) Channel 2 (750 µm), (c) Channel 3 (500 µm), (d) Channel 4 (350 µm)

3 is smaller in size, the mass flow rate is smaller than in systems 1 and 2 (see Eq. 4.1) and the differences in heat rates for the two different capacity rate ratios are not as great as the previous systems. Figure 5.3 (d) presents the heat rate for system 4. Note that, as expected, q_c decreases as the system size decreases (system 1 → system 4) for the same Re_c. Also note that the heat rate is nearly linear with Re_c for all systems. This is due to the increase of the mass flow rate with Re in Eq. (3.27). Obtaining a lower C_r for smaller channels introduces higher risk of leakage since reducing one side of the flows will increase the other side inlet pressure and with the smaller channel sizes the risk of leakage is higher. Also, it was explained that with lower C_r, the heat imbalance increases which affects the desired output calculations. This observation has been confirmed experimentally with smaller channels as an attempt was conducted to obtain lower C_r and the heat imbalance was very obvious. On the other hand, the maximum Reynolds numbers for smaller channels are found to be lower than larger channels. It can be seen from Eqs. (3.11), (3.12) and (3.13) that Re can be rewritten as:

$$Re = \frac{2\dot{m}}{\mu(W+H)} \tag{5.1}$$

From Eq. (5.1) it is clear that the Reynolds number is linearly proportional with the mass flow rate which is decreasing with the channel size for the same inlet pressures. Also, Reynolds number is inversely proportional to the channel width and height and the fluid dynamic viscosity. Since the height of the channel is fixed, Reynolds number is not affected by this variable. However, as channel width decreases, the Reynolds number

increases based on the inverse relationship with channel width. The dynamic viscosity of the fluid is temperature dependant and is determined using the fluid mean temperature. Since the heat rate is decreasing with the channel size, as explained previously, so does the mean temperature of the fluid, which results in a relatively higher dynamic viscosity than that in larger channels. Even though the channel width is decreasing, which would increase Reynolds number, the decrease of mass flow rate and fluid dynamic viscosity is more dominant on Reynolds number and for this reason, Reynolds numbers in smaller channels are lower than larger channels. Figure 5.4 represents the hot channel heat rates for all systems as a function of the hot fluid Reynolds number. System 1 q_h data are shown in Figure 5.4 (a) for different capacity rate ratios. As opposed to the $q_c(C_r)$ relationship, q_h decreases with C_r for fixed Re_h. Again, the conservation of energy principle helps explain the trend. For fixed Re_h, $\dot{m}_h$ must also be fixed, meaning $\dot{m}_c$ and C_c must decrease for a decrease in C_r. With decreased capacity in the cold fluid, q_c and q_h will both decrease, assuming no heat loss to the surroundings. Figure 5.4 (b) shows the same $q_h(C_r)$ behavior for system 2 for the same reasons as for system 1. The system 3 response, shown in Figure 5.4 (c), exhibits the same behavior as for systems 1 and 2. In this case, the downward shift with C_r is more obvious than in Figure 5.3 (c), due to the good heat balance found in Figure 5.2 (c). Finally, Figure 5.4 (d) presents the heat rates for system 4. A final comparison for the heat rates with equivalent capacity rate ratios for different channel sizes is presented in Figure 5.5. A comparison of the cold fluid heat rates as a function of Re_c is shown in Figure 5.5 (a) for the largest capacity rate ratio (C_r ~ 1) for W = 1000, 750, 500, and 350 μm. As expected, heat rates increase with channel size for the same capacity rate ratio and Reynolds number. This is primarily due to the

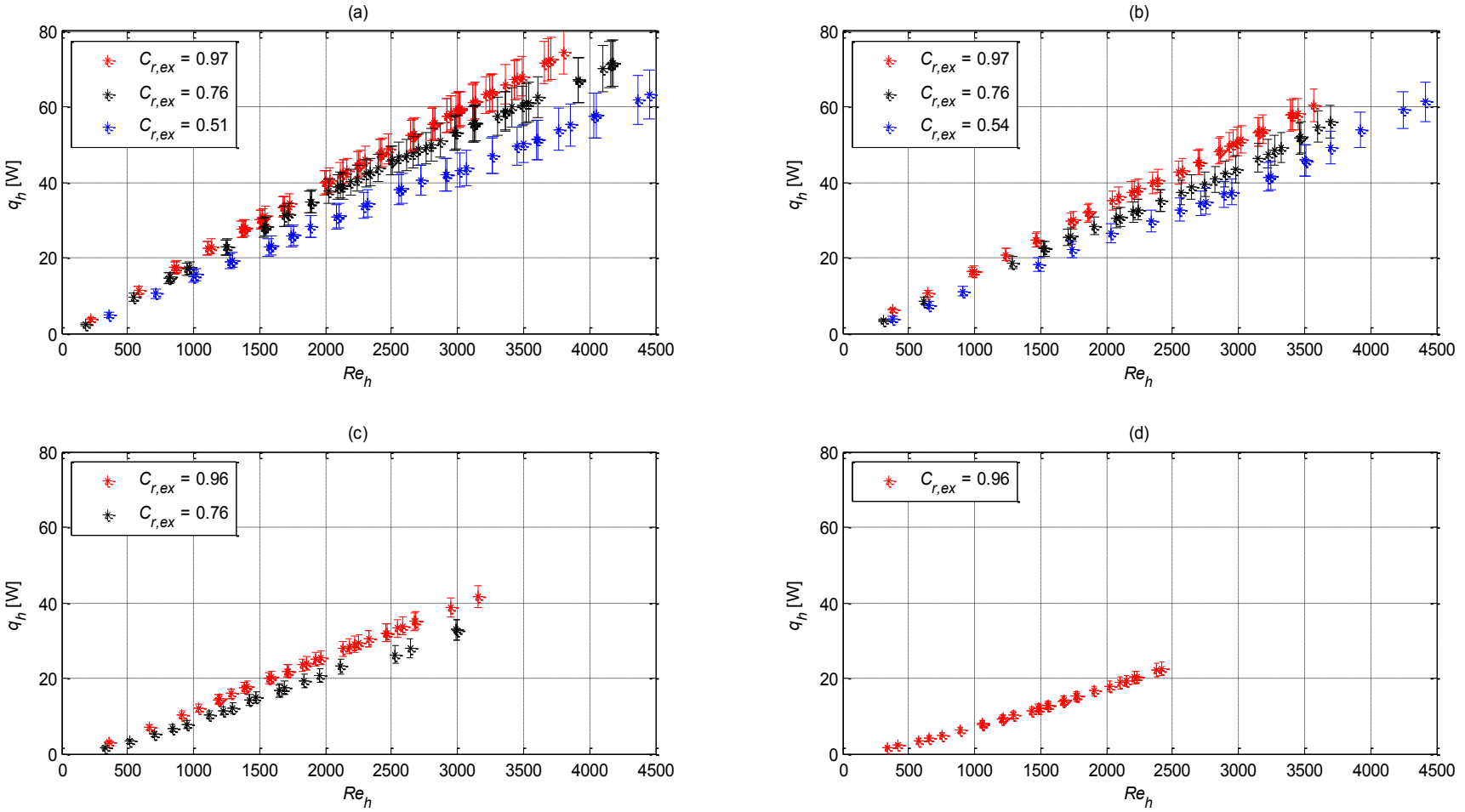

Figure 5.4 Effect of hot fluid Reynolds number on heat rate to the hot channel for different channel sizes: (a) Channel 1 (1000 µm), (b) Channel 2 (750 µm), (c) Channel 3 (500 µm), (d) Channel 4 (350 µm)

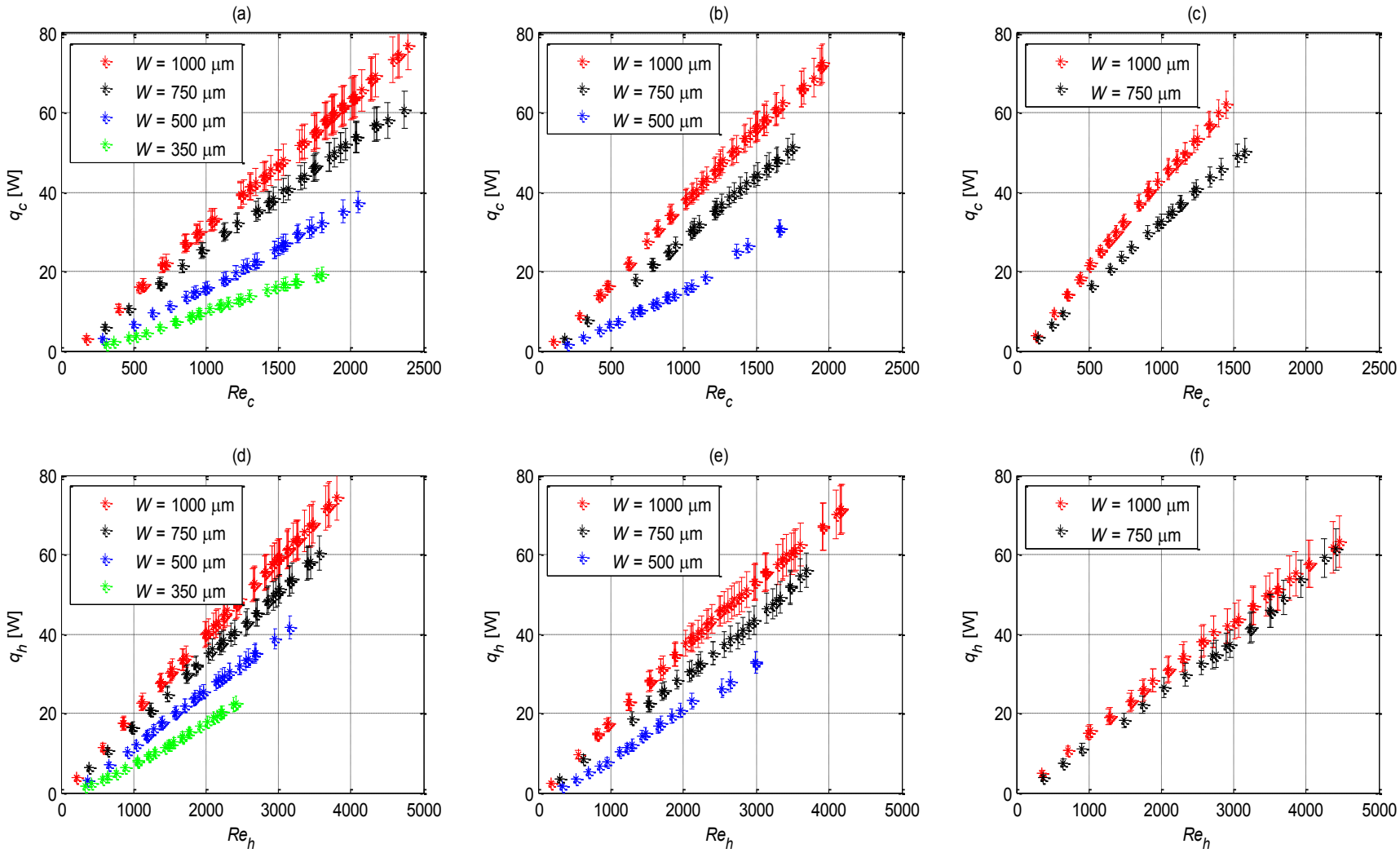

Figure 5.5 Effect of cold and hot fluid Reynolds numbers on heat rate to the cold and hot channels for different capacity rate ratios: (a) $C_r \sim 1$, (b) $C_r \sim 0.75$ (c) $C_r \sim 0.5$ (d) $C_r \sim 1$, (e) $C_r \sim 0.75$ (f) $C_r \sim 0.5$

larger heat transfer surface area associated with the larger channel width. Figure 5.5 (b) and (c) show similar trends for heat rates as a function of Re_c and W for capacity rate ratios C_r ~ 0.75 and C_r ~ 0.5, respectively. Figures 5.5 (d), (e), and (f) present q_h data as a function of W and Re_h for the three C_r. The trends observed for the cold fluids are also exhibited for the hot fluids; the explanations for the trends are the same. Table 5.2 presents the maximum and minimum experimental heat rates achieved for each system for different capacity rate ratio along with the associated maximum and minimum Reynolds number for the cold and hot fluids.

5.1.3 Heat Flux

Heat flux is the heat rate gained or lost by the cold or hot channels divided by the respective channel surface area. Since the two channels are identical, the surface areas are equal. Figure 5.6 presents the heat flux for the cold channel as a function of Re_c for all systems and for the different capacity rate ratios. Since the heat flux is the heat rate divided by the heat transfer surface area, the trends observed in the heat flux data are similar to those for the heat rate data. This similarity is obvious when Figure 5.3 and Figure 5.6 are compared. The explanations for the effects of Re_c and C_r on the heat flux are synonymous with those for the heat rate. Figure 5.7 presents the heat flux for the hot channel as a function of Re_h for all the heat exchangers and for the different capacity rate ratios. The same explanations for the observed trends for the hot fluid heat rate (Figure 5.4) are valid here. A final comparison of the heat fluxes with the same capacity rate ratios for the different systems is presented in Figure 5.8. A comparison of the heat flux for the cold channel as a function of Re_c is shown in Figure 5.8 (a) for the largest

Table 5.2 Maximum and minimum heat rates and associated maximum and minimum Reynolds numbers for the hot and cold fluids for all systems with different capacity rate ratios

System \ Variable		q_c [W]		q_h [W]		Re_c		Re_h	
		Min.	Max.	Min.	Max.	Min.	Max.	Min.	Max.
System 1	C_r = 0.97	3.2201	76.93	3.6367	74.591	175.42	2395.4	223.15	3803
	C_r = 0.76	2.2631	72.434	2.4339	71.613	107.05	1954.6	184.68	4177.7
	C_r = 0.51	3.9353	62.063	4.7182	63.26	130.66	1448.2	356.62	4451.2
System 2	C_r = 0.97	5.9212	60.796	6.1631	60.22	301.19	2369.1	379.73	3568.1
	C_r = 0.76	3.127	51.436	3.4267	55.99	181.32	1752.2	306.12	3692.7
	C_r = 0.54	3.2688	50.442	3.7361	61.365	146.39	1580.3	376.19	4413.8
System 3	C_r = 0.96	3.0026	37.469	3.0115	41.617	289.21	2046.5	361.16	3155.4
	C_r = 0.76	1.6173	30.748	1.567	32.827	201.3	1662.3	327.8	2994.6
System 4	C_r = 0.96	1.5317	19.378	1.5428	22.405	312.3	1803.6	335.93	2418.3

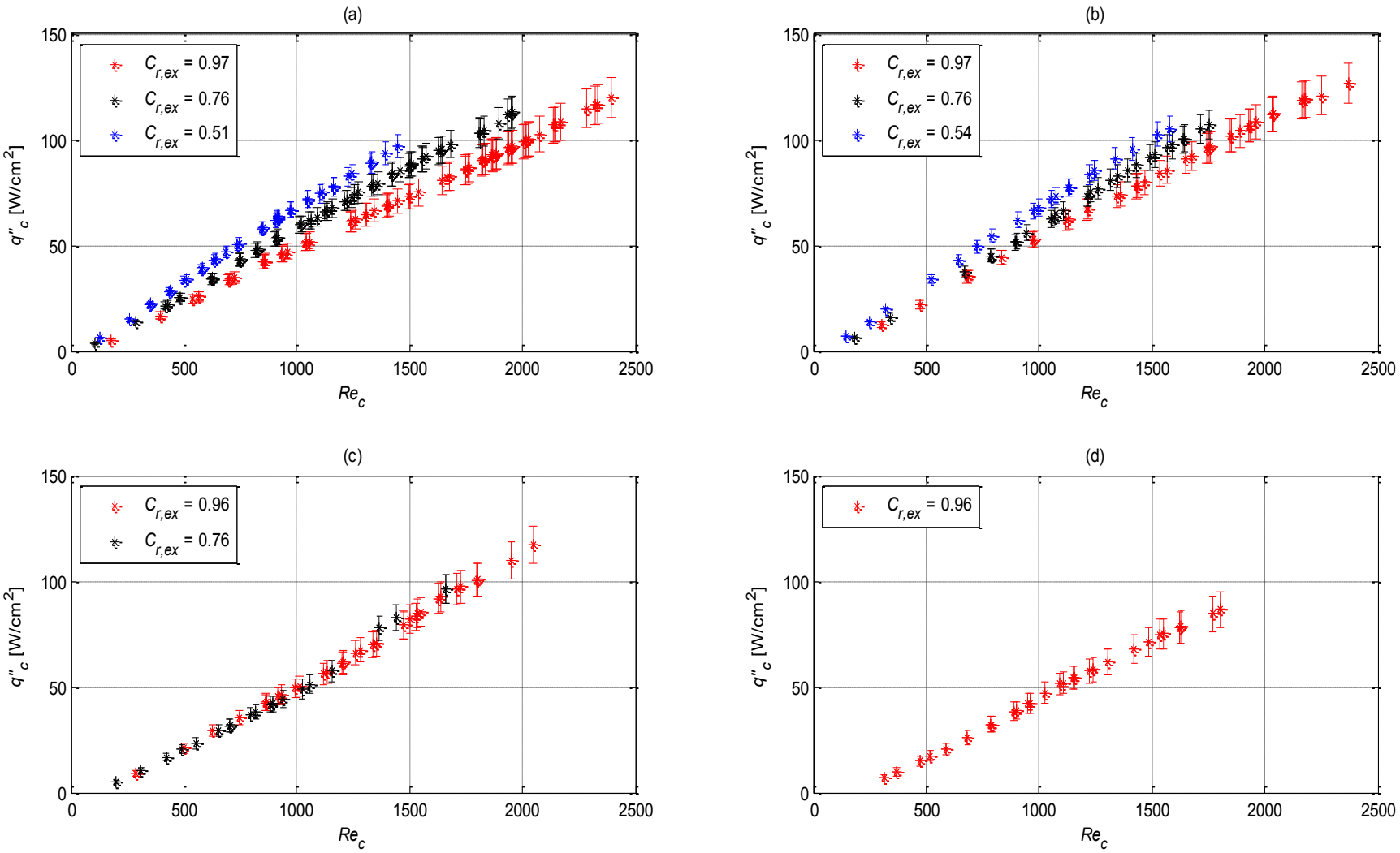

Figure 5.6 Effect of cold fluid Reynolds number on heat flux to the cold channel for different channel sizes: (a) Channel 1 (1000 µm), (b) Channel 2 (750 µm), (c) Channel 3 (500 µm), (d) Channel 4 (350 µm)

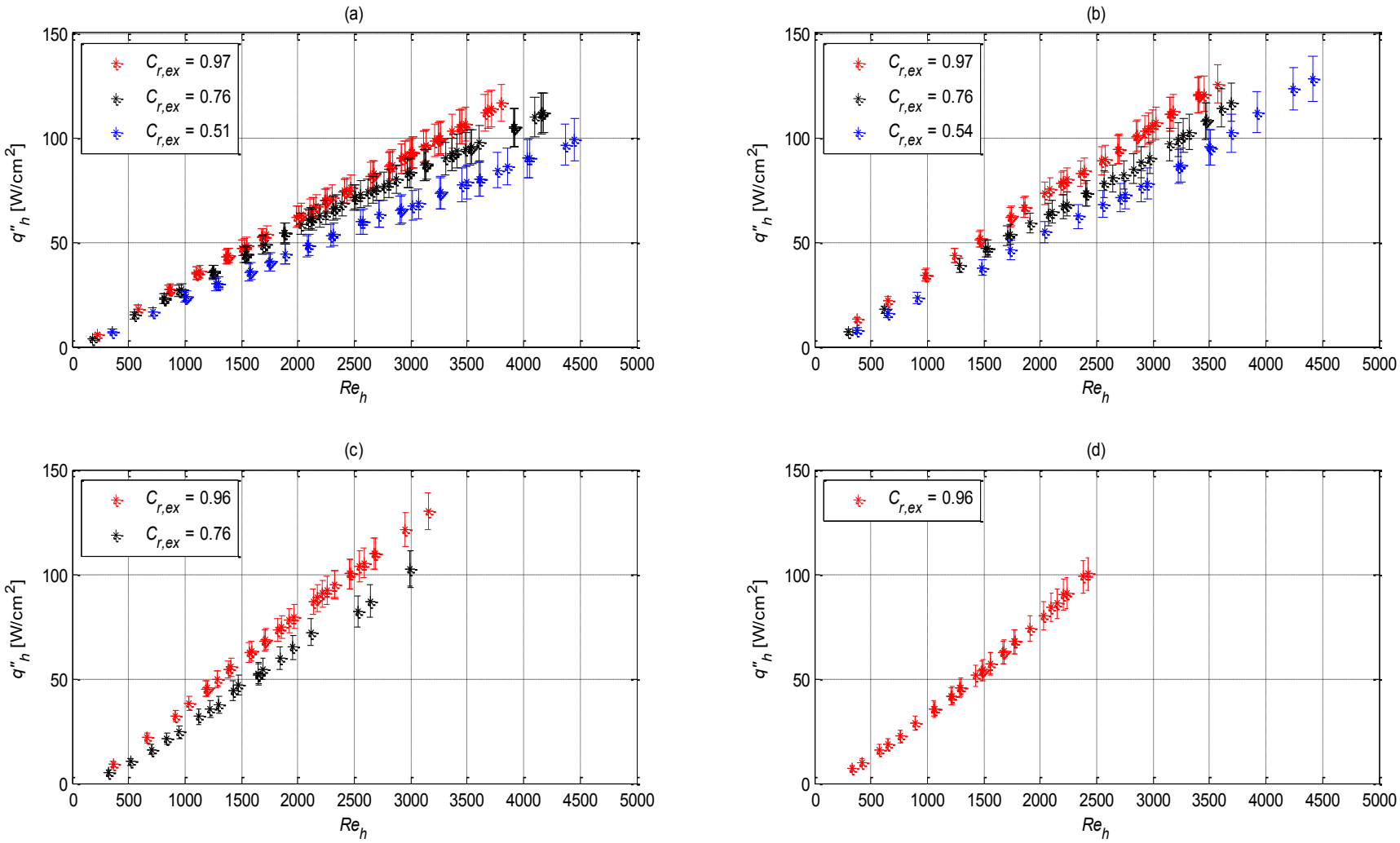

Figure 5.7 Effect of hot fluid Reynolds number on heat flux from the hot channel for different channel sizes: (a) Channel 1 (1000 µm), (b) Channel 2 (750 µm), (c) Channel 3 (500 µm), (d) Channel 4 (350 µm)

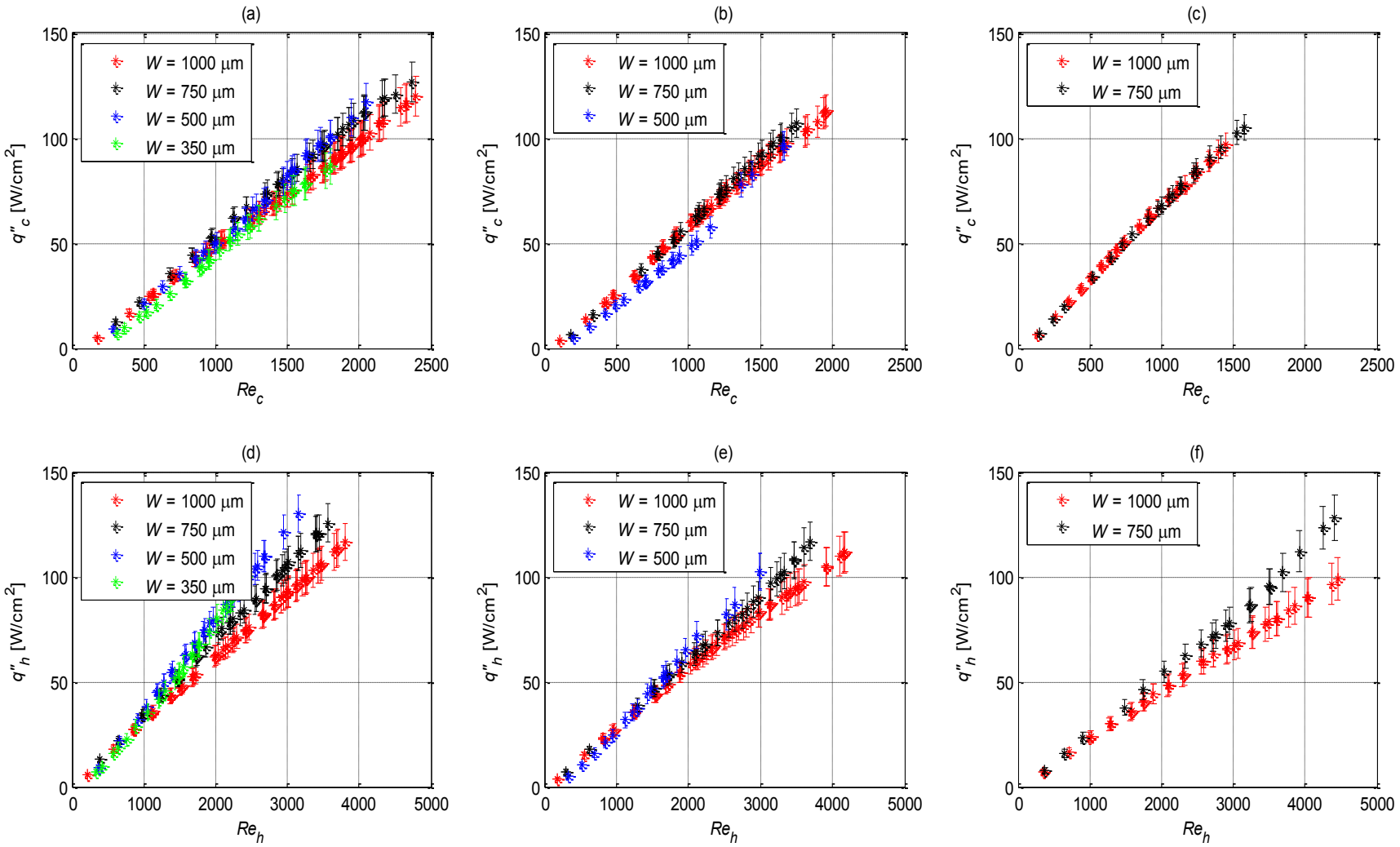

Figure 5.8 Effect of cold and hot fluid Reynolds numbers on heat fluxes to and from the cold and hot channels, respectively, for different capacity rate ratios: (a) $C_r \sim 1$, (b) $C_r \sim 0.75$ (c) $C_r \sim 0.5$ (d) $C_r \sim 1$, (e) $C_r \sim 0.75$ (f) $C_r \sim 0.5$

capacity rate ratio (C_r ~ 1) and all 4 heat exchangers. In contrast to the heat rate behavior shown in Figure 5.5 where heat rate trends shifted downward with decreasing channel size for the same capacity rate ratio, heat flux data increase slightly, or are nearly the same, for a decrease in channel size. These trends are a result of the decrease in heat transfer surface area that accompanies the smaller channel widths. For a decrease in channel size, the heat rate is reduced, but so is the heat transfer surface area. Thus, the effect of channel size on the heat flux is negligible, particularly for small Reynolds number, or is the inverse of that for the heat rate (i.e., heat flux increases with decreasing channel size). Figure 5.8 (b) and (c) present a comparison of the heat flux for the cold channels as a function of Re_c for capacity rate ratios of C_r ~ 0.75 and C_r ~ 0.5, respectively. Figure 5.8 (d), (e), and (f) present comparisons of heat flux for the hot channels as a function of Re_h for capacity rate ratios of C_r ~ 1, C_r ~ 0.75, and C_r ~ 0.5, respectively. Table 5.3 summarizes the maximum and minimum experimental heat fluxes achieved for each system for the different capacity rate ratios along with the associated maximum and minimum Reynolds number for the cold and hot fluids.

Table 5.3 Maximum and minimum heat fluxes for all heat exchangers with different capacity rate ratios along with the associated maximum and minimum Reynolds numbers for cold and hot fluids

System \ Variable		q_c'' [W/cm^2]		q_h'' [W/cm^2]		Re_c		Re_h	
		Min.	Max.	Min.	Max.	Min.	Max.	Min.	Max.
System 1	C_r = 0.97	5.0313	120.2	5.6823	116.55	175.42	2395.4	223.15	3803
	C_r = 0.76	3.536	113.18	3.8029	111.89	107.05	1954.6	184.68	4177.7
	C_r = 0.51	6.1489	96.974	7.3722	98.843	130.66	1448.2	356.62	4451.2
System 2	C_r = 0.97	12.336	126.66	12.84	125.46	301.19	2369.1	379.73	3568.1
	C_r = 0.76	6.5145	107.16	7.139	116.65	181.32	1752.2	306.12	3692.7
	C_r = 0.54	6.8101	105.09	7.7835	127.84	146.39	1580.3	376.19	4413.8
System 3	C_r = 0.96	9.3832	117.09	9.4109	130.05	289.21	2046.5	361.16	3155.4
	C_r = 0.76	5.0542	96.088	4.8967	102.58	201.3	1662.3	327.8	2994.6
System 4	C_r = 0.96	6.8378	86.509	6.8876	100.02	312.3	1803.6	335.93	2418.3

5.2 Overall Heat Transfer Coefficients

5.2.1 Experimental Overall Heat Transfer Coefficients

Heat exchanger performance can be evaluated by many parameters; one of these is the overall heat transfer coefficient. The larger this parameter, the more heat the device can transfer between the two fluids. The method used to calculate the experimental overall heat transfer coefficient was previously explained in section 4.6. Figure 5.9 presents the experimental overall heat transfer coefficients of all systems with different capacity rate ratios as a function of Re_c. For the largest channels represented in Figure 5.9 (a), the same trends observed for the heat rate and heat flux data are evident. Once again, the energy conservation principle, as presented in section 5.1.2 for the heat rate, can be used here to explain the trends. In this case, however, fluid temperature changes are also included through the log mean temperature difference and the heat transfer surface area is inversely proportional to U (see Eqs. 3.27 and 4.6). Thus, the effects of C_r and Re_c are complicated by the simultaneous changes that occur to A, ΔT_{lm}, and $\dot{m}_c$. One change from earlier trends is the effect of C_r on U_{ex} for system 3 shown in Figure 5.9 (c). The complex interaction of all the variables now results in U_{ex} increasing for a decrease in C_r at fixed Re_c, whereas C_r appears to have no effect on q_c for similar conditions (Figure 5.3 (c)). Figure 5.10 presents the experimental overall heat transfer coefficient of all systems with different capacity rate ratios as a function of Re_h. The explanation for the trends observed for q_h is also valid for U_{ex}. One change, however, is the apparent negligible effect that C_r has on U_{ex} for system 3 at fixed Re_h. This variable independence is in contrast to q_h decreasing with C_r for fixed Re_h (Figure 5.4 (c)). The

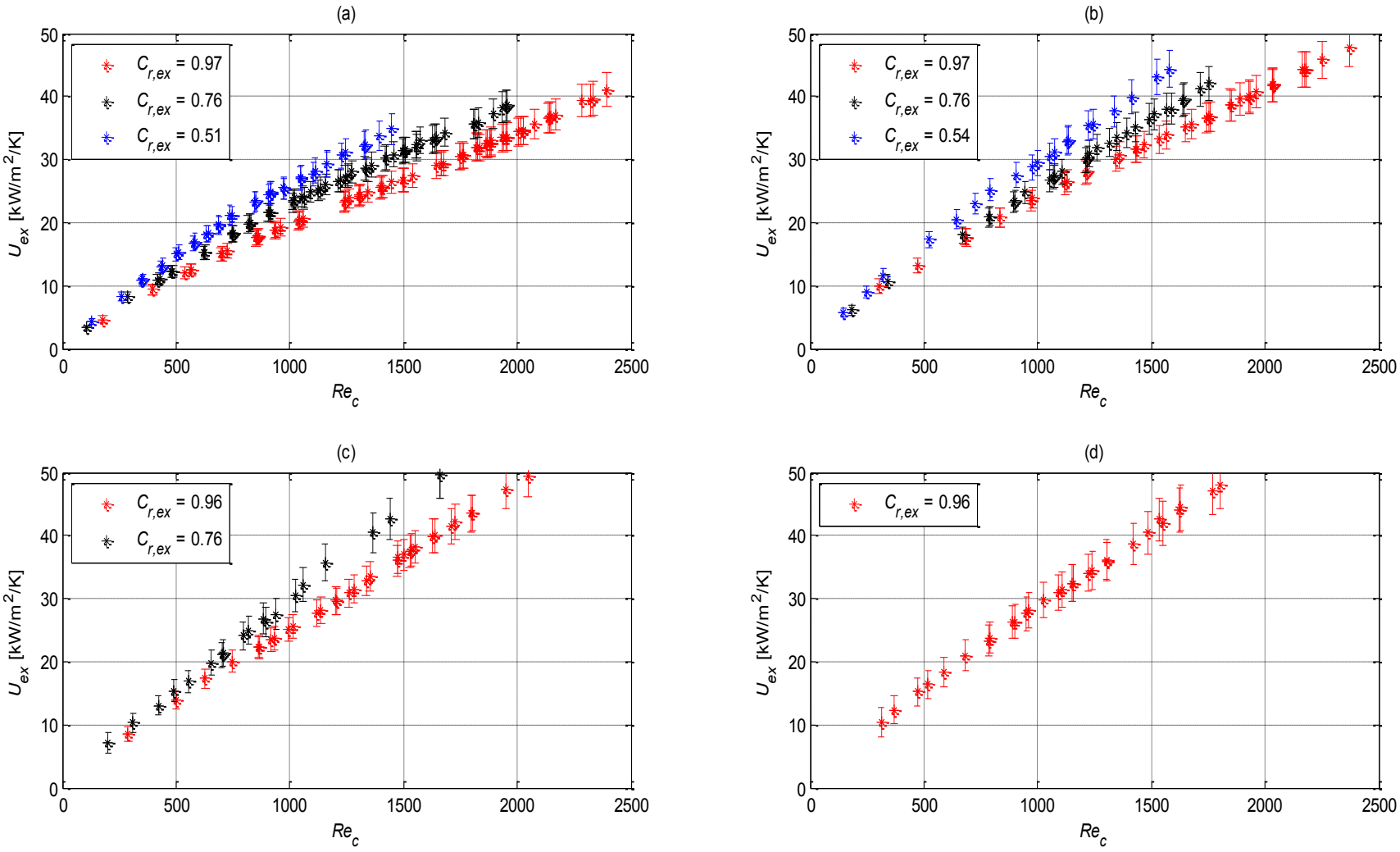

Figure 5.9 Effect of cold fluid Reynolds number and capacity rate ratio on overall heat transfer coefficient for different channel sizes: (a) Channel 1 (1000 µm), (b) Channel 2 (750 µm), (c) Channel 3 (500 µm), (d) Channel 4 (350 µm)

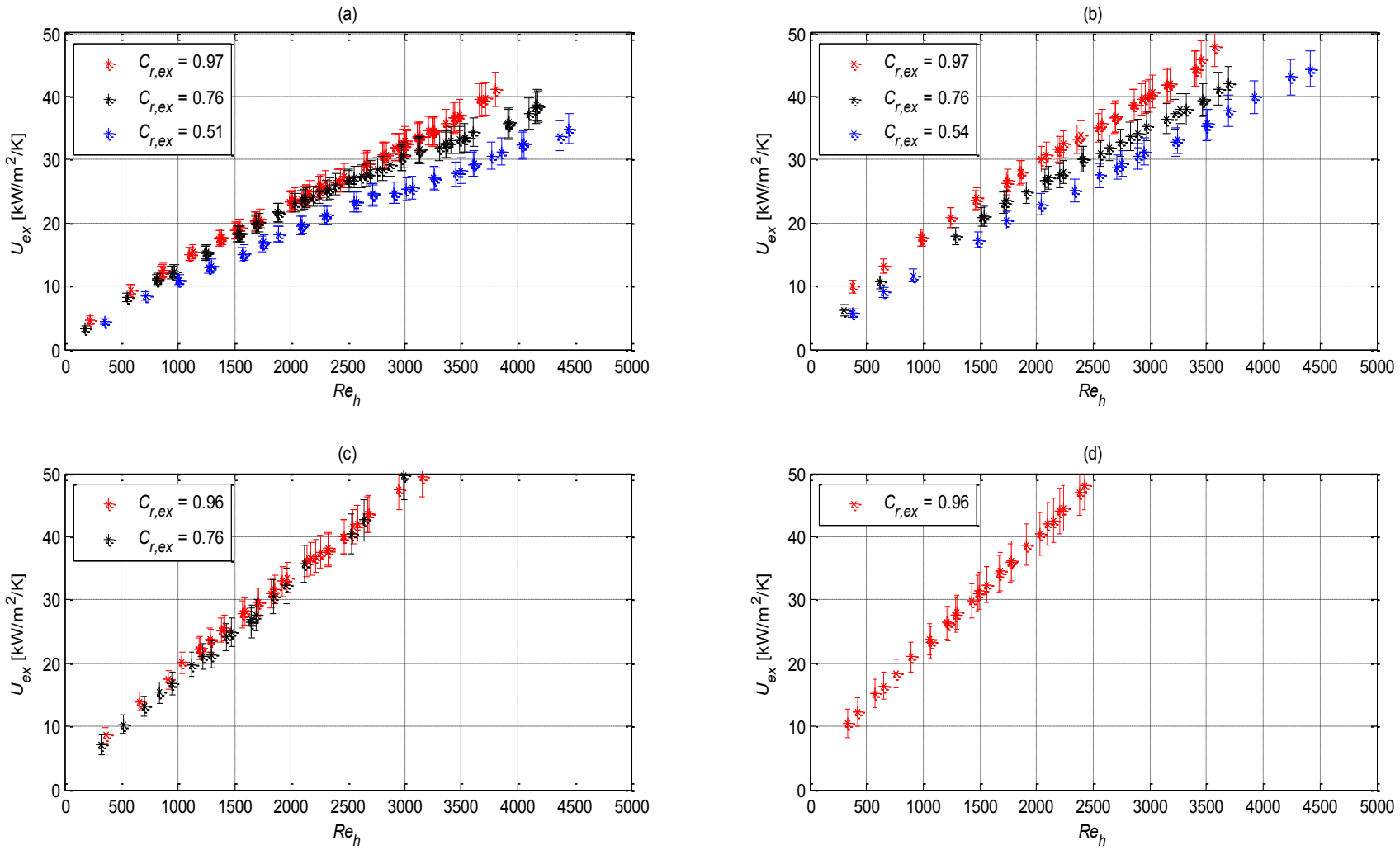

Figure 5.10 Effect of hot fluid Reynolds number and capacity rate ratio on overall heat transfer coefficient for different channel sizes: (a) Channel 1 (1000 µm), (b) Channel 2 (750 µm), (c) Channel 3 (500 µm), (d) Channel 4 (350 µm)

effect on U_{ex} is again due to the changes occurring in all the dependent variables with C_r. Figure 5.11 presents the same data in a form that allows direct comparison between the experimental overall heat transfer coefficients of the different systems operating at the same capacity rate ratios. Figure 5.11 (a) show U_{ex} as a function of Re_c for different systems having a capacity rate ratio of $C_r \sim 1$. It is clear that channel size and the overall heat transfer coefficients are inversely proportional. This relationship is primarily due to the decrease in heat transfer surface area with the decrease in channel size. The same trend is shown in Figures 5.11 (b) and (c), which present the overall heat transfer coefficient as a function of Re_c for all systems having capacity rate ratios of $C_r \sim 0.75$ and $C_r \sim 0.5$, respectively. Finally, Figures 5.11 (d), (e), and (f) present similar data for U_{ex} as a function of Re_h. The discussion provided for the effects of channel size on q_h also apply here. Table 5.4 summarizes the maximum and minimum experimental overall heat transfer coefficients achieved for each system for different capacity rate ratios along with the associated maximum and minimum Reynolds numbers for the cold and hot fluids.

5.2.2 Theoretical and Experimental Overall Heat Transfer Coefficients

The experimental overall heat transfer coefficient data were compared with theoretical values to ascertain how the heat exchangers actually performed compared to predictions. The theoretical overall heat transfer coefficients, $U_{th,1}$, are calculated from Eq. (3.17) assuming hydrodynamically and thermally fully developed flow. These values are then compared to the calculated experimental overall heat transfer coefficients. Figure 5.12 (a) presents this comparison for system 1 with different capacity rate ratios.

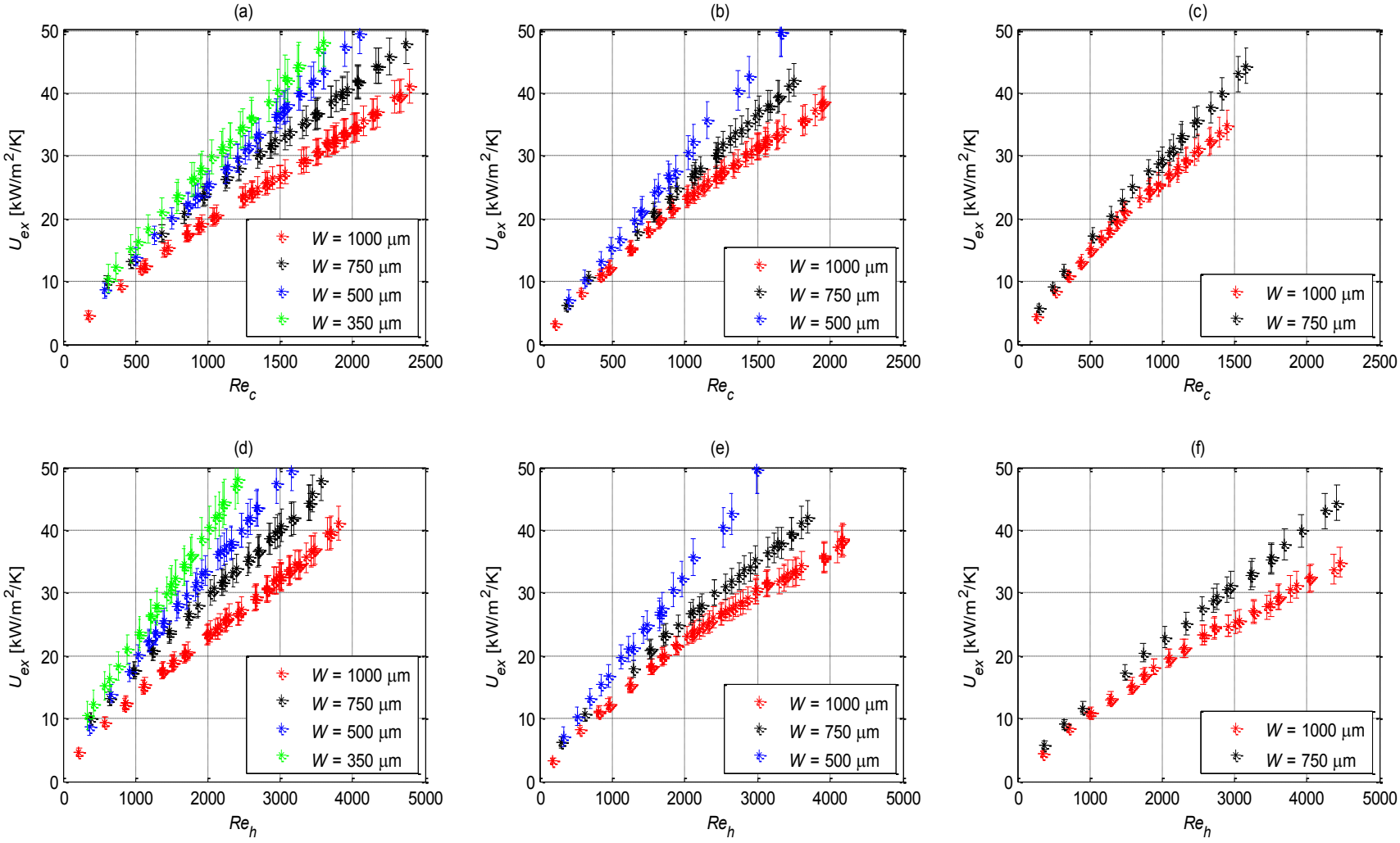

Figure 5.11 Effect of cold and hot fluid Reynolds numbers on overall heat transfer coefficient for different capacity rate ratios: (a) $C_r \sim 1$, (b) $C_r \sim 0.75$ (c) $C_r \sim 0.5$ (d) $C_r \sim 1$, (e) $C_r \sim 0.75$ (f) $C_r \sim 0.5$

Table 5.4 Maximum and minimum experimental overall heat transfer coefficients for all systems with different capacity rate ratios along with maximum and minimum associated Reynolds numbers for cold and hot fluids

System \ Variable		U_{ex} [kW/m^2/K]		Re_c		Re_h	
		Min.	Max.	Min.	Max.	Min.	Max.
System 1	C_r = 0.97	4.6162	41.059	175.42	2395.4	223.15	3803
	C_r = 0.76	3.2796	38.605	107.05	1954.6	184.68	4177.7
	C_r = 0.51	4.3682	34.83	130.66	1448.2	356.62	4451.2
System 2	C_r = 0.97	9.929	47.821	301.19	2369.1	379.73	3568.1
	C_r = 0.76	6.1702	42.104	181.32	1752.2	306.12	3692.7
	C_r = 0.54	5.8017	44.355	146.39	1580.3	376.19	4413.8
System 3	C_r = 0.96	8.5814	49.437	289.21	2046.5	361.16	3155.4
	C_r = 0.76	7.1461	49.59	201.3	1662.3	327.8	2994.6
System 4	C_r = 0.96	10.456	48.058	312.3	1803.6	335.93	2418.3

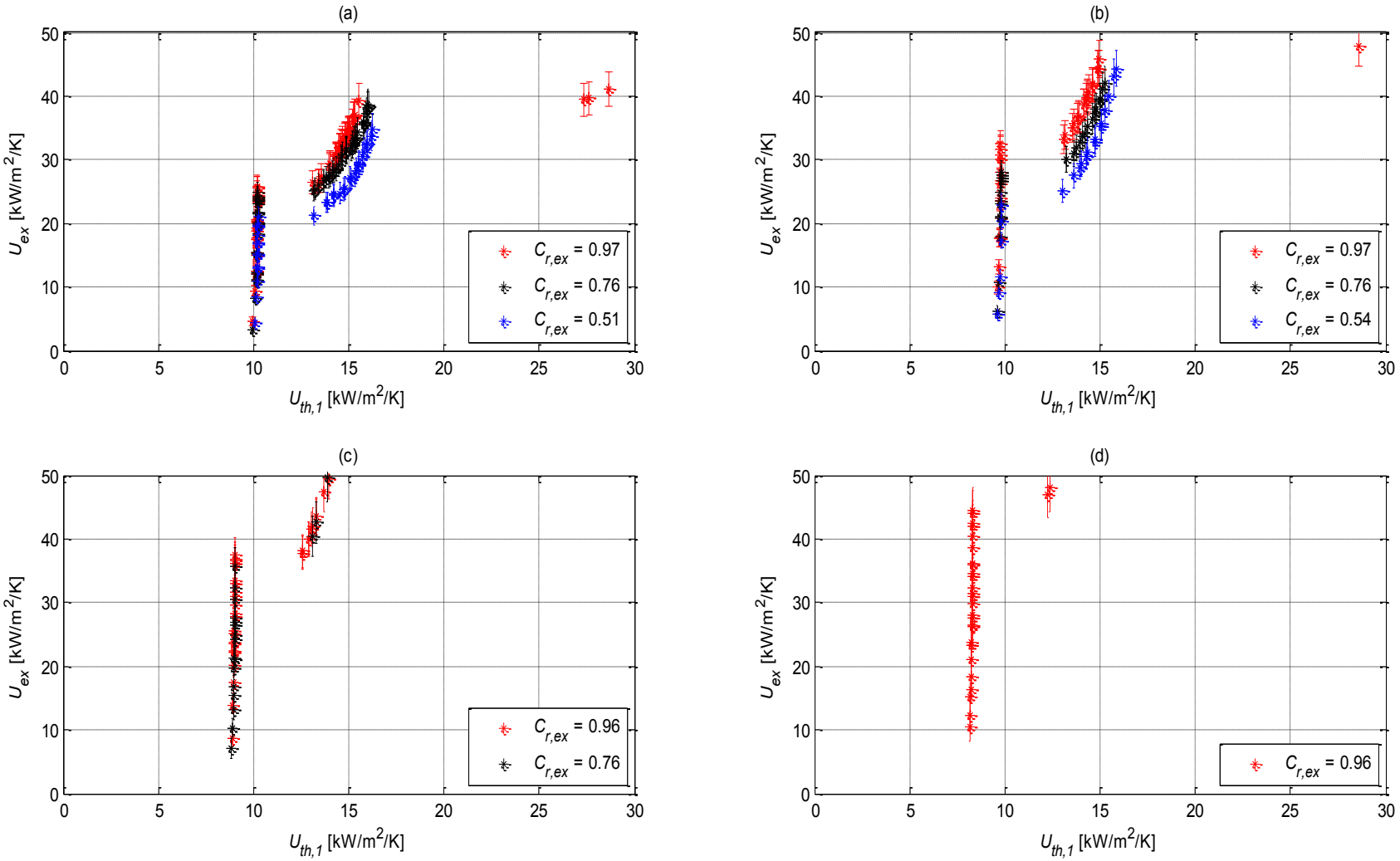

Figure 5.12 Theoretical and experimental overall heat transfer coefficient for all channels: (a) Channel 1 (1000 μm), (b) Channel 2 (750 μm), (c) Channel 3 (500 μm), (d) Channel 4 (350 μm)

As expected, the theoretical overall heat transfer coefficient remains constant as long as both flows are in the laminar regime, i.e., the heat transfer coefficient for fully developed internal flows is constant for laminar flow for either isoflux of isothermal boundary conditions. On the other hand, U_{ex} is dependent on the Reynolds number, which is not surprising since the two channel flows are not fully developed nor are the thermal boundary conditions completely isoflux or isothermal. When the channel flows become turbulent, individual theoretical heat transfer coefficients become Re dependent. While the relationship between the theoretical and experimental overall heat transfer coefficients is nearly linear for turbulent conditions, the experimental values are two to three times the theoretical predictions. This theoretical underprediction is primarily due to the assumption of fully developed internal flow. For developing flow, which occurs for much of the channel flow, local heat transfer coefficients are much greater than in the fully developed regions; thus, average internal heat transfer coefficients are greater for channels with significant development length. In the intermediate region where the theoretical overall heat transfer coefficients increase almost linearly with the experimental values, the hot fluid Reynolds number transitions the flow from laminar to turbulent. This affects the heat transfer coefficient of the hot fluid in Eq. (3.17), which results in the linear relationship with experimental values. Note again that the theoretical values in this region are almost 50% of the experimental ones. Figures 5.12 (b), (c), and (d) present the same comparison for systems 2, 3, and 4, respectively for different capacity rate ratios. Note that as the channel size decreases, the number of data for turbulent flow conditions decreases, which is due to the limitations placed on the attainable flow rate by pressure drop. From the data in Figure 5.12, it may be concluded

that the theoretical heat transfer coefficient for fully developed internal flows applied to the 1D thermal resistance analogy using Eq. (3.17) are not adequate to predict actual overall heat transfer coefficients. This approach clearly underestimates the overall heat transfer coefficient, making the theoretical model a poor design tool. The primary reason for the failure of this approach is the assumption that the flows are hydrodynamically and thermally fully developed. Another approach to predict the theoretical overall heat transfer coefficients was applied using Eq. (3.22) along with Eq. (4.10). In this approach, the calculated experimental heat exchanger effectiveness (Eq. 4.2.) is used to calculate the modified theoretical net transfer units $(NTU)_{th,2}$ from Eq. (4.10). Then, Eq. (3.22) is used with the experimental minimum heat capacity rate (C_{min}) and the corresponding heat transfer surface area to determine the modified theoretical overall heat transfer coefficient $U_{th,2}$. The heat transfer surface area used here is the same surface area used to determine the heat flux and the experimental overall heat transfer coefficients. Figure 5.13 presents the comparison of the predicted theoretical overall heat transfer coefficients from the new approach with the experimental overall heat transfer coefficients for all systems with different capacity rate ratios. The comparison shows almost 100% agreement between the theoretical and experimental data. This finding is observed for all systems and all capacity rate ratios. The reason of this perfect agreement is that the new approach uses the $\varepsilon - NTU$ method to predict the theoretical values while the experimental values are calculated using the log mean temperature difference (LMTD) method. In practice, these two methods are coupled as the $\varepsilon - NTU$ method is derived from the LMTD method, and hence, it is logical that the same overall heat transfer coefficient values are obtained. This observed agreement between the experimental

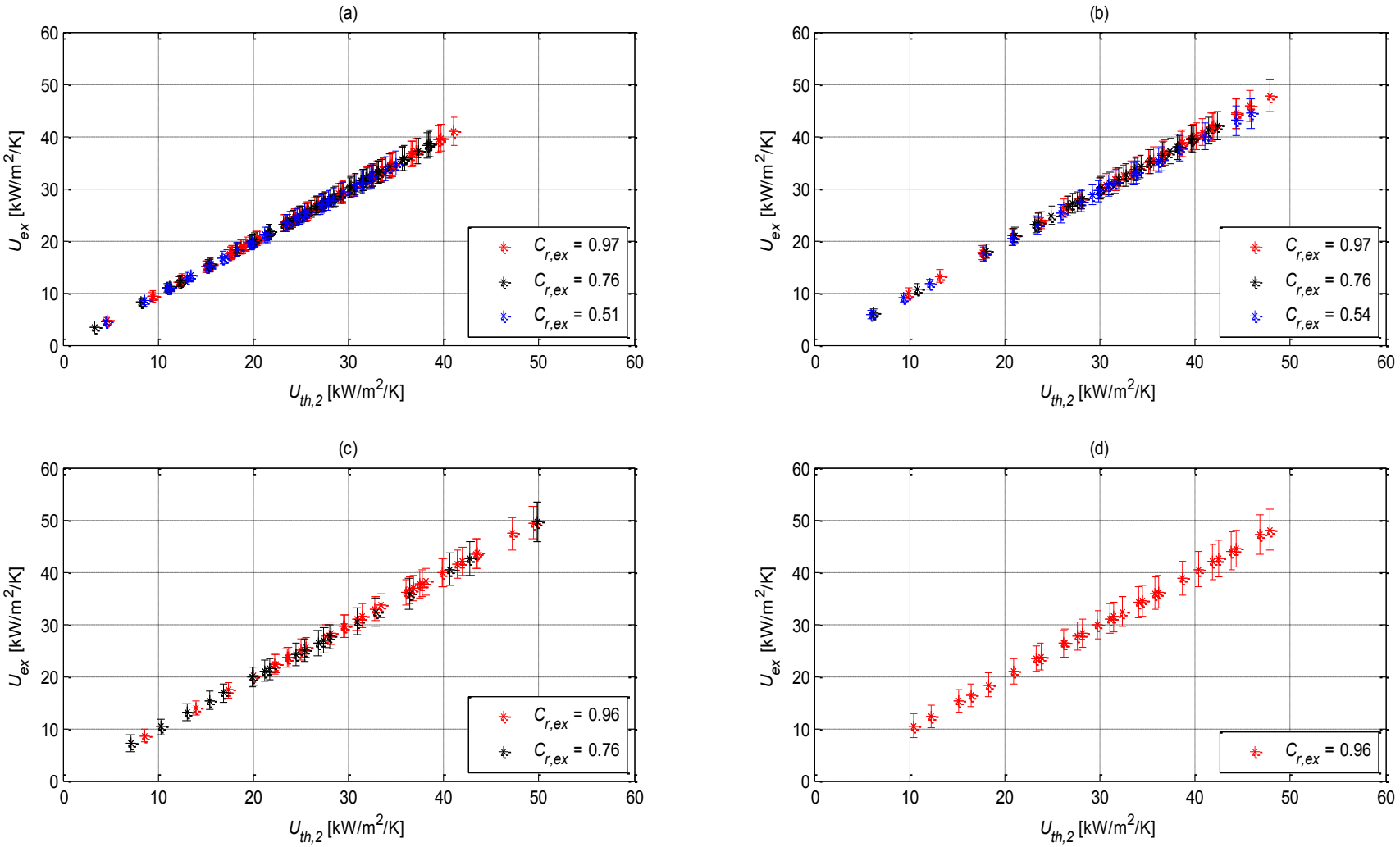

Figure 5.13 Theoretical and experimental overall heat transfer coefficient for all channels: (a) Channel 1 (1000 µm), (b) Channel 2 (750 µm), (c) Channel 3 (500 µm), (d) Channel 4 (350 µm)

and theoretical overall heat transfer coefficients suggests that the proposed correlation, Eq. (5.2), may be viewed as an acceptable design tool.

$$U = \frac{NTU_{th,2}\, C_{min}}{A_{ht}} \tag{5.2}$$

where $NTU_{th,2}$ is calculated from Eq. (4.10) with the desired effectiveness and capacity rate ratio and A_{ht} is calculated from Eq. (3.9). Eq. (5.2) is assumed to be valid for the conditions applied in the current study and for the range of C_{min} shown in Table 5.5.

Table 5.5 Range of C_{min} where Eq. (5.2) is valid

System		C_{min} [W/K]	
		Min.	Max.
System 1	C_r = 0.97	0.34643	4.0941
	C_r = 0.76	0.21044	3.4205
	C_r = 0.51	0.24245	2.4283
System 2	C_r = 0.97	0.43453	3.0674
	C_r = 0.76	0.26945	2.349
	C_r = 0.54	0.20891	2.0673
System 3	C_r = 0.96	0.31014	1.9741
	C_r = 0.76	0.21276	1.5494
System 4	C_r = 0.96	0.23397	1.2325

5.2.3 Overall Volumetric Heat Transfer Coefficient

A more common parameter used to evaluate the thermal performance of heat exchangers is the overall volumetric heat transfer coefficient U_{vol}. Figure 5.14 presents the experimental overall volumetric heat transfer coefficients for all the systems with different capacity rate ratios as a function of Re_c. U_{vol} is determined in the same way as U_{ex}, except the heat transfer surface area A_{ht} in Eq. 4.6 is replaced by the volume of the channel. This replacement means that U_{vol} is 10^4 times U_{ex} as the volume is calculated as A_{ht} times the channel height $H \sim 100$ μm. Thus, the trends demonstrated by the U_{ex} data and their explanations are unchanged for U_{vol}. Figure 5.15 presents the experimental overall volumetric heat transfer coefficient for all systems with different capacity rate ratios as a function of Re_h. Finally, Figure 5.16 presents a comparison between the experimental overall volumetric heat transfer coefficients for the different systems having the same capacity rate ratios. Table 5.6 summarizes the maximum and minimum experimental overall volumetric heat transfer coefficients achieved for each system for different capacity rate ratios along with the associated maximum and minimum Reynolds number for the cold and hot fluids.

5.3 Heat Exchanger Effectiveness

Heat exchanger effectiveness data are valuable for researchers and designers. Figure 5.17 presents the data for heat exchanger experimental effectiveness (ε_{ex}) as a function of experimental net transfer units (NTU_{ex}) along with the analytical solutions for all systems with different capacity rate ratios. ε_{ex} is determined from Eq. (4.2) and NTU_{ex} is determined from Eq. (4.7) using the experimental average heat rate for the

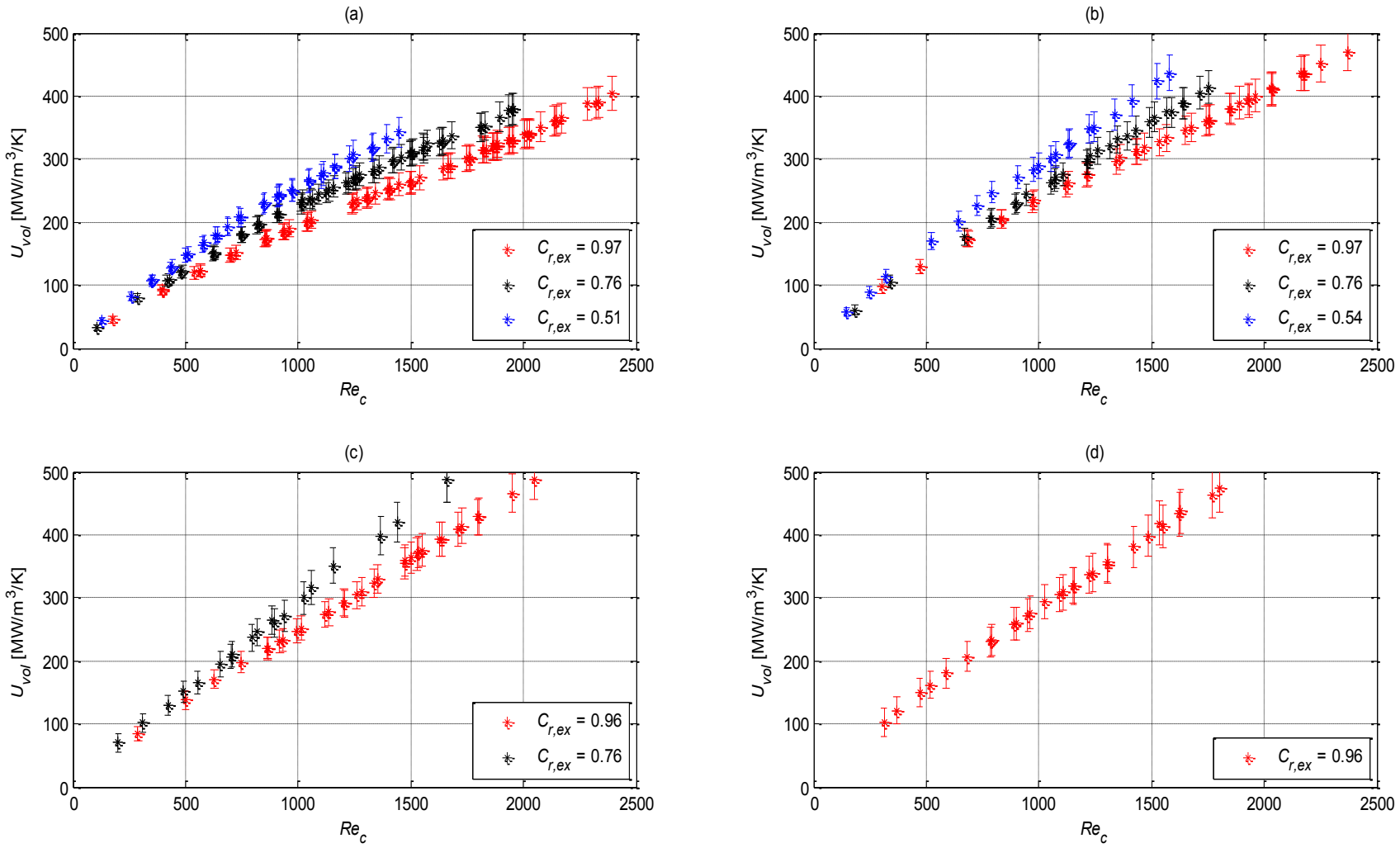

Figure 5.14 Effect of cold fluid Reynolds number on overall volumetric heat transfer coefficient for different channel sizes: (a) Channel 1 (1000 µm), (b) Channel 2 (750 µm), (c) Channel 3 (500 µm), (d) Channel 4 (350 µm)

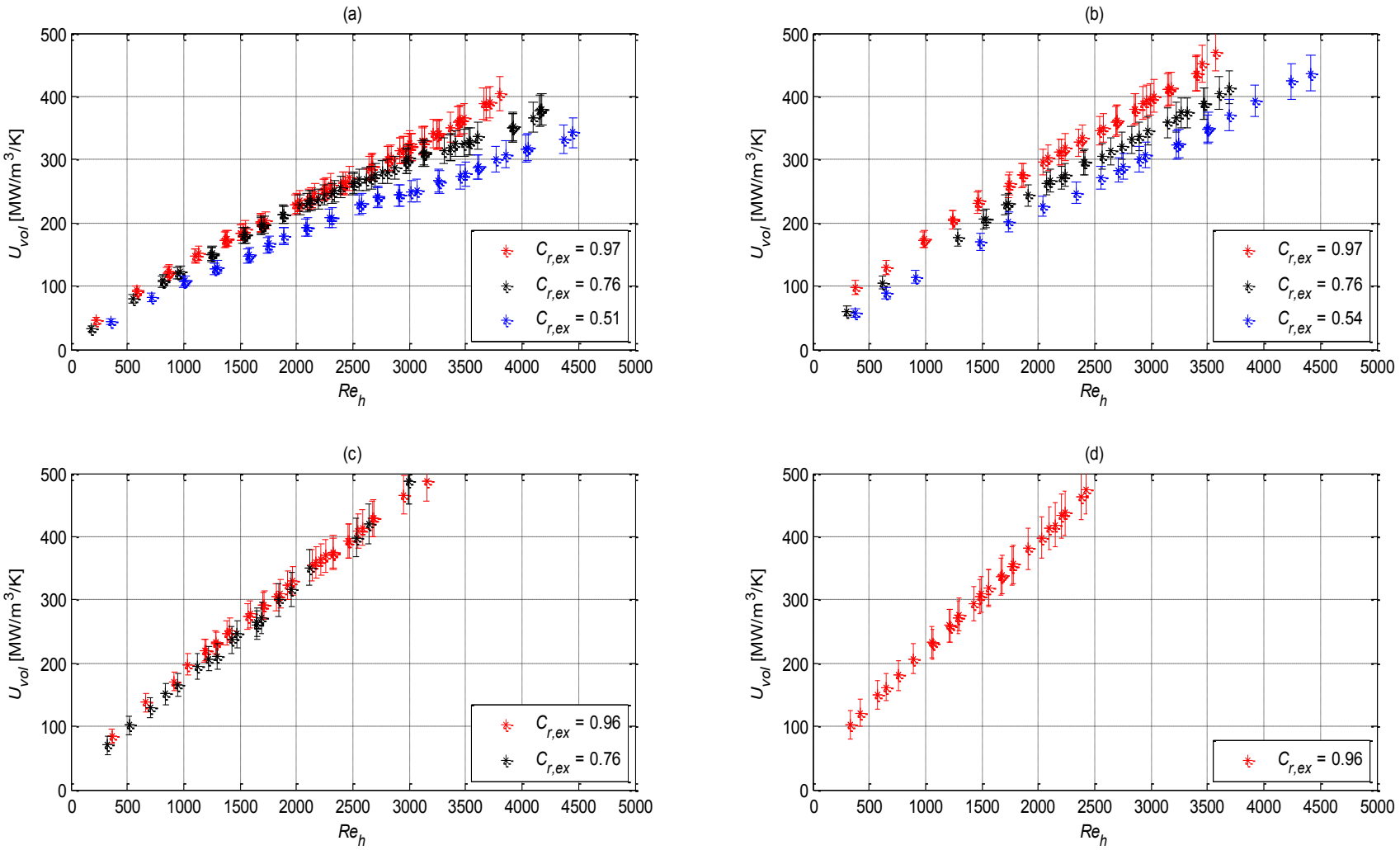

Figure 5.15 Effect of hot fluid Reynolds number on overall volumetric heat transfer coefficient for different channel sizes: (a) Channel 1 (1000 µm), (b) Channel 2 (750 µm), (c) Channel 3 (500 µm), (d) Channel 4 (350 µm)

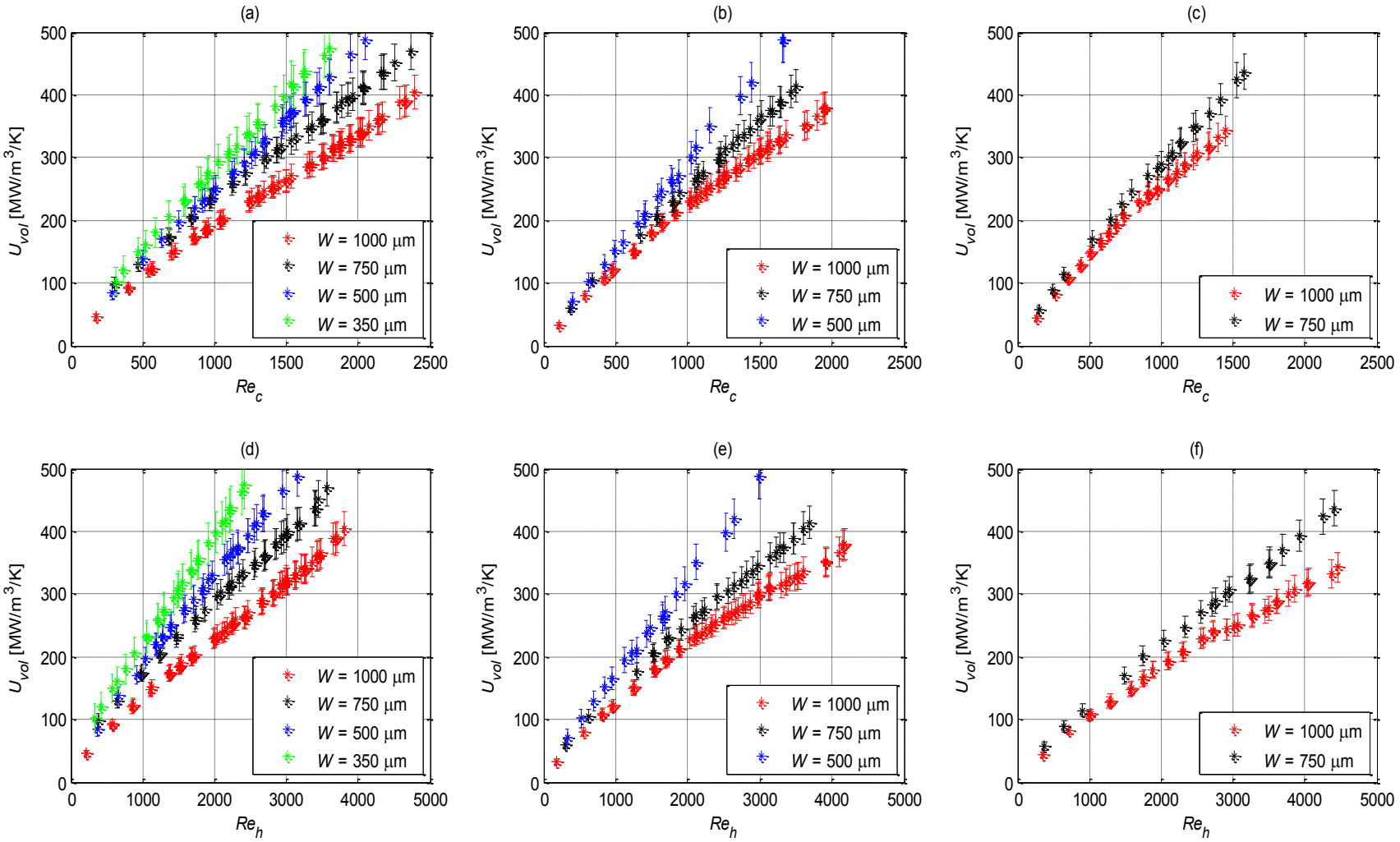

Figure 5.16 Effect of cold and hot fluid Reynolds numbers on volumetric overall heat transfer coefficient for different capacity rate ratios: (a) $C_r \sim 1$, (b) $C_r \sim 0.75$ (c) $C_r \sim 0.5$ (d) $C_r \sim 1$, (e) $C_r \sim 0.75$ (f) $C_r \sim 0.5$

Table 5.6 Maximum and minimum experimental overall volumetric heat transfer coefficients for all systems with different capacity rate ratios along with maximum and minimum associated Reynolds number for the cold and hot fluids

System \ Variable		U_{vol} [MW/m^3/K]		Re_c		Re_h	
		Min.	Max.	Min.	Max.	Min.	Max.
System 1	C_r = 0.97	45.435	404.13	175.42	2395.4	223.15	3803
	C_r = 0.76	32.28	379.97	107.05	1954.6	184.68	4177.7
	C_r = 0.51	42.994	342.81	130.66	1448.2	356.62	4451.2
System 2	C_r = 0.97	97.727	470.68	301.19	2369.1	379.73	3568.1
	C_r = 0.76	60.73	414.41	181.32	1752.2	306.12	3692.7
	C_r = 0.54	57.103	436.57	146.39	1580.3	376.19	4413.8
System 3	C_r = 0.96	84.462	486.59	289.21	2046.5	361.16	3155.4
	C_r = 0.76	70.336	488.09	201.3	1662.3	327.8	2994.6
System 4	C_r = 0.96	102.91	473.01	312.3	1803.6	335.93	2418.3

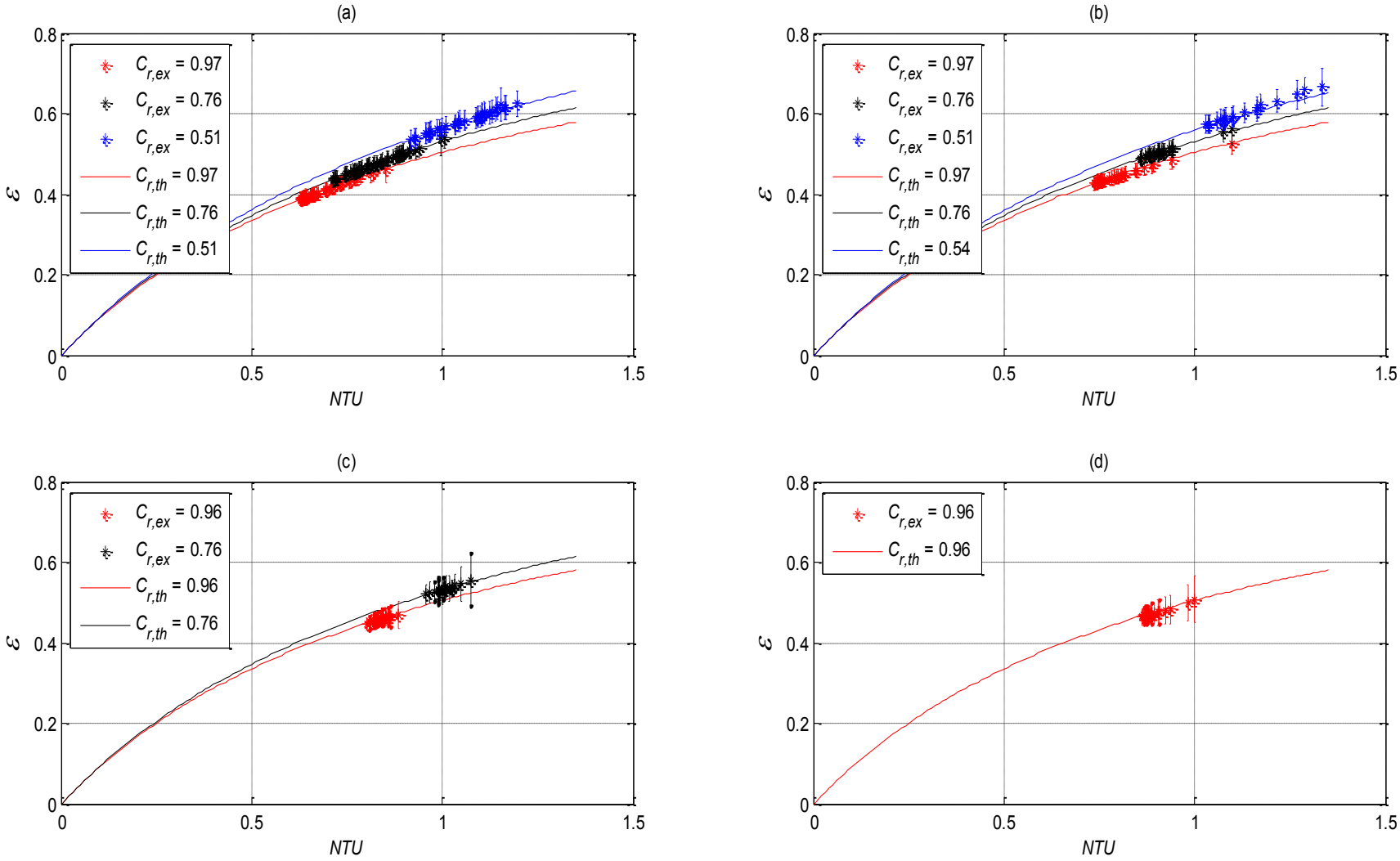

Figure 5.17 Heat exchanger effectiveness as a function of net transfer units for different channel sizes: (a) Channel 1 (1000 µm), (b) Channel 2 (750 µm), (c) Channel 3 (500 µm), (d) Channel 4 (350 µm)

system, Eq. (4.1) and Eq. (3.22.). The solid colored lines represent the analytical expression of $\varepsilon(NTU)$ as determined from Eq. (3.23.) with NTU ranging from 0 to 1.5. Figure 5.17 (a) shows the thermal performance of system 1 for three different capacity rate ratios. The experimental $\varepsilon - NTU$ data agree very well with the analytical expressions. The capacity rate ratio term applied in the analytical expression (Eq. 3.23) is the average experimental capacity rate ratio for each experiment. For this reason some theoretical data deviate slightly from the experimental data. However, these deviations are not significant and it may be concluded that there is strong agreement between theory and the experiment. The $\varepsilon(NTU)$ data for systems 2, 3, and 4 presented in Figure 5.17 (b), (c), and (d), respectively, exhibit similar agreement as that for system 1. It was initially believed that the $\varepsilon(NTU)$ data might not agree with the analytical expressions since the analytical expression were derived for a concentric tube counterflow heat exchanger. However, it is clear that the concentric tube counterflow heat exchanger $\varepsilon - NTU$ relations can adequately predict the thermal performance of the current microchannel heat exchanger when the appropriate boundary and operating conditions are applied. A comparison between the theoretical $(\varepsilon - NTU)_{th,1}$ and experimental $(\varepsilon - NTU)_{ex}$ for systems 1, 2, 3, and 4 are shown in Figures 5.18, 5.19, 5.20, and 5.21, respectively, for different capacity rate ratios. The theoretical overall heat transfer coefficient ($U_{th,1}$), determined using the thermal circuit analogy from Chapter 3, is used to determine the theoretical NTU, $(NTU)_{th,1}$, using Eq. (3.22) and the measured minimum capacity rate (C_{min}). Then, the theoretical effectiveness ($\varepsilon_{th,1}$) is determined from Eq. (3.23) using the previously determined $(NTU)_{th,1}$ and the measured average

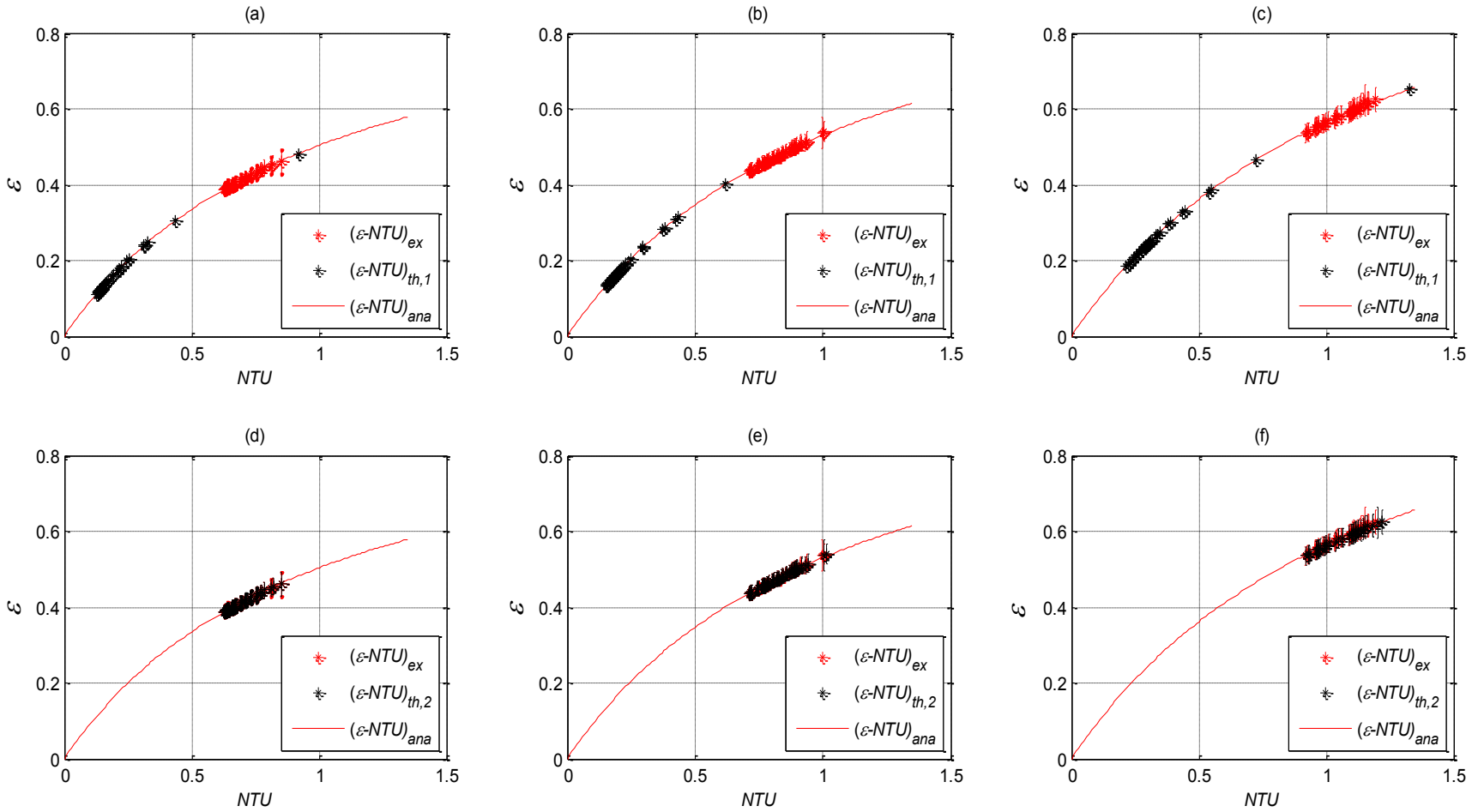

Figure 5.18 Comparison between theoretical and experimental effectiveness and NTU with different definitions for channel 1 (1000 μm) for different capacity rate ratios: (a) $C_r \sim 1$, (b) $C_r \sim 0.75$ (c) $C_r \sim 0.5$ (d) $C_r \sim 1$, (e) $C_r \sim 0.75$ (f) $C_r \sim 0.5$

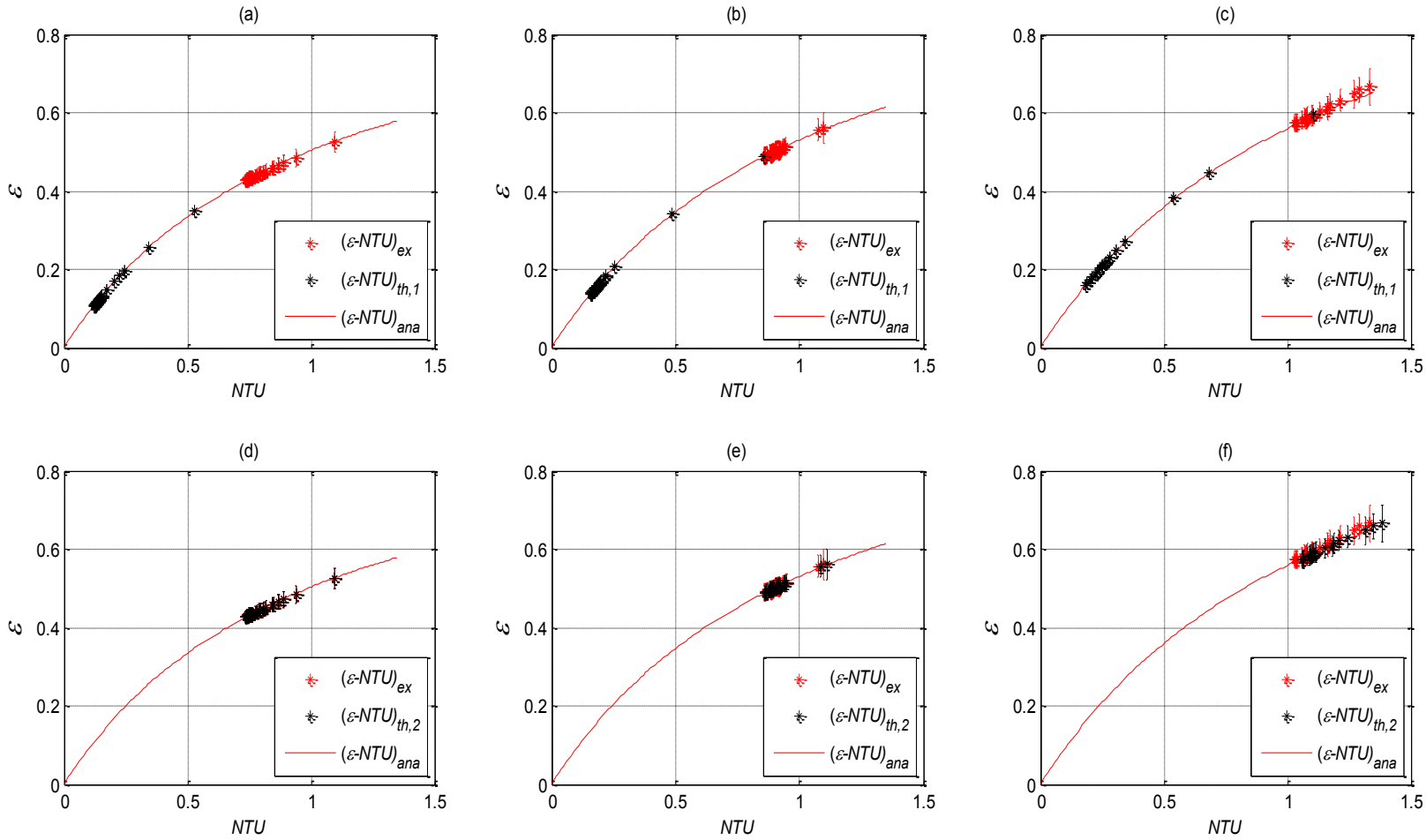

Figure 5.19 Comparison between theoretical and experimental effectiveness and NTU with different definitions for channel 2 (750 μm) for different capacity rate ratios: (a) $C_r \sim 1$, (b) $C_r \sim 0.75$ (c) $C_r \sim 0.5$ (d) $C_r \sim 1$, (e) $C_r \sim 0.75$ (f) $C_r \sim 0.5$

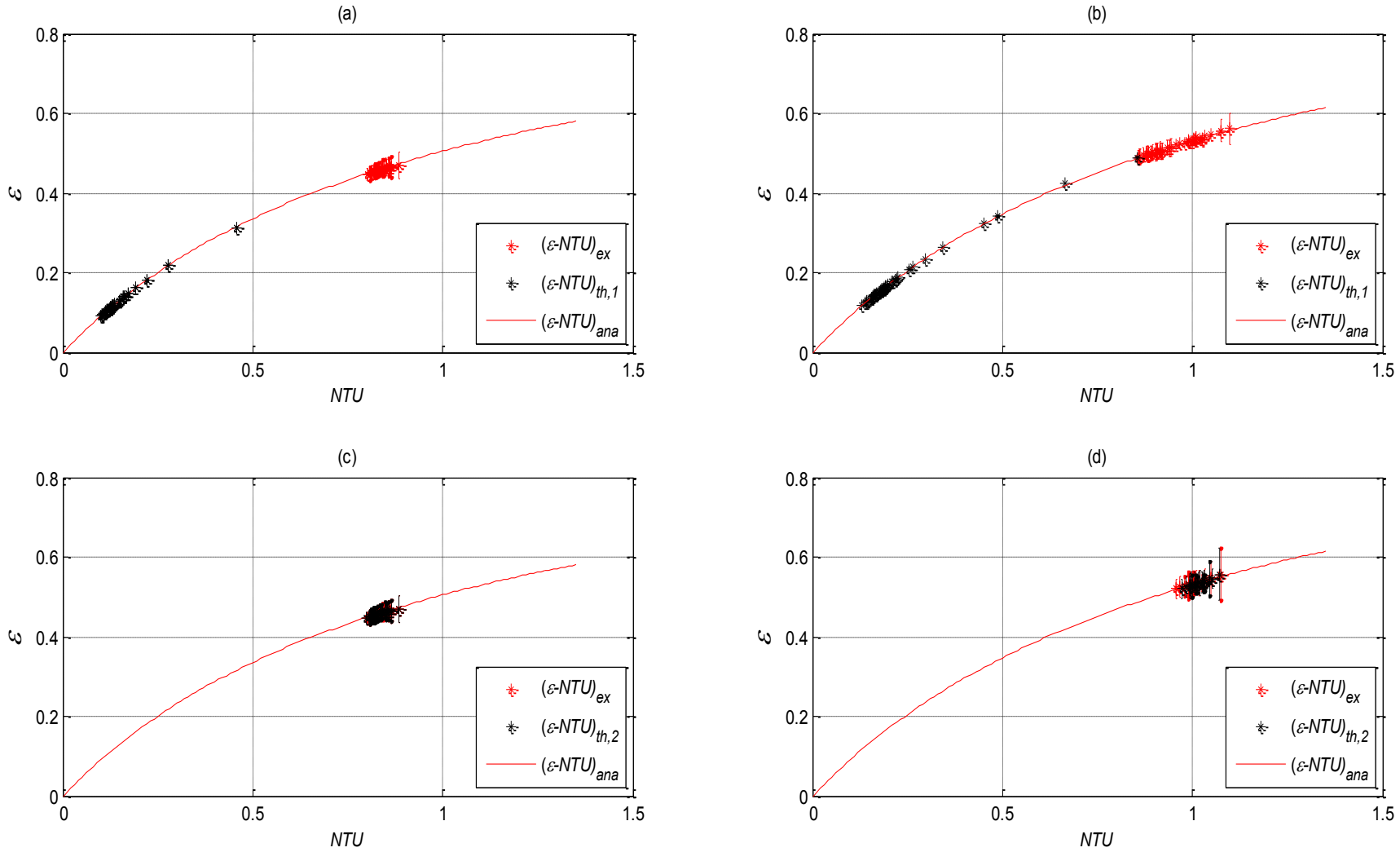

Figure 5.20 Comparison between theoretical and experimental effectiveness and NTU with different definitions for channel 3 (500 μm) for different capacity rate ratios: (a) $C_r \sim 1$, (b) $C_r \sim 0.75$ (c) $C_r \sim 1$ (d) $C_r \sim 0.75$

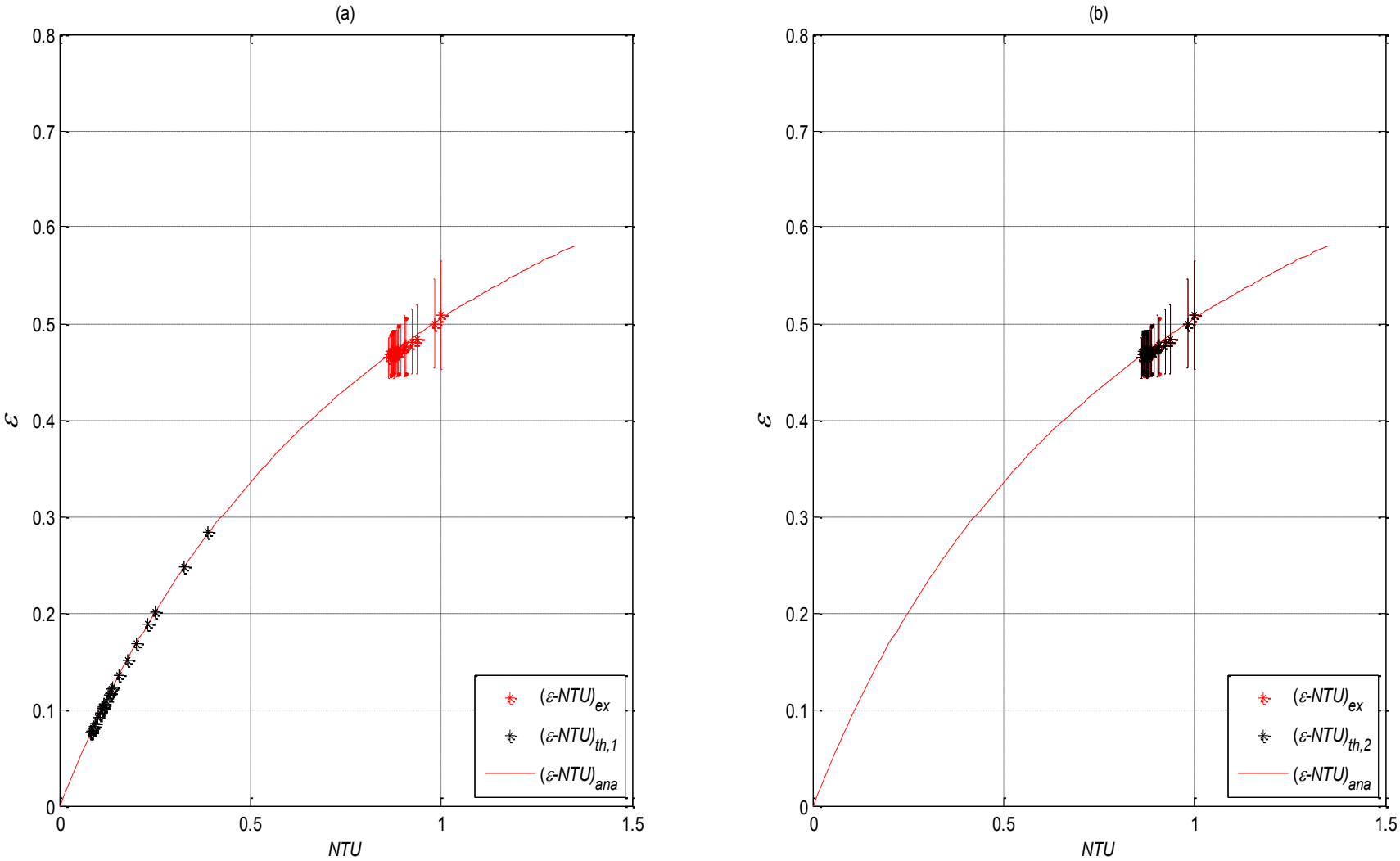

Figure 5.21 Comparison between theoretical and experimental effectiveness and NTU using the different definitions for the theoretical relationship for channel 4 (350 μm) for $C_r \sim 1$

capacity rate ratio. Finally, these two theoretical values $(\varepsilon - NTU)_{th,1}$ are plotted with the experimental values $(\varepsilon - NTU)_{ex}$ and the analytical $(\varepsilon - NTU)_{ana}$ expression for the conventional concentric tube counterflow heat exchanger using Eq. (3.23) in the same manner used for Figure 5.17. The data in Figures 5.18 (a, b, c), 5.19 (a, b, c), 5.20 (a, b), and 5.21 (a) clearly show that the proposed theoretical $(\varepsilon - NTU)_{th,1}$ relationship based on the thermal circuit analysis approach underestimates the thermal performance for all systems. This finding is similar to the poor agreement found between the predicted theoretical overall heat transfer coefficient $(U_{th,1})$ and the experimental overall heat transfer coefficient (U_{ex}) found in Figure 5.12 and discussed earlier in section 5.2.2. A second theoretical $\varepsilon(NTU)$ relationship is determined using the experimental effectiveness and the average capacity rate ratio data to calculate the theoretical net transfer units $(\varepsilon - NTU)_{ex}$ using Eq. (4.10). The term $(NTU)_{th,2}$ is referred to as the modified theoretical NTU. When this modified NTU is calculated and plotted against the experimental effectiveness values, a very strong agreement between the experimental and theoretical values is found. This strong agreement confirms that the concentric counterflow heat exchanger relation is an acceptable means to predict the thermal performance of the heat exchangers used in the current study, assuming the same boundary and operating conditions are applied. This strong agreement is similar to that found for the modified theoretical overall heat transfer coefficient $(U_{th,2})$, discussed in section 5.2.2, since the approach is the same. The legends in Figures 5.18, 5.19, 5.20, and 5.21 indicate the data representing the experimental values $(\varepsilon - NTU)_{ex}$, the theoretical values $(\varepsilon - NTU)_{th,1}$, the modified theoretical values $(\varepsilon - NTU)_{th,2}$, and the analytical

expression $(\varepsilon - NTU)_{ana}$. Table 5.7 summarizes the maximum and minimum experimental heat exchanger effectiveness and NTU achieved for each system for the different capacity rate ratios along with the associated maximum and minimum Reynolds numbers for cold and hot fluids.

5.4 Exergy Analysis

5.4.1 Fluid-based Exergy Efficiency

An exergy analysis has become an important thermodynamic tool over the last few decades to assess a system's overall performance. An exergy analysis can be conducted using exergy efficiency as the parameters of interest. Two different exergy efficiency definitions have been proposed by different authors [26 and 27] and each is applied to assess the heat exchanger performance. The first definition, discussed in this section, analyzes the exergy efficiency based on exergy changes to the two fluids (Eq. (4.15)). Specifically the fluids-based exergy efficiency η_{ch} equals the ratio of the exergy change in the cold fluid to that in the hot fluid. Figure 5.22 shows the exergy efficiency for all systems with different capacity rate ratios as a function of the cold fluid Reynolds number Re_c. As shown in Figure 5.22 (a), the exergy efficiency increases with increasing Reynolds number to a maximum value and then decreases with increasing Reynolds number. This trend suggests that operating at higher Reynolds numbers is not desired. For system 1, shown in Figure 5.22 (a), and for the three different capacity rate ratios, the data suggest that the optimum Reynolds number range to operate is near 500.

Table 5.7 Maximum and minimum experimental heat exchanger effectiveness and NTU for all systems with different capacity rate ratios along with the associated maximum and minimum Reynolds numbers for cold and hot fluids

System \ Variable		ε_{ex}		NTU_{ex}		Re_c		Re_h	
		Min.	Max.	Min.	Max.	Min.	Max.	Min.	Max.
System 1	$C_r = 0.97$	0.38752	0.46012	0.627	0.85281	175.42	2395.4	223.15	3803
	$C_r = 0.76$	0.43599	0.53927	0.71311	1.0064	107.05	1954.6	184.68	4177.7
	$C_r = 0.51$	0.53547	0.6249	0.91797	1.1955	130.66	1448.2	356.62	4451.2
System 2	$C_r = 0.97$	0.42648	0.52613	0.73596	1.0968	301.19	2369.1	379.73	3568.1
	$C_r = 0.76$	0.48807	0.56236	0.85824	1.0991	181.32	1752.2	306.12	3692.7
	$C_r = 0.54$	0.57392	0.66586	1.0299	1.333	146.39	1580.3	376.19	4413.8
System 3	$C_r = 0.96$	0.44651	0.47017	0.80137	0.88541	289.21	2046.5	361.16	3155.4
	$C_r = 0.76$	0.52027	0.55632	0.95773	1.0748	201.3	1662.3	327.8	2994.6
System 4	$C_r = 0.96$	0.46408	0.50828	0.8625	1.001	312.3	1803.6	335.93	2418.3

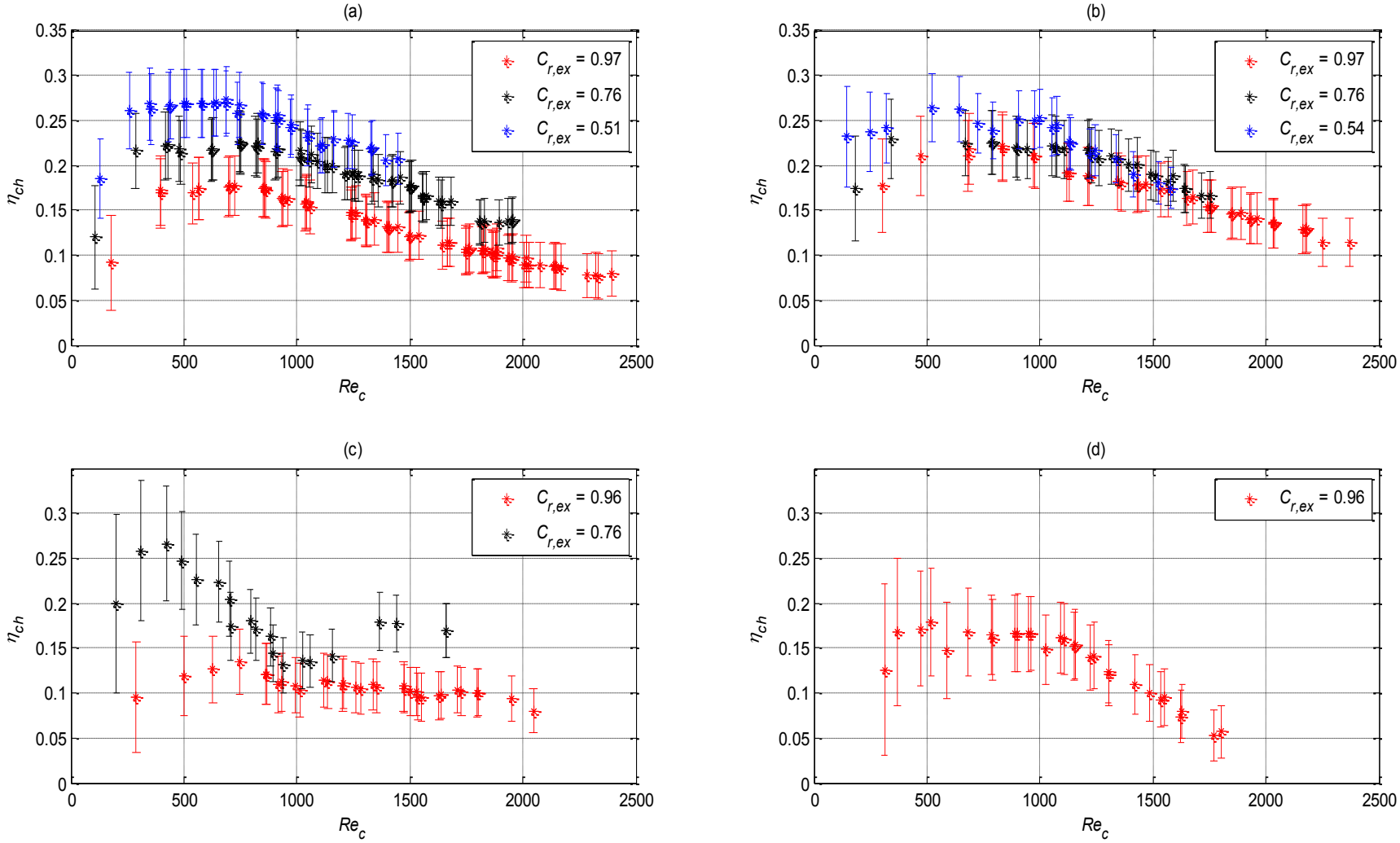

Figure 5.22 Fluid based exergy efficiency as a function of Reynolds number for the cold fluid for all channels: (a) Channel 1 (1000 µm), (b) Channel 2 (750 µm), (c) Channel 3 (500 µm), (d) Channel 4 (350 µm)

Since the Reynolds numbers for the cold and hot fluids are different, the optimum hot fluid Reynolds number to operate is approximately 1000, as shown in Figure 5.23. From Figure 5.22 (a) it can also be concluded that the exergy efficiency increases with the decrease of capacity rate ratio. This finding is primarily due to the higher enthalpy values in Eq. (4.12). Since the cold fluid flow was the variable controlled to produce the different capacity rate ratios, and since the cold exergy terms are in the numerator, the increase in η_{ch} with decease in C_r can be directly related to the enthalpy terms. Since the mass flow rate of the cold fluid is reduced to produce lower capacity rate ratios, the cold fluid outlet temperature increases. Thus, the outlet enthalpy term in Eq. (4.12) increases with the reduction of the capacity rate ratio and, hence, the total exergy efficiency increases with decreasing capacity rate ratio. In addition, the cold fluid flow was controlled at the outlet of the heat exchanger by adjusting the needle valve, which causes the cold fluid outlet pressure to increase.

The enthalpy term is pressure and temperature dependent. Since both the outlet temperature and outlet pressure of the cold fluid flow increase with a decrease in flow rate, the enthalpy term increases as well. The exergy efficiency is dependent on enthalpy and entropy. However, entropy has less effect than enthalpy. It should also be noted that the increase in enthalpy change for the cold fluid offsets the reduction in cold fluid mass flow rate; both terms are in the numerator of the exergy efficiency definition. For these reasons, the exergy efficiency increases with the lower capacity rate ratios. The reference state is standard pressure and temperature (P = 101.325 kPa, T = 25 °C). Choosing a different reference state will result in changes to the data, but not any changes to the trends. Figure 5.22 (b) presents the exergy efficiency for system 2 with different capacity

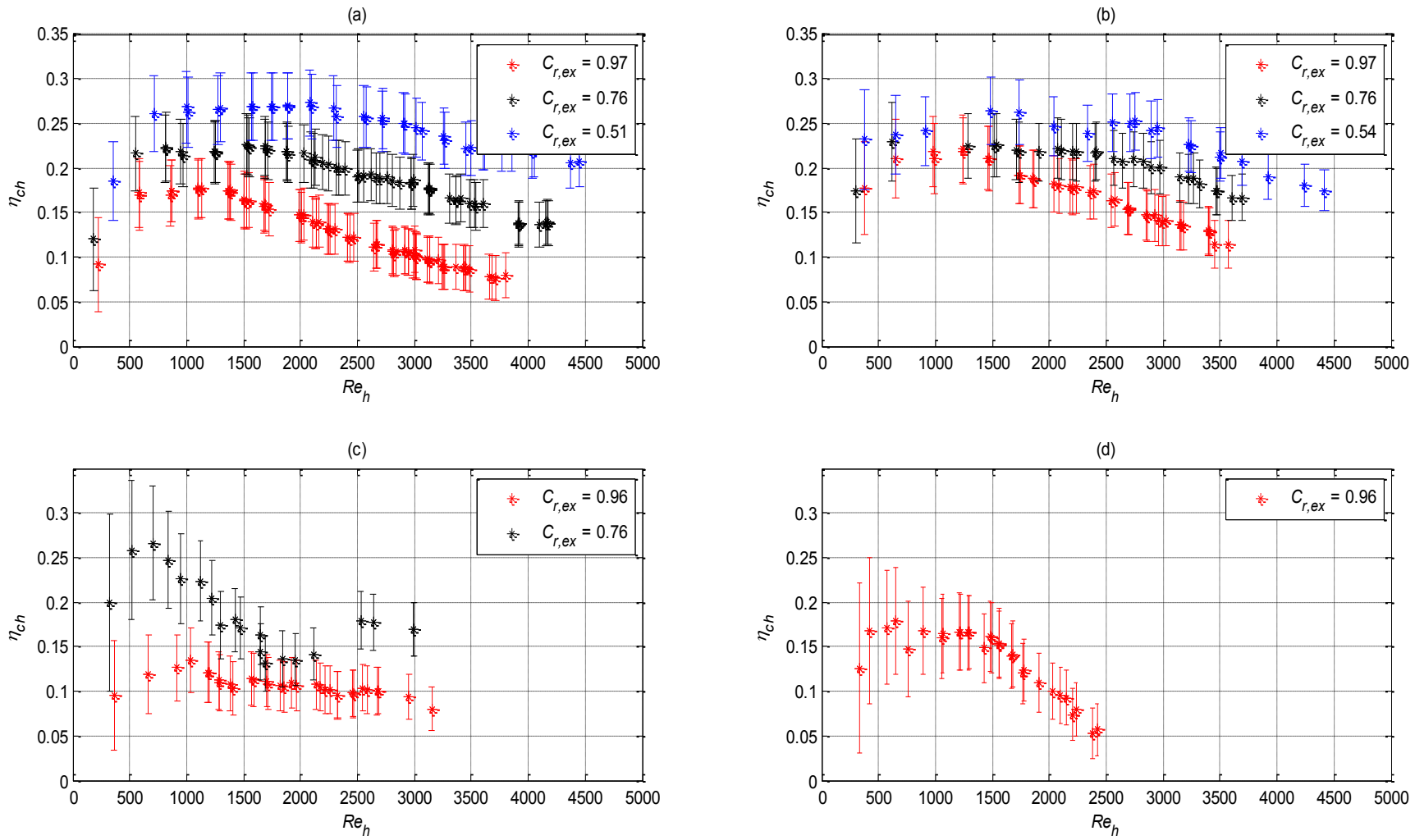

Figure 5.23 Fluid-based exergy efficiency as a function of hot fluid Reynolds number for all channels: (a) Channel 1 (1000 µm), (b) Channel 2 (750 µm),(c) Channel 3 (500 µm), (d) Channel 4 (350 µm)

rate ratios. The same trends found for system 1 apply for system 2. Figure 5.22 (c) presents the exergy efficiency for system 3 for the available two different capacity rate ratios. Similar behavior as in the previous systems is observed. However, for C_r = 0.76 the last three data points deviate from the decreasing trend, which is likely due to a change to the test system during the experiment when the thermocouples were reattached after the system was disconnected from the flow loop. Figure 5.22 (d) presents the exergy efficiency for system 4. Figure 5.23 presents the exergy efficiency for all the systems as a function of the Reynolds number for the hot fluid.

A final comparison of fluid-based exergy efficiency for all the systems and for each capacity rate ratio as a function of both the cold and hot fluid Reynolds numbers is presented in Figure 5.24. In Figure 5.24 (a), where all the systems are compared for the capacity rate ratio C_r ~ 1, the 750 μm channel has higher exergy efficiency than the 1000 μm channel. Also, the 350 μm channel has higher exergy efficiency than the 500 μm channel. However, the trends for the smaller two channels, 500 μm and 350 μm, are both below those for the larger two channels, 1000 μm and 750 μm. This inconsistency is believed to be attributed to the lower mass flow rates in the smaller channels. For the second capacity rate ratio, C_r ~ 0.75, the data for the larger two channels, 1000 μm and 750 μm, are nearly equivalent. On the other hand, the 500 μm data are greater than that for the larger two channels for Re_c < 500 and lower than the larger two channels for larger Re_c. These trends are not easily explained; however, they are most likely the result of the interrelated changes to mass flow rates and outlet temperatures that occur when the lower C_r conditions are created. The lowest capacity rate ratio for all systems, C_r ~ 0.5, is presented in Figure 5.24 (c). Here the data trends for the two channels are nearly the same

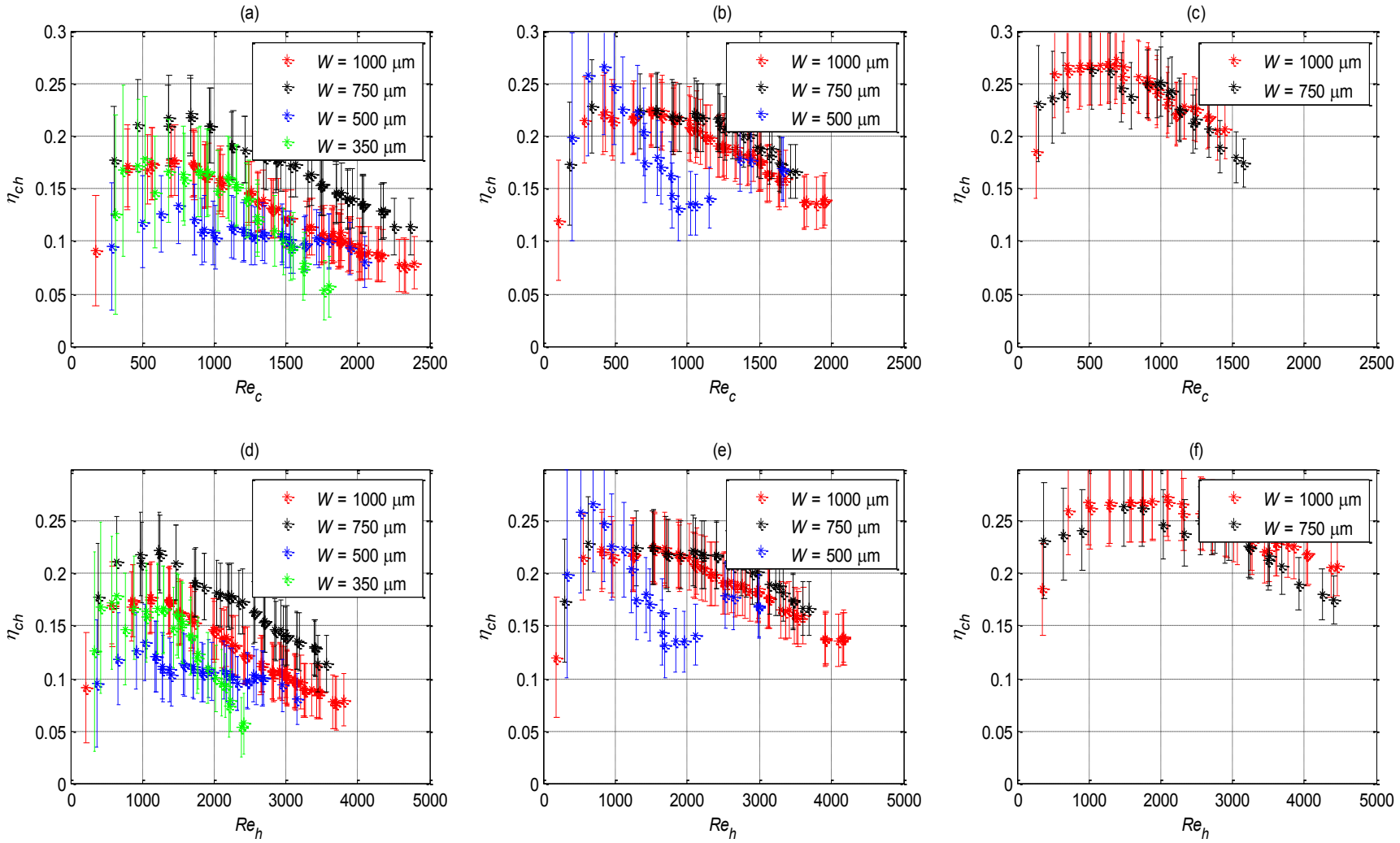

Figure 5.24 Effect of cold and hot fluid Reynolds numbers on fluid-based exergy efficiency for different capacity rate ratios: (a) $C_r \sim 1$, (b) $C_r \sim 0.75$ (c) $C_r \sim 0.5$ (d) $C_r \sim 1$, (e) $C_r \sim 0.75$ (f) $C_r \sim 0.5$

and within the uncertainty limits. Figure 5.24 (d), (e), and (f) present the fluid-based exergy efficiency for all systems for each capacity rate ratio as a function of the hot fluid Reynolds number. Examining the data in Figure 5.24, no general conclusion for the exergy efficiency for a specific capacity rate ratio as a function of the channel size can be formed. However, channels that are about ~ 25% smaller in size have higher exergy efficiency for the same capacity rate ratio. Finally, from examining Figures 5.22, 5.23, and 5.24, it can be concluded that the higher exergy efficiencies are achieved in the laminar region, which does not require higher flow rates, and, hence, lower pressure driving force is required. Table 5.8 provides the minimum and maximum fluid-based exergy efficiencies for all systems with their respective capacity rate ratios along with the associated minimum and maximum Reynolds numbers for the cold and hot fluids. It should be noted that the exergy efficiency data presented in this chapter are underestimated; however, all trends are valid. The changes to the absolute exergy are due to the pressure measurements of the inlet and outlet flows. The inlet pressure sensors for both channels were located about 20 cm upstream of the test section while the outlet pressure sensors were located about 20 cm downstream. These locations cause the enthalpy calculated for the outlet cold fluid flow to be less than the actual value at the heat exchanger outlet and the enthalpy calculated for the inlet cold fluid flow to be higher than the actual. In addition, the enthalpy of the outlet hot fluid flow with the current pressure measurement location is lower than the actual value and the enthalpy of the inlet hot fluid flow is higher than the actual value. These differences in calculated enthalpy for the inlet and outlet flows decrease the numerator term in the fluid-based exergy efficiency definition and increase the denominator term, which results in an

Table 5.8 Maximum and minimum fluid-based exergy efficiency for all systems with different capacity rate ratios along with associated maximum and minimum Reynolds numbers for the cold and hot fluids

Variable / System		η_{ch}		Re_c		Re_h	
		Min.	Max.	Min.	Max.	Min.	Max.
System 1	C_r = 0.97	0.076396	0.17765	175.42	2395.4	223.15	3803
	C_r = 0.76	0.12017	0.22643	107.05	1954.6	184.68	4177.7
	C_r = 0.51	0.18527	0.27336	130.66	1448.2	356.62	4451.2
System 2	C_r = 0.97	0.11412	0.22174	301.19	2369.1	379.73	3568.1
	C_r = 0.76	0.16656	0.22939	181.32	1752.2	306.12	3692.7
	C_r = 0.54	0.17495	0.26443	146.39	1580.3	376.19	4413.8
System 3	C_r = 0.96	0.079807	0.13447	289.21	2046.5	361.16	3155.4
	C_r = 0.76	0.13131	0.26628	201.3	1662.3	327.8	2994.6
System 4	C_r = 0.96	0.053053	0.17856	312.3	1803.6	335.93	2418.3

underestimation of exergy efficiency. Hence, higher exergy efficiency is expected if the pressure measurements were relocated to the inlet and outlet ports.

5.4.2 System-based Exergy Efficiency

The second exergy efficiency definition, which is discussed in this section, analyzes the system exergy using Eq. (4.16) as discussed in Chapter 4. For this alternative definition, the system-based exergy efficiency is defined as the ratio of the total system exit exergy to the total system exergy entering the system. Figure 5.25 shows the system-based exergy efficiency for all systems with the different capacity rate ratios

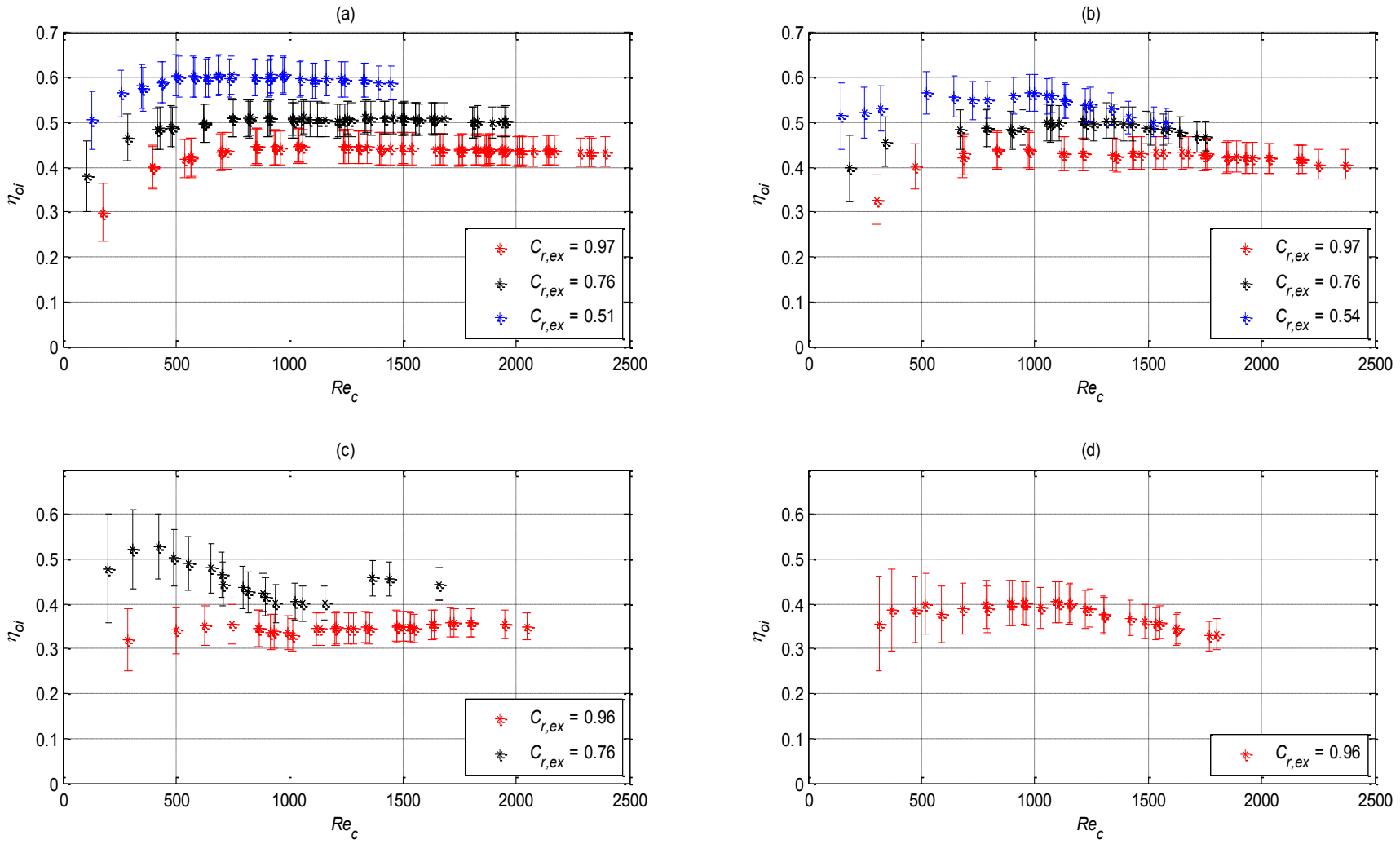

Figure 5.25 System-based exergy efficiency as a function of the cold fluid Reynolds number for all channels: (a) Channel 1 (1000 µm), (b) Channel 2 (750 µm), (c) Channel 3 (500 µm), (d) Channel 4 (350 µm)

as a function of the cold fluid Reynolds number Re_c. As shown in Figure 5.25 (a), η_{oi} increases with increasing Re_c to a maximum value and then decreases slightly, or remains constant, as Re_c increases further. This trend suggests that operating in the higher Re_c range is not recommended. The data in Figure 5.25 (a) for the three different capacity rate ratios suggests that the optimum Re_c value at which to operate is about 500. Again, since the Reynolds numbers of the cold and hot fluids are different; the optimum Re_h at which to operate is about 1000, which is shown in Figure 5.26.

As with η_{ch}, η_{oi} increases with decreasing C_r for fixed Re_c and Re_h as shown in Figure 5.25 (a, b, c, and d) and Figure 5.26 (a, b, c, and d), respectively. This behavior can be explained by examining Eq. (4.16). The cold fluid inlet temperature is fixed at room temperature while the inlet pressure is increased to obtain higher flow rates. Enthalpy and entropy terms in the exergy calculations are temperature and pressure dependant as mentioned earlier; however, the temperature dependence is much stronger. For this reason, the cold fluid inlet exergy is almost constant and has no significant effect on the exergy terms in Eq. (4.16). The hot fluid inlet temperature is shown to increase with the hot fluid mass flow rate; hence, the hot fluid inlet exergy increases with the mass flow rate. Looking at Eq. (4.16) again, the increase in hot fluid inlet exergy results in a decrease in the exergy efficiency; however, as discussed earlier, with lower capacity rate ratios, the cold fluid outlet exergy increases as well. In addition, the cold fluid outlet exergy is summed with the hot fluid outlet exergy, which together offset the effects of the hot fluid inlet exergy in the denominator in Eq. (4.16). A final comparison of the system-based exergy efficiency for all the systems and for each capacity rate ratio as a function

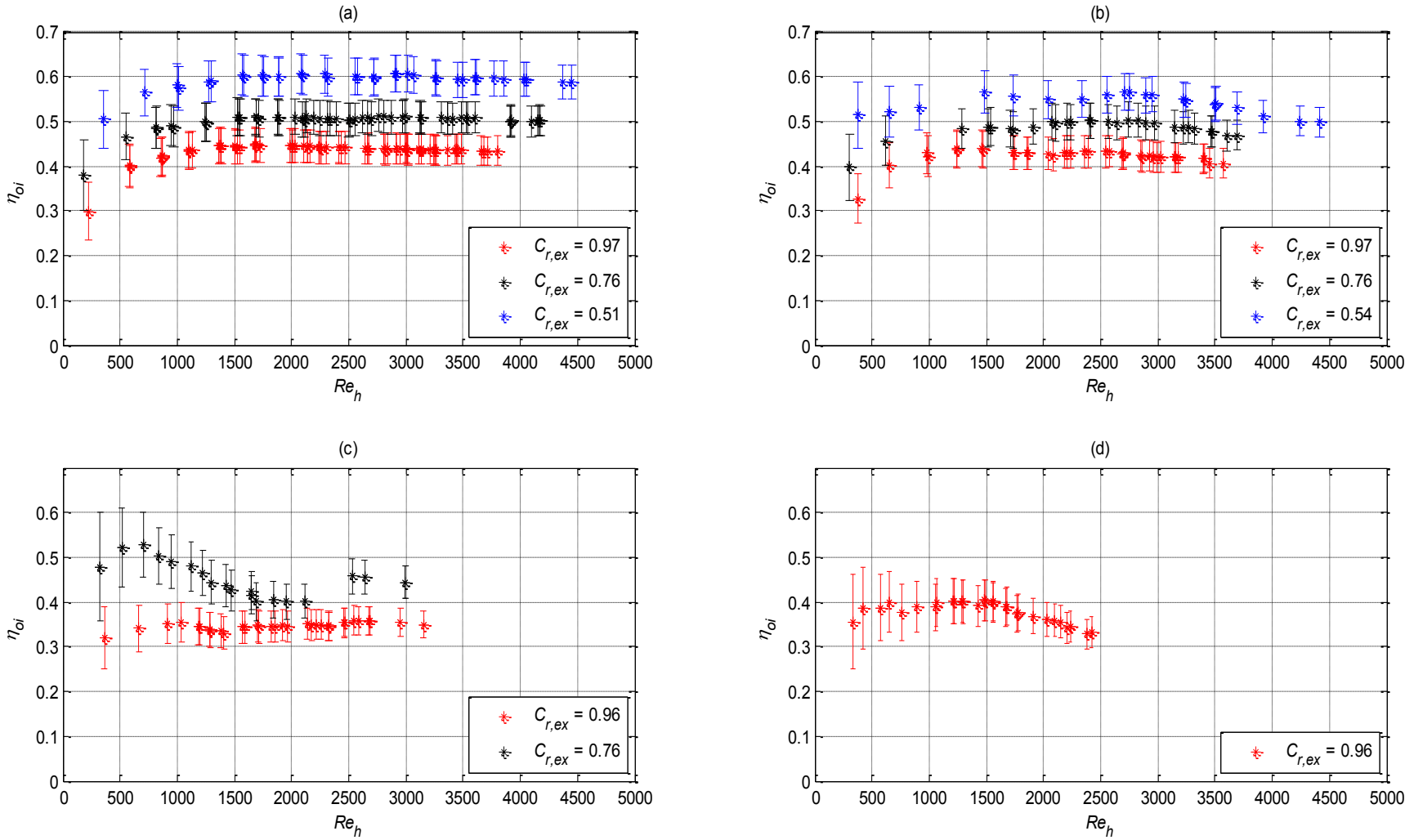

Figure 5.26 System-based exergy efficiency as a function of hot fluid Reynolds number for all channels: (a) Channel 1 (1000 μm), (b) Channel 2 (750 μm), (c) Channel 3 (500 μm), (d) Channel 4 (350 μm)

of both the cold and hot fluid Reynolds numbers is presented in Figure 5.27. The same discussion for the fluids-based exergy efficiency trends in Figure 5.24 is still applicable for the system-based exergy efficiency. Table 5.9 summarizes the range of the system-based exergy efficiency with the corresponding Reynolds numbers for different systems.

5.5 Temperature Changes and Pressure Drops

5.5.1 Fluid Temperature Changes

In this section, the fluid temperature changes across each channel are presented for all systems. Figure 5.28 (a) shows the cold fluid temperature rise across the cold channel as a function of the cold Reynolds number for the different capacity rate ratios. The data indicate that ΔT_c increases with decreasing C_r for fixed Re_c. This is expected as the cold flow was the control variable used to produce the different capacity rate ratios. To satisfy the conservation of energy principle, the temperature rise for the cold flow must increase. Figures 5.28 (b), (c), and (d) present similar temperature change data for systems 2, 3, and 4, respectively. From these data sets, it is also observed that the temperature change increases with the increase in Re_c up to a certain region, after which ΔT_c remains almost constant. In this latter region, the increase in heat rate is directly proportional to the increase in the mass flow rates. The region where ΔT_c remains nearly constant for systems 1 and 2 begins about Re_c~ 1000. For systems 3 and 4, this region begins around Re_c ~ 1500. These results suggest that laminar flow is an acceptable flow regime if the purpose of this type of heat exchanger is to increase the cold fluid temperature. Figure 5.29 presents similar temperature change data, this time for the hot

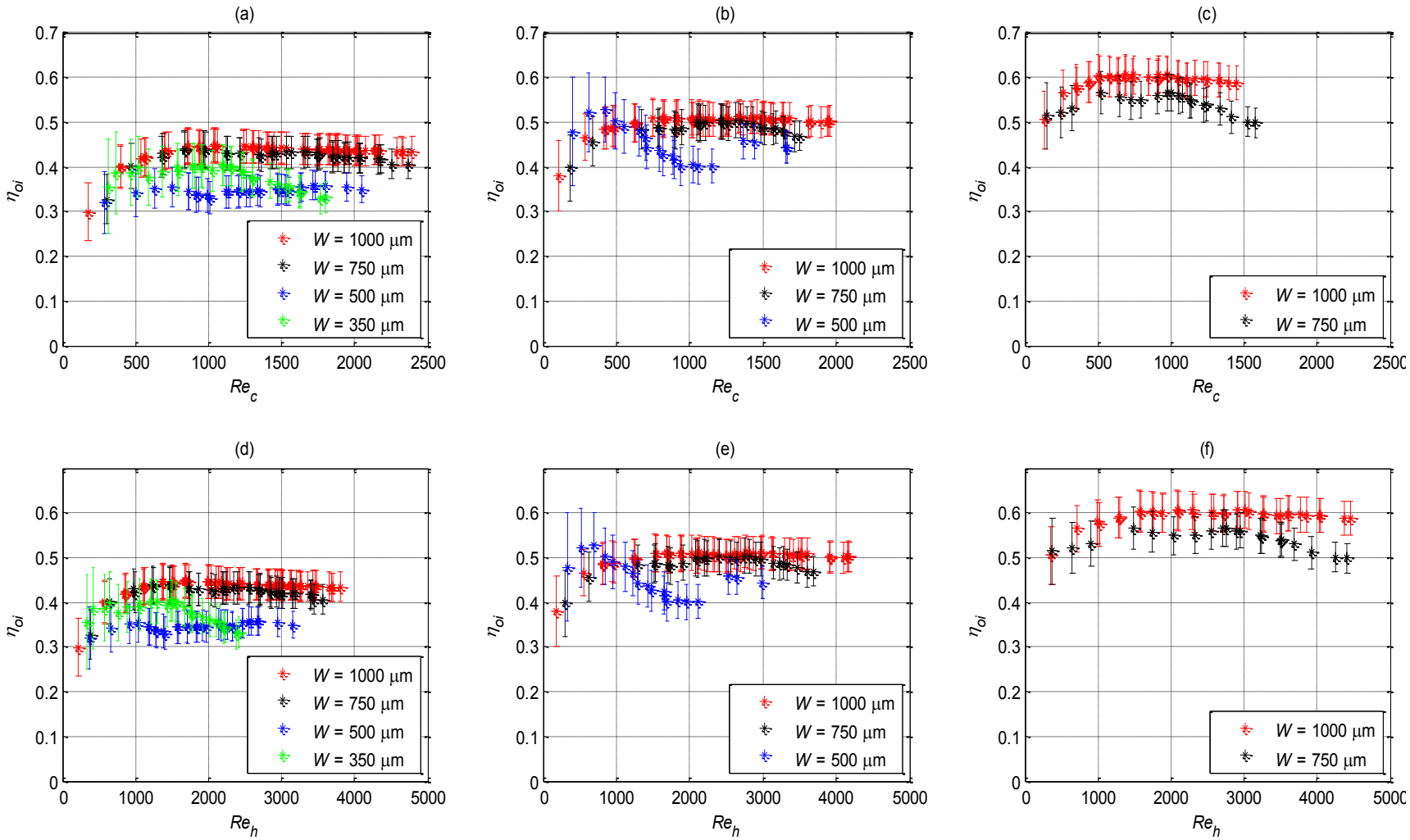

Figure 5.27 Effect of cold and hot fluid Reynolds numbers on system-based exergy efficiency for different capacity rate ratios: (a) $C_r \sim 1$, (b) $C_r \sim 0.75$ (c) $C_r \sim 0.5$ (d) $C_r \sim 1$, (e) $C_r \sim 0.75$ (f) $C_r \sim 0.5$

Table 5.9 Maximum and minimum system-based exergy efficiency for all heat exchangers with different capacity rate ratios along with associated maximum and minimum Reynolds numbers for the cold and hot fluids

System \ Variable		η_{oi}		Re_c		Re_h	
		Min.	Max.	Min.	Max.	Min.	Max.
System 1	C_r = 0.97	0.29837	0.44927	175.42	2395.4	223.15	3803
	C_r = 0.76	0.38018	0.5139	107.05	1954.6	184.68	4177.7
	C_r = 0.51	0.50462	0.60752	130.66	1448.2	356.62	4451.2
System 2	C_r = 0.97	0.32754	0.43997	301.19	2369.1	379.73	3568.1
	C_r = 0.76	0.39802	0.50449	181.32	1752.2	306.12	3692.7
	C_r = 0.54	0.49821	0.56638	146.39	1580.3	376.19	4413.8
System 3	C_r = 0.96	0.31976	0.35938	289.21	2046.5	361.16	3155.4
	C_r = 0.76	0.40056	0.52791	201.3	1662.3	327.8	2994.6
System 4	C_r = 0.96	0.32902	0.40474	312.3	1803.6	335.93	2418.3

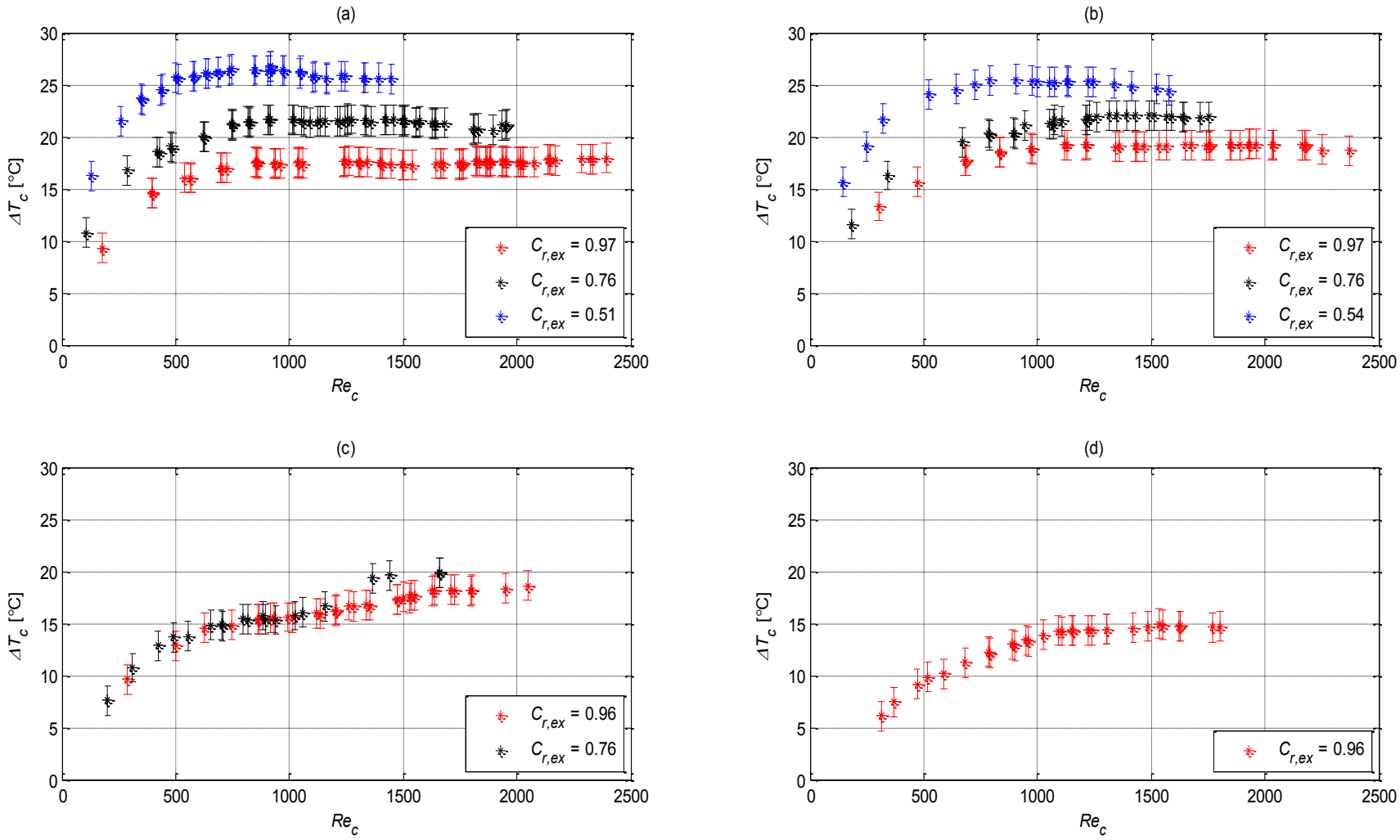

Figure 5.28 Effect of cold fluid Reynolds number on temperature change across the cold channel for different channel sizes: (a) Channel 1 (1000 μm), (b) Channel 2 (750 μm), (c) Channel 3 (500 μm), (d) Channel 4 (350 μm)

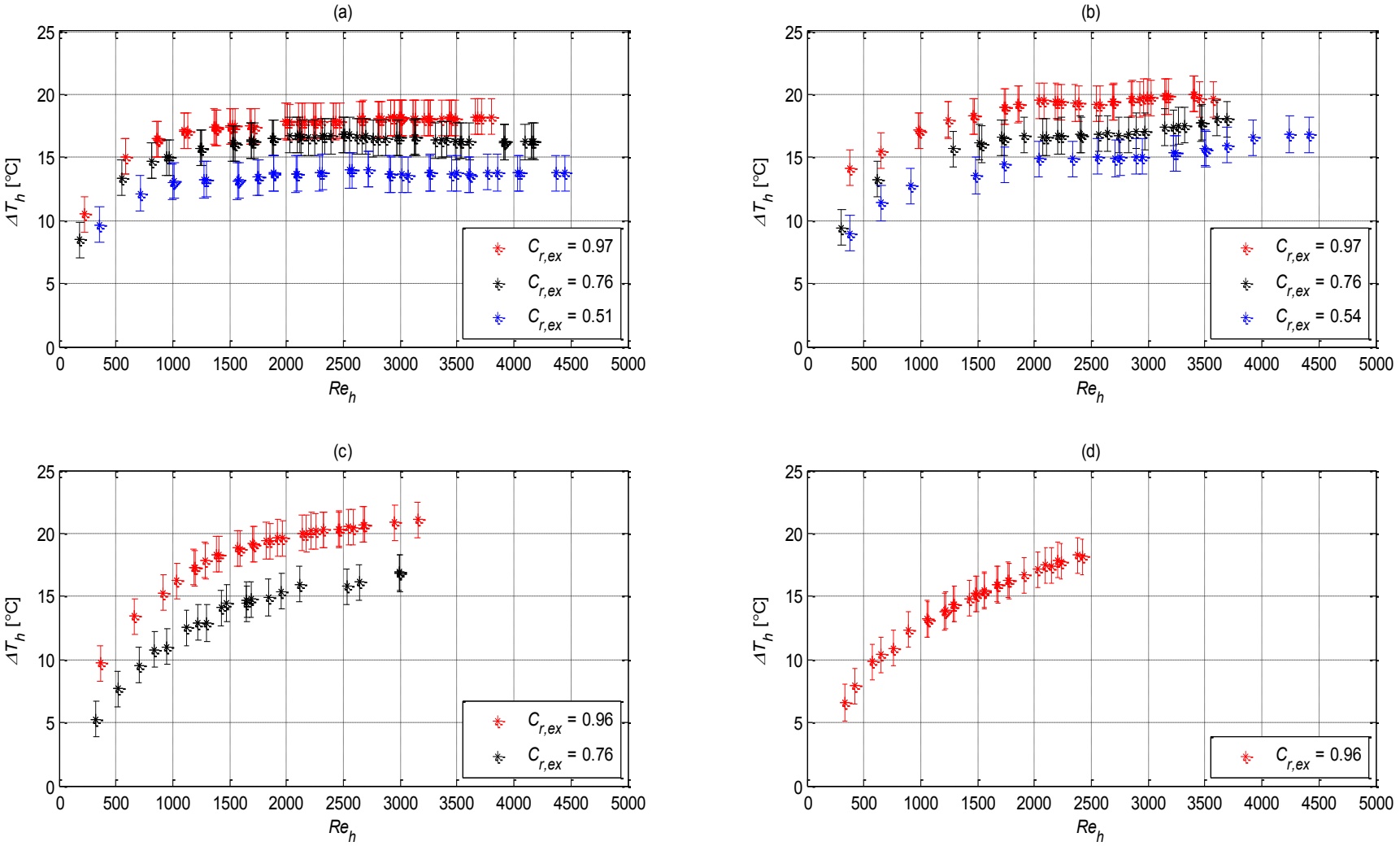

Figure 5.29 Effect of hot fluid Reynolds number on temperature change across the hot channel for different channel sizes: (a) Channel 1 (1000 µm), (b) Channel 2 (750 µm), (c) Channel 3 (500 µm), (d) Channel 4 (350 µm)

fluid temperature drop across the hot channel as a function of the hot fluid Reynolds number for all systems and for all capacity rate ratios. For this case, ΔT_h decreases with the reduction of C_r for fixed Re_h. This effect is due to the relative increase in $\dot{m}_h$ as $\dot{m}_c$ decreases with C_r (conservation of energy principle applied again). This trend is evident in Figures 5.29 (b) and (c) as well. A final comparison between all the systems for each capacity rate ratio is presented in Figure 5.30.

5.5.2 Pressure Drop

In order to evaluate the power needed to drive the flow such that the desired thermal performance is achieved, the pressure drop for each flow in the heat exchanger is required. In this section, the pressure drop for each channel (cold and hot) for the different systems and capacity rate ratios are provided. Figure 5.31 presents the pressure drop for the cold channel as a function of Re_c for all systems and capacity rate ratios. Similar data are provided in Figure 5.32 for the hot channel. Finally, Figure 5.33 presents a comparison of the pressure drops for all systems having the same capacity rate ratio. These pressure drops were measured using sensors located approximately 20 cm upstream and downstream from the inlet and outlet ports, respectively. Thus, in addition to frictional losses in the microchannels, the pressure drop includes minor losses due to fittings, flow in the 20 cm of connecting tubes at the inlets and outlets, bends associated with the inlet and outlet manifolds, flow acceleration in the microchannels, and developing flow. Given the minor losses, a comparison to theoretical frictional losses in the microchannels is not feasible. It is evident, however, that given the small cross

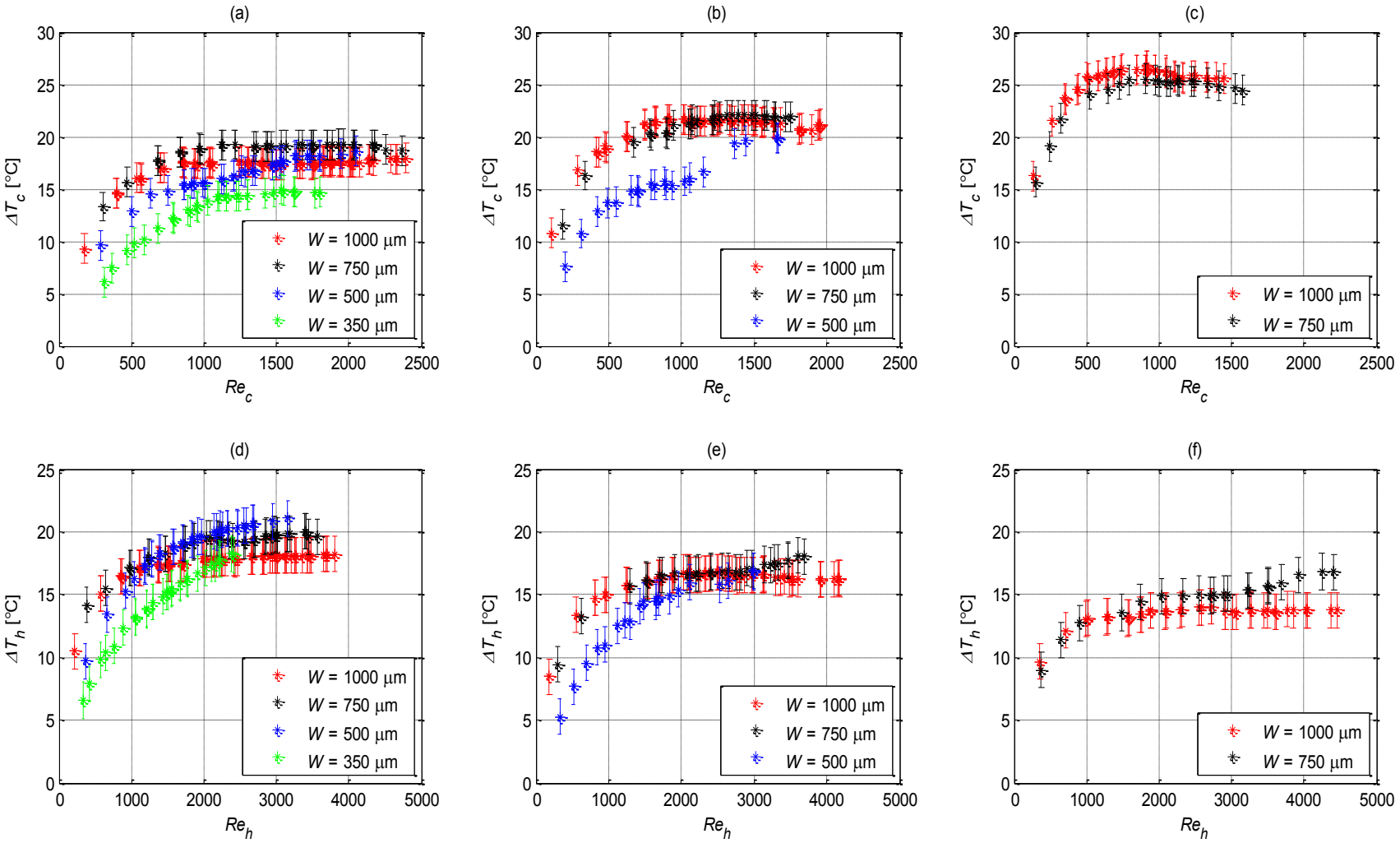

Figure 5.30 Effect of cold and hot fluid Reynolds numbers on temperature change across the cold and hot channels for different capacity rate ratios: (a) $C_r \sim 1$, (b) $C_r \sim 0.75$ (c) $C_r \sim 0.5$ (d) $C_r \sim 1$, (e) $C_r \sim 0.75$ (f) $C_r \sim 0.5$

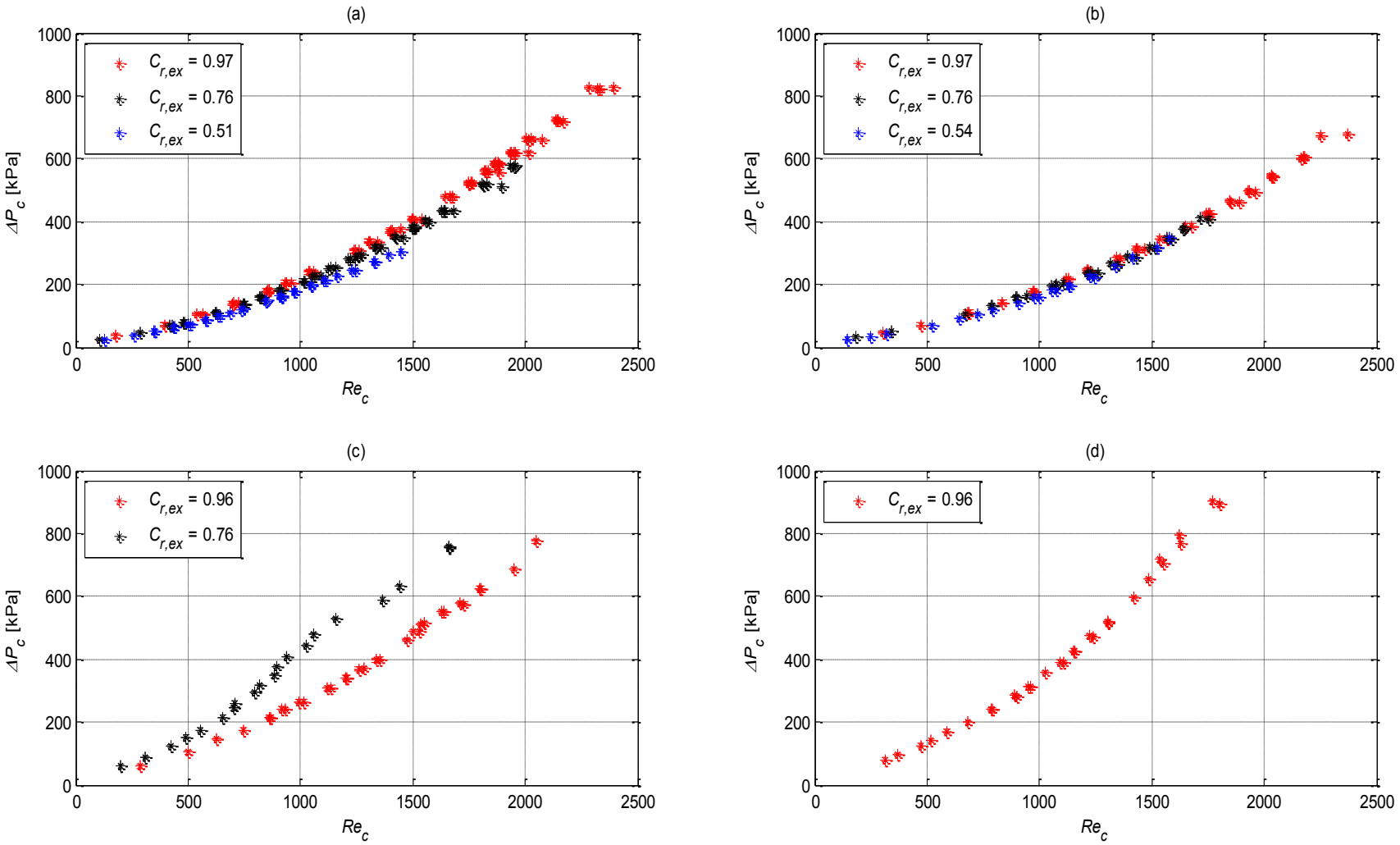

Figure 5.31 Effect of cold fluid Reynolds number on pressure drop across the cold channel for different channel sizes: (a) Channel 1 (1000 µm), (b) Channel 2 (750 µm), (c) Channel 3 (500 µm), (d) Channel 4 (350 µm)

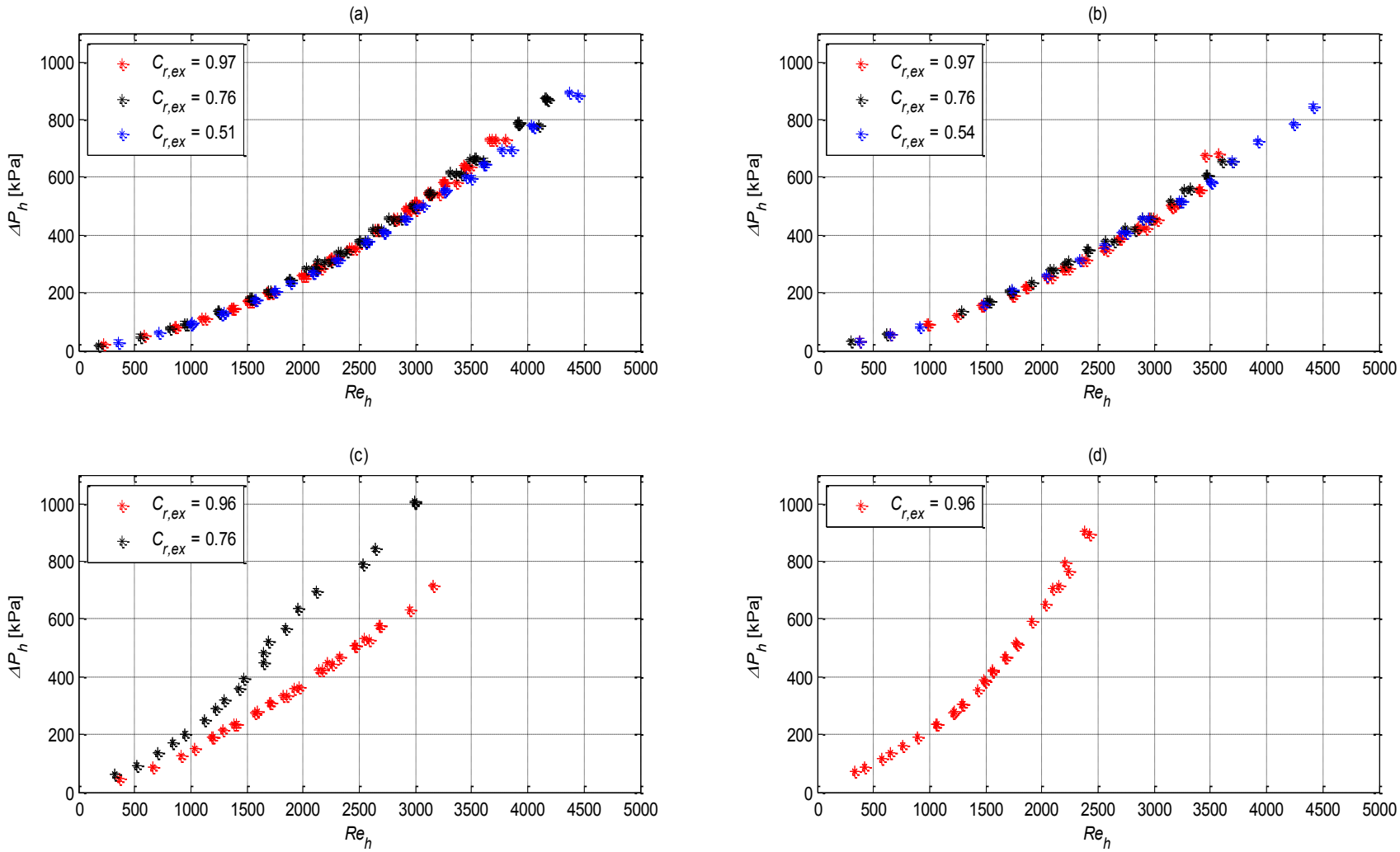

Figure 5.32 Effect of hot fluid Reynolds number on pressure drop across the hot channel for different channel sizes: (a) Channel 1 (1000 µm), (b) Channel 2 (750 µm), (c) Channel 3 (500 µm), (d) Channel 4 (350 µm)

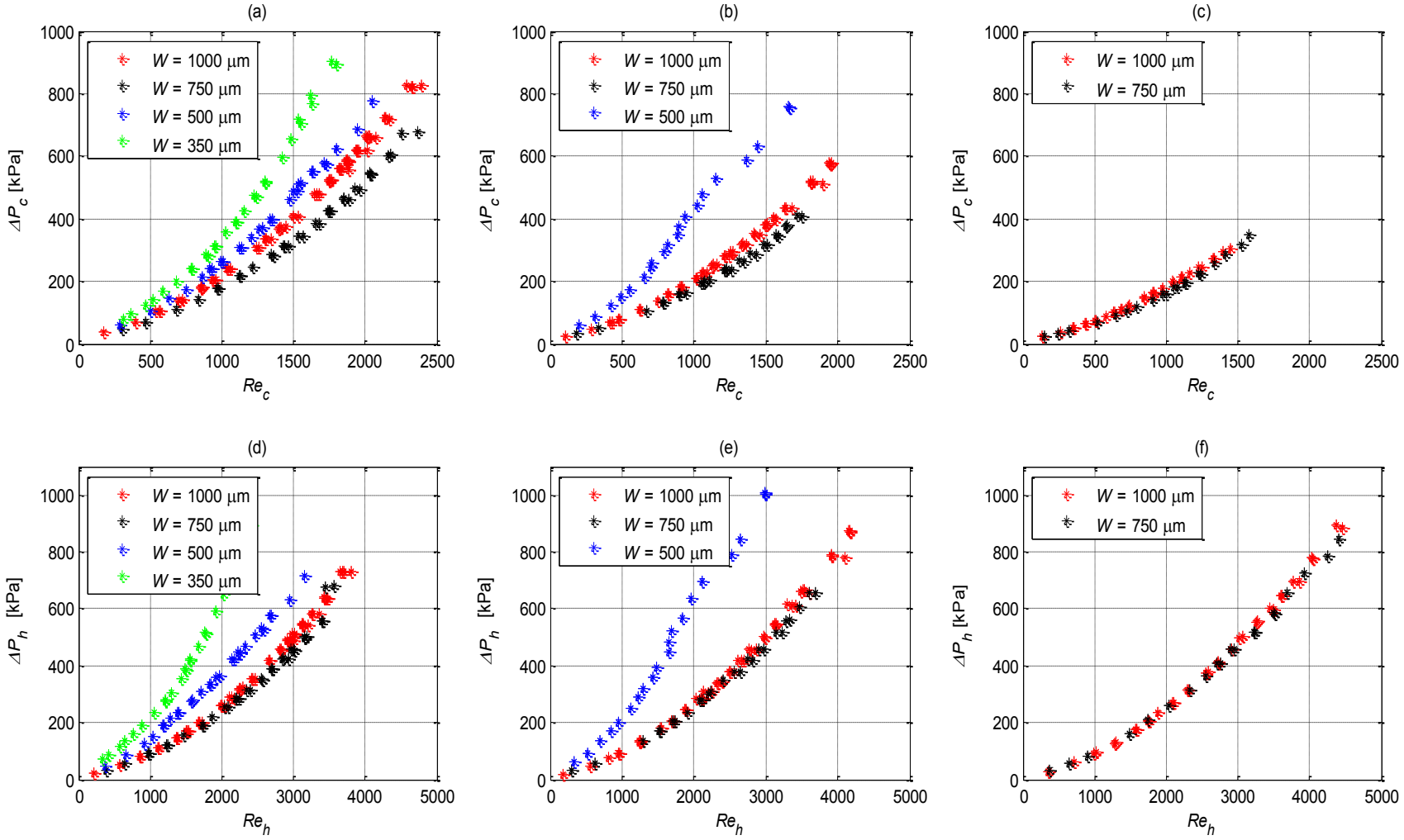

Figure 5.33 Effect of cold and hot fluid Reynolds numbers on pressure drops across both channels for different capacity rate ratios: (a) $C_r \sim 1$, (b) $C_r \sim 0.75$ (c) $C_r \sim 0.5$ (d) $C_r \sim 1$, (e) $C_r \sim 0.75$ (f) $C_r \sim 0.5$

section of the microchannels, the pressure drops are severe. Application of this type of heat exchanger in an on-chip application would likely require off-chip pumping.

5.6 Uncertainty Report

The experimental relative uncertainties using Moffat's [22] approach explained in Chapters 3 and 4 are presented in Table 5.10. The minimum and maximum relative uncertainties for each system and all capacity rate ratios for the major results are shown. Control of the experiment was based on the desire to have a relative uncertainty for the mass flow rates less than 0.1%. This requirement resulted in prolonged time intervals between data collection for each experiment. The maximum relative uncertainties were found in the exergy efficiency results. This is due to the dependence of the enthalpy and entropy terms on the operating pressures which affects the exergy relative uncertainties. It is recommended that the pressure sensors with high pressure limits be replaced with pressure sensors with low to moderate pressure limits in order to reduce the relative uncertainties. Thermocouple measurement uncertainties published by the manufacturer (± 1°C) were used in the analysis. This level of measurement uncertainty is the leading cause of the high uncertainties in results such as q_c and U_{ex}. Thermocouple calibration could reduce the measurement uncertainty to ± 0.1°C, which would significantly reduce the uncertainties in the results.

Table 5.10 Experimental relative uncertainties associated with some variables calculated in current study

Variable	System 1 relative uncertainty %		System 2 relative uncertainty %		System 3 relative uncertainty %		System 4 relative uncertainty %	
	Min.	Max.	Min.	Max.	Min.	Max.	Min.	Max.
q_c	5.28	15.1	5.55	12.1	7.107	18.6	9.46	23.08
q_h	7.75	16.7	7.06	15.7	6.709	26.9	7.74	21.4
q_c''	5.28	15.2	5.55	12.1	7.11	18.6	9.47	23.09
q_h''	7.75	16.7	7.06	15.7	6.72	26.9	7.76	21.4
Re_c	1.42	1.59	1.44	1.57	1.48	1.61	1.54	1.63
Re_h	1.05	1.37	1	1.36	1.16	1.46	1.26	1.5
U_{ex}	6.46	13.9	6.30	13.2	6.45	21.6	8	21.9
U_{vol}	6.46	13.9	6.32	13.2	6.46	21.6	8.02	21.9
ε_{ex}	3.83	7.71	3.65	7.01	3.59	11.7	4.34	11.1
NTU_{ex}	6.43	13.9	6.30	13.2	6.44	21.6	7.98	21.9
η_{ch}	13.3	57.6	13	33.5	17.6	63.7	24.3	75.6
η_{oi}	6.34	21.6	6.85	18.6	8.13	25.4	10.1	29.5

5.7 Summary

An experimental study was conducted to determine the thermal performance of a counterflow xurographic microchannel heat exchanger. Four different channels having different widths, and, hence, aspect ratios, were examined for different capacity rate ratios. Performance parameters included heat rate, heat flux, overall heat transfer coefficient, overall volumetric heat transfer coefficient, effectiveness, number of transfer units, and exergy efficiencies. Heat rates and heat fluxes were found to be highly dependent on capacity rate ratios for each system. In addition, the larger size channels with the same capacity rate ratio were found to have higher heat rates; however, heat fluxes were found to be almost equal. Overall heat transfer coefficients were determined using the log mean temperature difference method (LMTD) and they were compared for each system having different capacity rate ratios and for all systems having the same capacity rate ratio. A similar comparison was made for the overall volumetric heat transfer coefficients. A proposed theoretical overall heat transfer coefficient model was found to poorly represent the experimental data. In addition, a comparison of experimental heat exchanger effectiveness (ε_{ex}) as a function of experimental net transfer units (NTU_{ex}) and an analytical $\varepsilon - NTU$ relationship based on the concentric counterflow heat exchanger model showed strong agreement for all systems with different capacity rate ratios. Finally, two exergy efficiency analyses were performed for two different exergy definitions. Both exergy efficiencies achieved maximum values at Reynolds numbers in the laminar flow region. Hence, the laminar region is recommended to obtain the maximum exergy efficiency; however, higher flow rates are recommended

if the desired goal is maximum heat rate. Table 5.11 presents a comparison between previous experimental work reported by some researchers and the current study results.

Table 5.11 A comparison between present and previous studies

Author	Flow Configuration	Manufacturing technique	Reynolds number	Experimental overall heat transfer coefficient [KW/m2/K]	Experimental overall volumetric heat transfer coefficient [MW/m3/K]
Kang and Friedrich [13]	Counterflow	Diamond machining (Trapezoidal)	72-492	---	33.3-43.3
Alm et al [14]	Counterflow and Crossflow	Streolithography and low-pressure injection molding	---	8.7-19.5	---
Bier et al. [15]	Crossflow	Microtool precision cutting	1400 (hot) 800 (cold)	22.8	324
Jiang et al. [16]	Crossflow	Wire-cutting machine	---	13.3	38.4
Cross and Ramshaw [17]	Crossflow	Stacked etched copper leaves	1300	---	7.3
Hernando et al. [18]	Counterflow	Stainless steel	1600	2-5.5	---
Current study	Counterflow	Xurography	175-4451	3.27-49.437	32.28-488.09

CHAPTER 6

CONCLUSIONS AND RECOMMENDATIONS

6.1 Conclusions

An experimental study was conducted to examine the thermal performance of a xurographic microchannel counterflow heat exchanger. Four different heat exchangers with channels widths ranging from 350 to 1000 μm and nominal channel height of about 100 μm were constructed using xurographic manufacturing. Channels were made from double sided adhesive Kapton® tape and either glass or copper substrates. Kapton® tape is a highly heat resistant material used in many industrial applications. The ease and relatively low cost of manufacturing microchannel heat exchangers by xurography made them a very attractive thermal device to study. Even though Kapton® tape has low thermal conductivity, it was expected that microchannel heat exchangers with closely-spaced channels (~ 1 mm) would still produce relatively good thermal performance. Thus, a microchannel counterflow heat exchanger made from Kapton® tape and glass substrates was built and tested. Experimental results for the glass substrate heat exchanger confirmed the pre-design predictions of poor thermal performance. Subsequently, four heat exchangers were fabricated from Kapton® tape and copper substrates. Nominal channel widths in the heat exchangers were 350, 500, 750, and 1000

μm. Microchannel height for all heat exchangers was defined by the Kapton® tape thickness, which is approximately 100 μm. Upon testing, the desired thermal variables were calculated from the measured data and a comparison of each system with different capacity rate ratios was conducted. Heat rates, heat fluxes, overall heat transfer coefficients, overall volumetric heat transfer coefficients, heat exchanger effectiveness, and exergy efficiencies were calculated from the measured data for the copper substrate microchannel heat exchangers. As expected, the copper substrate devices outperformed the heat exchangers fabricated with glass substrates. A maximum heat rate of approximately 77 W was achieved, which corresponds to a heat flux of almost 120 W/cm^2. The overall heat transfer coefficient ranged from 3.3 to 49.4 $kW/m^2/K$ and the overall volumetric heat transfer coefficient ranged from 32.3 to 488 $MW/m^3/K$. The heat exchanger experimental effectiveness and experimental net transfer units were shown to agree very well with the analytical expression for a concentric counterflow heat exchanger. A proposed theoretical overall heat transfer coefficient model was found to produce poor agreement with the experimental data. A second theoretical overall heat transfer coefficient model based on an analytical NTU expression for the concentric tube counterflow heat exchanger utilizing the experimental heat transfer coefficients was used. Good agreement between the two data sets was is found for the second model. Finally, an exergy efficiency analysis was performed with two different definitions to assess the thermal performance of the heat exchangers from a cost-benefit thermodynamic prospective. From an exergy perspective, it was found that optimal operating conditions are produced at moderate Reynolds numbers in the laminar regime. Complete results were discussed in Chapter 5 in detail; however, it should be noted that flow control was

conducted with a single valve. Thus, reducing the cold fluid flow rate to achieve a lower capacity rate ratio also affected the hot fluid flow rate. These interrelated flow rate changes should be taken into account when utilizing the data.

Results indicate that the thermal performance of xurographic parallel-channel microchannel heat exchangers can be predicted using the concentric tube counterflow heat exchanger theoretical model. In addition, the laminar flow region provides the maximum exergy efficiency, but the greatest heat rates and fluid temperature changes occur at the maximum achievable flow rates.

The answers to the research questions presented in Chapter 1 are as follows:

- Compact single-pass two-channel heat exchangers can be fabricated by xurography.
- The two parallel channel heat exchangers have shown good agreement with theory.
- The maximum fluid temperature reached in current study is ~ 70°C. The Kapton® tape was able to withstand this temperature without any leaks or failure.
- The maximum flow rate achieved is ~ $1x10^{-3}$kg/s and the maximum pressure drop is ~ 1379 kPa (200 psi). These conditions were achieved without leaks or device failure.
- Constructing compact microchannel heat exchangers using glass substrates and Kapton® tape is not desirable, as the thermal performance is poor.
- From an exergy perspective, the best flow condition to operate the heat exchangers is when both fluids are in the laminar flow region. If pressure drop is

not a concern, the flows should be in the turbulent regime to maximize thermal performance.

Additional conclusions for the fabrication of microchannel systems using the xurographic technique are suggested by Nguyen [21]. The following conclusions are drawn from the present study to improve the thermal performance of microchannel heat exchangers fabricated by xurography using double sided adhesive Kapton® tape:

- Xurography can be considered a viable manufacturing technology with which to fabricate microchannel heat exchangers since it is fast and relatively cheap.
- Reliable microchannel heat exchangers can be fabricated from Kapton® tape and highly conductive substrates, such as copper.
- Glass is not recommended as a substrate material for xurographic microchannel heat exchangers.
- Highly conductive materials, such as copper and brass, are recommended for fabricating microchannel heat exchangers using xurography.
- Temperature and pressure sensors should be positioned as close as possible to the inlet and outlet ports to achieve the most accurate readings.
- A clamping system is highly recommended for high pressure flows to mitigate the risk of leaks, both internally between the channels and externally to the surroundings.
- Controlling the capacity rate ratio with a single valve is not desirable.
- Nanoports adhere better with copper when the surface is roughened.

- Doubling the nanoport adhesive rings increases bond strength between the nanoport and copper substrate.

6.2 Recommendations

If the current study was to be performed again, the following recommendations should be considered to increase accuracy and experiment control:

- Low to moderate pressure sensors should be employed to lower the pressure measurement uncertainty. This change would primarily reduce the exergy efficiency uncertainty.
- Thermocouples should be calibrated to lower their measurement uncertainties. This modification would reduce the uncertainty in all reported data.
- Mass balances with greater capacity (> 600 g) should be employed to extend the data acquisition range.
- Two separate flow systems should be used such that the flow rates of both fluids can be controlled independently.
- Micropumps that permit continuous flow, in contrast to the batch flows used in the current experiment, would provide greater experimental flexibility.
- A system that allows temperature control of the hot fluid should be installed. In the current experiment, the temperature of heat source fluid in the tube-in-tube heat exchanger was controlled, which resulted in the hot fluid temperature going to the heat exchanger to change with flow rate.

To expand the current experimental study, the following recommendations are proposed:

- Fluids other than distilled water should be considered to extend the Reynolds number range.
- Different adhesive tapes should be tested to ascertain their thermal performance and bonding capability.
- Microchannel heat exchangers should be fabricated from different substrates such as aluminum and brass.
- Compact serpentine microchannel heat exchangers should be studied to determine the maximum thermal performance available in the small heat exchanger size of the current study
- Measure the channel wall temperatures to estimate the heat transfer coefficients and Nusselt numbers Nu.
- Control the experiment appropriately so the Wilson Plot Method could be employed to determine the average Nusselt number and heat transfer coefficient for the microchannels.
- Use the method proposed by Styrylska and Lechowska [28] to determine the microchannel Nusselt numbers and heat transfer coefficients from the current data sets.
- Create several capacity rate ratios by changing the hot fluid mass flow rate (rather than the cold fluid mass flow arte, as used in the present study) and check the results with the present study.
- Create microchannel heat exchangers from a laser-based xurography technology, which would allow smaller channel widths and smoother channel walls.

- Test the microchannel heat exchangers with inlet cold fluid temperatures below room temperature (i.e., 5°C). This change would extent the Reynolds number range.

REFERENCES

[1] G. Claudia, Micro- and Nanofluidics-Technology and Applications, short course, Proceedings SPIE Photonics west, San Francisco 26 Jan 2011.

[2] D. Erickson, D. Li, Integrated microfluidics devices, Analytica Chimica Acta 507 (2004) 11-26.

[3] D. B. Tuckerman, R. F. W. Pease, High-performance heat sinking for VLSI, Electron Device Letters, IEEE, 2 (5) 1981 126-129

[4] P. Jiang, M. Fan, G. Si, Z. Ren, Thermal-hydraulic performance of small micro-channel and porous-media heat exchangers, International Journal of Heat and Mass Transfer 44 (2001) 1039-1051.

[5] D. Bartholomeusz, R. Boutté, J. Andrade, Xurography: Rapid prototyping of microstructures using a cutting plotter, Journal of Microelectromechanical systems 14 (6) (2005) 1364-1374.

[6] J. Greer, S. Sundberg, C. Wittwer, B. Gale, Comparison of glass etching to xurography prototyping of microfluidics channels for DNA melting analysis, Journal of Micromechanics and Microengineering 17 (2007) 2407-2413.

[7] S. G. Kandlikar, Heat Transfer and Fluid Flow in Minichannels and Micro-channels, first ed., Elsevier Ltd, UK, (2006) pp. 87-136

[8] S. Kandlikar, W. Grande, Evolution of micro-channel flow passages-thermohydraulic performance and fabrication technology, Heat Transfer Engineering 24 (1) (2003) 3-17.

[9] S. Mehendale, A. Jacobi, R. Shah, Fluid flow and heat transfer at micro- and meso-scales with application to heat exchanger design, Appl Mech 53 (7) 2000 175-192.

[10] M. Gad-el-Hak, The fluid mechanics of microdevices-the freeman scholar lecture, Journal of Fluids Engineering 121 (1999) 5-33.

[11] B. Choondal, S. Garimella, A comparative analysis of studies on heat transfer and fluid flow in micro-channels, Microscale Thermophysical Engineering 5 (2001) 293-311.

[12] P. Lee, S. Garimella, D. Liu, Investigation of heat transfer in rectangular micro-channels, International Journal of Heat and Mass Transfer 48 (2005) 1688-1704.

[13] P. Lee, S. Garimella, Thermally developing flow and heat transfer in rectangular micro-channels of different aspect ratios, International Journal of Heat and Mass Transfer 49 (2006) 3060-3067.

[14] W. Qu, I. Mudawar, Experimental and numerical study of pressure drop and heat transfer in a single-phase micro-channel heat sink, International Journal of Heat and Mass Transfer 45 (2002) 2549-2565.

[15] C. Friedrich, S. Kang, Micro heat exchangers fabricated by diamond machining, Precision Engineering 16 (1) (1994) 56-59.

[16] B. Alm, U. Imke, R. Knitter, U. Schygulla, S. Zimmermann, Testing and simulation of ceramic micro heat exchangers, Chemical Engineering Journal 135S (2008) S179-S184.

[17] W. Bier, W. Keller, G. Linder, D. Seidel, Manufacturing and testing of compact micro heat exchangers with high volumetric heat transfer coefficients, ASME, DSC- Microstructures, Sensors and Actuators 19 (1990) 189-197.

[18] W. Cross, C. Ramshaw, Process intensification: laminar flow heat transfer, Chem Eng Res Des 64 (1986) 293-301.

[19] N. García-Hernando, A. Acosta-Iborra, U. Ruiz-Rivas, M. Izquierdo, Experimental investigation of fluid flow and heat transfer in a single-phase liquid flow micro-heat exchanger, International Journal of Heat and Mass Transfer 52 (2009) 5433-5446.

[20] F. Incropera, D. Dewitt, T, Bergman, A, Lavine, Fundamentals of Heat and Mass Transfer, sixth ed., Wiley, New York, 2007, pp. 515-518 and 673-690.

[21] Lam Nguyen, Contraction/Expansion Effects in 90° Miter Bends in Rectangular Xurographic Micro-channels, Master's thesis, University of Utah, Salt Lake City, UT, 2011.

[22] Dan Torgerson, Microscale Loss Coefficients Through Expansion and Contraction Xurographic Micro-channels, Master's thesis, University of Utah, Salt Lake City, UT, 2010.

[23] Rahul Kolekar, Fluid Flow Characteristics in Xurographic Micro-channels, Master's thesis, University of Utah, Salt Lake City, UT, 2009.

[24] Department of Technical Thermodynamics - Mechanical Engineering - University of Applied Sciences Zittau/Görlitz, Professor Hans-Joachim Kretzschmar, Dr. Ines Stöcker (http://thermodynamik.hs-zigr.de/cmsfg/Lehre/index.php?rubric=Downloads+f%FCr+Studierende) Last time visited the website on 07/16/2012

[25] Moffat, R.J., Describing the uncertainties in experimental results, Experimental Thermal and Fluid Science 1 (1998) 3–17.

[26] R. Shah, D. Sekulić, Fundamentals of Heat Exchanger Design, illustrated ed., Wiley, New York, 2003, pg. 790

[27] K. Wark, Advanced Thermodynamics for Engineers, illustrated ed., McGraw-Hill, New York, 1995, pg. 122.

[28] T.B. Styrylska, A.A. Lechowska, Unified Wilson plot method for determining heat transfer correlations for heat exchangers, Journal of Heat Transfer (125) 2003 752-756.